New Jersey Institute of Technology
Digital Commons @ NJIT

Dissertations | Theses and Dissertations

Fall 2013

Discrete element method based scale-up model for material synthesis using ball milling

Priya Radhi Santhanam
New Jersey Institute of Technology

Follow this and additional works at: https://digitalcommons.njit.edu/dissertations

 Part of the Chemical Engineering Commons

Recommended Citation
Santhanam, Priya Radhi, "Discrete element method based scale-up model for material synthesis using ball milling" (2013). *Dissertations*. 152.
https://digitalcommons.njit.edu/dissertations/152

This Dissertation is brought to you for free and open access by the Theses and Dissertations at Digital Commons @ NJIT. It has been accepted for inclusion in Dissertations by an authorized administrator of Digital Commons @ NJIT. For more information, please contact digitalcommons@njit.edu.

Copyright Warning & Restrictions

The copyright law of the United States (Title 17, United States Code) governs the making of photocopies or other reproductions of copyrighted material.

Under certain conditions specified in the law, libraries and archives are authorized to furnish a photocopy or other reproduction. One of these specified conditions is that the photocopy or reproduction is not to be "used for any purpose other than private study, scholarship, or research." If a, user makes a request for, or later uses, a photocopy or reproduction for purposes in excess of "fair use" that user may be liable for copyright infringement,

This institution reserves the right to refuse to accept a copying order if, in its judgment, fulfillment of the order would involve violation of copyright law.

Please Note: The author retains the copyright while the New Jersey Institute of Technology reserves the right to distribute this thesis or dissertation

Printing note: If you do not wish to print this page, then select "Pages from: first page # to: last page #" on the print dialog screen

NJIT New Jersey's Science & Technology University

The Van Houten library has removed some of the personal information and all signatures from the approval page and biographical sketches of theses and dissertations in order to protect the identity of NJIT graduates and faculty.

ABSTRACT

DISCRETE ELEMENT METHOD BASED SCALE-UP MODEL FOR MATERIAL SYNTHESIS USING BALL MILLING

by
Priya Radhi Santhanam

Mechanical milling is a widely used technique for powder processing in various areas. In this work, a scale-up model for describing this ball milling process is developed. The thesis is a combination of experimental and modeling efforts.

Initially, Discrete Element Model (DEM) is used to describe energy transfer from milling tools to the milled powder for shaker, planetary, and attritor mills. The rolling and static friction coefficients are determined experimentally. Computations predict a quasi-steady rate of energy dissipation, E_d, for each experimental configuration. It is proposed that the milling dose defined as a product of E_d and milling time, t, divided by the mass of milled powder, m_p characterizes the milling progress independently of the milling device or milling conditions used. Once the milling dose is determined for one experimental configuration, it can be used to predict the milling time required to prepare the same material in any milling configuration, for which E_d is calculated. The concept is validated experimentally for DEM describing planetary and shaker mills. For attritor, the predicted E_d includes substantial contribution from milling tool interaction events with abnormally high forces ($>10^3$ N). The energy in such events is likely dissipated to heat or plastically deform milling tools rather than refine material. Indeed, DEM predictions for the attritor correlate with experiments when such events are ignored in the analysis.

With an objective of obtaining real-time indicators of milling progress, power, torque, and rotation speed of the impeller of an attritor mill are measured during

preparation of metal matrix composite powders in the subsequent portion of this thesis. Two material systems are selected and comparisons made between *in-situ* parameters and experimental milling progress indicators. It is established that real-time measurements can certainly be used to describe milling progress. However, they need to be interpreted carefully depending on hardness of brittle component relative to milling media.

To improve the DEM model of the attritor mill, it is desired to avoid the removal of unrealistic, high-force events using an approach that would not predict such events in the first place. It is observed that during experiments in attritor, balls may jam causing an increased resistance to the impeller's rotation. The impeller may instantaneously slow down, quickly returning to its pre-set rotation rate. Previous DEM models did not account for such rapid changes in the impeller's rotation. In this work, this relationship between impeller's torque and rotation rate is obtained experimentally and introduced in DEM. As a result, predicted E_d, are shown to correlate well with the experimental data.

Finally, a methodology is proposed combining an experiment and its DEM description enabling one to identify the appropriate interaction parameters for powder systems. The experiment uses a miniature vibrating hopper and can be applied to characterize the powder flow for variety of materials. The hopper is designed to hold up to 20,000 particles of 50-μm diameter, which can be directly described in DEM. Based on comparison of discharge rate from experiments and model, all 6 interaction parameters were analyzed and the ideal conditions identified for Zirconia beads. The values of these parameters for powders are generally not the same as those established for macroscopic bodies. In addition, effects of some other experimental parameters such as particle size distribution and amplitude of vibration are also investigated.

DISCRETE ELEMENT METHOD BASED SCALE-UP MODEL FOR MATERIAL SYNTHESIS USING BALL MILLING

by
Priya Radhi Santhanam

A Dissertation
Submitted to the Faculty of
New Jersey Institute of Technology
in Partial Fulfillment of the Requirements for the Degree of
Doctor of Philosophy in Chemical Engineering

Otto H. York Department of
Chemical, Biological and Pharmaceutical Engineering

January 2014

Copyright © 2013 by Priya Radhi Santhanam

ALL RIGHTS RESERVED

APPROVAL PAGE

DISCRETE ELEMENT METHOD BASED SCALE-UP MODEL FOR MATERIAL SYNTHESIS USING BALL MILLING

Priya Radhi Santhanam

Dr. Edward L. Dreizin, Dissertation Advisor — Date
Professor of Chemical, Biological and Pharmaceutical Engineering, NJIT

Dr. Rajesh N. Davé, Committee Member — Date
Distinguished Professor of Chemical, Biological and Pharmaceutical Engineering, NJIT

Dr. Mirko Schoenitz, Committee Member — Date
Research Associate Professor of Chemical, Biological and Pharmaceutical Engineering, NJIT

Dr. Ecevit A. Bilgili, Committee Member — Date
Assistant Professor of Chemical, Biological and Pharmaceutical Engineering, NJIT

Dr. Wei Chen, Committee Member — Date
Senior Research Investigator, Bristol-Myers Squibb Company, NJ

BIOGRAPHICAL SKETCH

Author: Priya Radhi Santhanam

Degree: Doctor of Philosophy

Date: September 2013

Undergraduate and Graduate Education:

- Doctor of Philosophy in Chemical Engineering,
  New Jersey Institute of Technology, Newark, NJ, 2014

- Master of Science in Chemical Engineering,
  New Jersey Institute of Technology, Newark, NJ, 2008

- Bachelor of Technology in Chemical Engineering,
  Shanmugha Arts, Science, Technology and Research Academy (SASTRA),
  Thanjavur, T.N., India, 2007.

Major: Chemical Engineering

Presentations and Publications:

Santhanam, P. R. and E.L. Dreizin, *Interaction parameters for Discrete Element Modeling of powder flows*. Submitted- Chemical Engineering Science.

Santhanam, P.R., A. Ermoline and E. L. Dreizin, *Discrete Element Model for an attritor mill with impeller responding to interactions with milling balls*. Chemical Engineering Science, 2013. 101: p.366-373.

Santhanam, P.R. and E. L. Dreizin, *Real time indicators of material refinement in an attritor mill*. AIChE Journal, 2013. 59: p. 1088-1095.

Santhanam, P.R. and E. L. Dreizin, *Predicting conditions for scaled-up manufacturing of materials prepared by ball milling* . Powder Technology, 2012. 221: p. 404-411.

Beloni, E., P. R. Santhanam and E. L. Dreizin, *Electrical conductivity of metal powder struck by a spark*. Journal of Electrostatics, 2012. 70: p. 157-165.

Santhanam, P.R., V. K. Hoffmann, M. A. Trunov and E. L. Dreizin, *Characteristics of aluminum combustion obtained from constant-volume explosion experiments*. Combustion Science and Technology, 2010. 182: p. 904-921.

Conference Proceedings:

Santhanam, P.R. and E. L. Dreizin, *Characteristics of metal combustion obtained from constant volume explosion experiments*, 48th AIAA Aerospace Sciences Meeting Including the New Horizons Forum and Aerospace Exposition, Article number 2010-0178, 2010.

Presentations:

Santhanam, P.R. and E. L. Dreizin, *Responsive Discrete Element Model for preparation of advanced materials by mechanical milling using an attritor mill*. AIChE Annual Meeting, Pittsburgh, PA, November 2012.

Santhanam, P.R. and E. L. Dreizin, *Experimental indicators of progress in material refinement by ball milling*. TMS Annual Meeting, Orlando, FL, March 2012.

Santhanam, P.R. and E. L. Dreizin, *Experimental indicators of progress in material refinement by mechanical milling*. Graduate Student Research Showcase, New Jersey Institute of Technology, Newark, NJ, November 2011.

Santhanam, P.R. and E. L. Dreizin, *Scale-up studies of aluminum matrix composites prepared by ball milling*. AIAA Region I Young Professional, Student, and Education Conference, Baltimore, MD, November 2011.

Santhanam, P.R. and E. L. Dreizin, *Experimental indicators of materials processing in mechanical alloying and reactive milling*. AIChE Annual Meeting, Minneapolis, MN, October 2011.

Santhanam, P.R. and E. L. Dreizin, *Predicting conditions for scaled-up manufacturing of materials prepared by ball milling*. Materials Processing and Manufacturing Division, TMS Annual Meeting, San Diego, CA, February 2011.

Santhanam, P.R. and E. L. Dreizin, *Experimental and computational study of progress in material refinement by mechanical milling*. Eastern Analytical Symposium and Exposition, Somerset, New Jersey, November 2010.

Santhanam, P.R. and E. L. Dreizin, *Predicting conditions for scaled-up manufacturing of materials prepared by ball milling*. AIChE Annual Meeting, Salt Lake City, UT, November 2010.

Santhanam, P.R. and E. L. Dreizin, *Experimental and computational study of progress in material refinement by mechanical milling*. Graduate Student Research Showcase, New Jersey Institute of Technology, Newark, NJ, November 2010.

Santhanam, P.R. and E. L. Dreizin, *Discrete Element Method modeling of preparation of reactive nanomaterials by mechanical milling*. Gordon Research Conference on Energetic Materials, Tilton, NH, June 2010.

Santhanam, P.R. and E. L. Dreizin, *Characteristics of metal combustion obtained from constant volume explosion experiments*. 48th AIAA Aerospace Sciences Meeting, Orlando, FL, January 2010.

Santhanam, P.R., C. Badiola, A. Ermoline, M. Schoenitz, and E. L. Dreizin, *Discrete Element Method modeling of preparation of reactive nanomaterials by mechanical milling*. AIChE Annual Meeting, Nashville, TN, November 2009.

Dreizin, E.L. and P. R. Santhanam, *Characteristics of metal combustion obtained from constant volume explosion experiments*. 40th International Annual Conference of ICT, Karlsruhe, Federal Republic of Germany, June 2009.

Santhanam, P.R. and E. L. Dreizin, *Characteristics of metal combustion obtained from constant volume explosion experiments*. AIAA Region I-NE Student Conference, Worcester, MA, March 2009.

To my parents:
Santhanam Appa and Jeyanthi Amma-
THANK YOU. You believed in me even when I did not believe in myself.

Gurumurthy Appa and Bhanumathi Amma-
For your unconditional support.

To my husband, Ram-
We did it!

This kept me going:
"Worry never robs tomorrow of its sorrow, but only saps today of its strength."

ACKNOWLEDGMENT

My life as a graduate student has been a fulfilling experience-packed with beautiful discoveries and wonderful opportunities! I have a lot of people to thank for making the journey worthwhile.

Words cannot express the gratitude and admiration I feel for Dr. Dreizin. He has played a pivotal role in my graduate life as my thesis advisor and a fantastic mentor for my professional career. I thank him wholeheartedly for inspiring me and always providing a positive outlook towards research. Thank you- for keeping the passion and love for research alive in me, and all the students in our research group.

I would like to thank Dr. Schoenitz for always providing constructive criticism at various meetings. His attention to detail is truly remarkable and helped greatly in improving certain sections of this work. Many thanks are due to my committee members Dr. Davé, Dr. Bilgili and Dr. Chen for agreeing to participate and for the insights. Their experiences are in diverse research areas and I benefitted greatly from inputs from these illustrious researchers.

I acknowledge Vern Hoffman for his help with building the vibratory hopper set-up. Thanks to Dr. Alexandre Ermoline for assistance with debugging the C++ codes.

I would also like to recognize the current as well as graduated students in our lab; Dr. Demetrios Stamatis, Dr. Ervin Beloni, Dr. Shasha Zhang, Yasmine Aly, Carlo Badiola, Shashank Vummidi, Rayon Williams, Hongqi Nie, Ani Abraham, Amy Corcoran, Song Wang and Stefano Mercati. Brainstorming, learning and working with everyone has been a great pleasure and I will leave with fond memories of the time spent with them.

A special thank you to Ms. Gonzalez and Dr. Ziavras from the Graduate Studies office at NJIT for their valuable inputs in making this manuscript look better.

I discovered a great support system in the Society of Women Engineers (SWE) chapter at NJIT. Many thanks to all the SWE ladies at NJIT and all over the nation. They serve as great role models to all the female students in the engineering discipline.

I must acknowledge my family and friends for their unconditional support throughout my student life. My parents, who sent me to America against all odds; so that I could receive an education that they could only dream of. I know they had a vision for my future and I hope I have fulfilled their ambitions. A big thank you to my parents-in law- for welcoming me in their hearts and home, accustoming to my life as a graduate student and for showering me with abundant love and support. Special thanks to my best friends and the sisters I never had, especially Lakxmi Gurumurthy, Sangeetha Ramamurthy and Supraja Varadharajan; for some great advice and 'the talk' whenever I needed it!

Lastly, and most importantly, I would like to thank my husband, Ram Gurumurthy. He deserves immense gratitude and respect for his support and encouragement. I could not have achieved everything I did during my graduate student life without his positive attitude, encouragement and patience. They say that good work-life balance stems from choosing the right life partner-I am glad we chose each other!

TABLE OF CONTENTS

TABLE OF CONTENTS
(Continued)

TABLE OF CONTENTS
(Continued)

Chapter **Page**

TABLE OF CONTENTS
(Continued)

Chapter **Page**

TABLE OF CONTENTS
(Continued)

LIST OF TABLES

LIST OF FIGURES

Figure **Page**

LIST OF FIGURES
(Continued)

LIST OF FIGURES
(Continued)

LIST OF FIGURES
(Continued)

Figure **Page**

LIST OF FIGURES
(Continued)

CHAPTER 1

INTRODUCTION

1.1 Background

Mechanical milling is a technique widely used for powder processing. In the field of energetic materials, high-energy milling is attractive for preparation of mechanically alloyed, nano-composite, reactively milled, and mechano-chemically activated powders [1-5]. In the past decade, ball milling has also expanded as a valuable tool in other applications such as food [6, 7], pharmaceutical [8-10], energy storage [11, 12], military and aircraft [13, 14], soil remediation [15] and even biomedical engineering [16]. Despite the extensive uses, transition to practical manufacture in most cases is either extremely slow or currently non-existent. The primary challenge is the lack of scientific methodologies to transfer milling conditions form laboratory scale to large-scale production. The problem is particularly daunting when milling devices are of different scale or different operation type.

Before analyzing the development of scale-up models, an overview of existing models to understand the ball milling process itself is presented. Historically, Benjamin [17] pioneered applications of ball milling as a materials synthesis technique; his work focused on dispersion strengthened alloys. In his earlier works, preliminary ideas for rate-based models of mechanical alloying were presented. An expression for calculation

of average rate of change of lamellar thickness was established, which was indirectly based on strain rate, and hardness of powders being milled. The core of that development was based on the energy input to the powders being processed. Several authors, who attempted to quantify and understand the ball milling process, adopted and further developed this fundamental idea. The modeling studies can broadly be classified as following atomistic [18-21] and mechanistic approaches [22-32].

As the name suggests, the atomistic models studied the mechanical alloying process on an atomic scale using molecular dynamics approach [18-20] and semi-empirical thermodynamic models [21, 33]. The repeated welding and fracture mechanisms combined with temperature effects cause atomic level diffusion and result in alloy phase formation. Deciphering such alloying mechanism was the goal of the atomistic studies.

Mechanistic modeling involved use of mechanical properties of the powders and balls to identify properties such as temperature rise during collisions, particle sizes, hardness, etc. Originally, collisions were considered as the only means of energy transfer [17, 22, 25] and appropriate kinematic equations were developed. Later, it was realized based on theoretical understanding as well as video observations of ball mills that both collisions as well as attrition (rolling or sliding) of the balls were essential contributors to the energy transfer [28, 34] and more detailed models were developed.

Despite impressive analysis and results, the aforementioned attempts achieve either empirical or semi-quantitative outcomes. Additionally, their usefulness for a comprehensive understanding of the ball milling process or prediction of scale-up parameters has not been demonstrated successfully. One of the breakthroughs in development of quantitative parameter with potential use in scale-up studies came from Delogu and Cocco [31, 32]. They introduced a simple milling dose parameter to relate the energy transfer during the ball milling operation to the duration of milling. This concept of milling dose was further developed by Jiang et al., [35] and Ward et al., [36] and its applicability for descriptions of shaker and planetary mills was explored. This thesis will advance that work and further establish milling dose as a useful concept for different types of mills.

While the aforementioned authors investigated the fundamentals of the ball milling processes, a few others ventured into understanding the mill operation via numerical methods [37-42]. Specifically, Discrete Element Modeling (DEM) was established to be an extremely valuable tool to model the ball milling devices [39-41]. Although the computational capabilities at the time of the early DEM efforts were not as advanced as today, they certainly contributed to promote the understanding of the process. Conventionally, one of the principal limitations in development of discrete element models of ball mills has been identification of appropriate material properties as well as interaction properties (restitution, friction coefficients). The material properties

can of course, be obtained easily from various literature sources. However, there are no reports in literature of validated and suitable methods to estimate the correct values for the interaction parameters. The discrete element modeling approach itself has been around for a few decades, and a lack of studies for identification of the important parameters for most DEM descriptions is quite striking.

1.2 Objectives

The general objective of this work includes development of a validated model describing material refinement in different types of ball-milling devices, while accounting for differences in the milling device type, scale and milling conditions. Milling dose will be utilized to develop scale-up parameters. In the process of achieving the aforementioned goal, a combination of experimental and modeling efforts will be presented in this thesis. The modeling tool utilized in this work is commercially available EDEM software by DEM Solutions.

The following specific objectives are proposed:

1. Create DEM-based models to describe various milling devices. Develop a scale-up approach and validate outcomes from the mill models with appropriate experiments. Meanwhile, obtain unique, powder dependent milling media interaction parameters for use in the DEM models.

2. Identify a non-intrusive technique to obtain parameters that can aid in validating the scale-up models. Specifically, examine the feasibility of using real-time parameters measured during the actual milling experiment as milling progress

indicators to replace the labor-intensive, sample interrogation based experimental methods employed currently.

3. Investigate the use of in-situ indicators of milling progress in tailoring the existing DEM models. This will help to better reflect the actual operation of milling devices, and thus, improve the efficacy of the scale-up models.

4. Develop a novel methodology to obtain material-dependent, particle-level interaction parameters (friction and restitution coefficients) for DEM studies in general.

CHAPTER 2

PREDICTING CONDITIONS FOR SCALED-UP MANUFACTURING OF MATERIALS PREPARED BY BALL MILLING

2.1 Introduction

Mechanical milling is used to prepare a wide range of materials [4, 43]. Specific examples include powders with reduced particle sizes [44], amorphous and nano-structured alloys [45, 46], metal-organic composites [47], and reactive materials such as mechanically alloyed or composite powders with components capable of highly exothermic reactions [48, 49]. Laboratory scale synthesis enables a relatively tight control over the structure, composition and morphology of the prepared materials. When demand for newly developed materials increases, the laboratory processes need to be transferred to practical manufacturing methods, which is an important challenge. The scale-up difficulties are primarily due to the absence of validated models describing material refinement in ball mills quantitatively. It is imperative to develop such models capable of predicting milling progress for different milling devices without the need for device- or material-specific adjustable parameters.

In a useful model, parameters describing material refinement should be obtained as a function of the milling conditions. Material refinement is expressed through evolution of specific material parameters of interest, such as the average particle size or the fraction of the intermetallic phase formed as a result of milling. These material

parameters should be correlated with the process- and device-specific characteristics describing energy transfer from milling tools to the milled materials. Such process characteristics may be difficult to describe quantitatively, considering multiple types of interactions between the milling tools, milling container, and the milled powder. Most importantly, the relationships between the process characteristics and the rate of material refinement have not been well understood and appear to vary as a function of the milling conditions or for different milling devices. Earlier, it was suggested that milling progress can be expressed using a function called milling dose, D_m [31, 36] defined as the ratio of the energy transferred to the powder from the milling tools, W to the mass of the milled powder, m_p:

$$D_m = W / m_p \tag{2.1}$$

Ward et al. and Jiang et al. [35, 36] used milling dose to track preparation of reactive nanocomposite powders, for which the refinement of components (size of oxide inclusions in a metal matrix) served as the material specific parameter of interest. Assuming steady milling conditions, the energy transferred to the powder was expressed as a product of the rate of energy dissipation in the ball mill, E_d, and the milling time, t. Thus, milling dose was expressed as a function of milling time:

$$D_m = E_d \cdot t / m_p \tag{2.2}$$

Thus, if the milling time required to prepare a specific product is determined experimentally, milling dose specific for that product is directly proportional to the energy dissipation rate. Multiple recently developed Discrete Element Models (DEM) describing the motion of the milling tools [38, 50] enable a relatively straightforward calculation of the energy dissipation rate. However, DEM describes the motion of the milling tools and not the milled powder. Therefore, two main challenges in utilizing the DEM predictions are:

- Account for the effects of the milled material on the motion of and energy exchange between the milling tools;
- Determine which fraction of the energy dissipated in interactions between the milling tools is responsible for the refinement of the milled material (parts of the energy can be used to heat the entire milling container, deform or damage the milling tools, or simply move the milled material without refining it.)

Previously, the presence of milled material on the motion of the milling tools was accounted by appropriate selection of the restitution coefficient describing collisions of the milling balls coated with powder [36, 51]. However, the effect of the milled material on the friction coefficients was not addressed. Furthermore, rolling friction was not explicitly considered in some of the previously reported DEM calculations, and it was

shown that such an omission results in a gross underestimation of the energy dissipated in a planetary mill and used to refine the milled powders [36].

This effort is aimed to develop a DEM-based model and approach for interpreting the computational results enabling an adequate description of the milling progress. The approach should be suitable for applications involving both manufacturing and processing of materials using different ball-milling devices.

2.2 Experimental

2.2.1 Materials

The materials for milling experiments were selected to enable measurements of the yield strength of the prepared composite increasing as a function of the milling progress. Powders of pure aluminum (-325 mesh, 99.9% pure, by Atlantic Equipment Engineers) and magnesium oxide (-325 mesh, 99% pure, by Aldrich Chemical Company, Inc.) were blended together for green mixture. These components do not react chemically, so the product of the ball milling is a work-hardened composite material. The starting powder blend included 30% aluminum and 70% magnesium oxide by volume.

2.2.2 Milling Devices and Parameters

Prepared powder blends were ball milled using three devices: a SPEX 8000 shaker mill, a Retsch 400 PM planetary mill, and a Union Process HD 01 attritor mill. The process

control agent was stearic acid (1% by wt.). Steel balls with 9.5 mm nominal diameter were used in all three mills. The milling jar of the attritor mill was cooled with room temperature water. Milling jars of the shaker mill were cooled using room temperature compressed air flow. Finally, the temperature in the milling compartment of the planetary mill was kept at 15 ºC using an air conditioner attached to the mill. Milling times varied from 30 min to 8 hours. Other milling conditions are shown in Table 2.1.

Table 2.1 Milling Conditions Used for Different Ball Mills

Parameter		**Shaker mill**	**Planetary mill**	**Attritor mill**
Charge Ratio (ball to powder mass ratio)		10	3	36
Powder mass, g		5	30	50
Rotation speed, rpm		1054 (fixed)	300, 350	200, 400
Impeller dimensions (vertical shaft, four horizontal bars), mm	Length	N/A	N/A	86.2
	Diameter	N/A	N/A	25.2
	Bar length	N/A	N/A	51.9
	Bar diameter	N/A	N/A	10.4
Vial dimensions, mm	Height	52.4	51.4	101.6
	Diameter	26.4	101.6	76.2

2.2.3 Milling Progress Assessment: Yield Strength Measurement

Different material parameters have been used to assess the milling progress in the past, ranging from particle size [4], grain size refinement [4, 52], to the ignition temperature of the ball-milled powder [53, 54]. In this study, preliminary experiments considered changes in the particle size for brittle materials and development of intermetallic phases

for mechanically alloyed powders. It was observed that the particle size changes very rapidly for brittle powders, such as sand, so that it is difficult to identify the rate of its change during milling with steady conditions. Changes in particle morphology (such as flake formation) masked the changes in the particle sizes for ductile powders. It was also observed that multiple intermediate and difficult to quantify phases are formed in mechanically alloyed powders making formation of such phases an inconvenient indicator of the milling progress. Following these preliminary studies, a change in the yield strength of the work-hardened oxide-reinforced composite powders was selected as an experimental indicator of the milling progress.

The compression curves (Figure 2.1, Left) were measured while consolidating prepared powders into pellets using an Instron 5567 universal strength tester. At least three pellets were made out of each sample obtained from the milling experiment. The cross-head extension rate used for the test was 0.6 mm/min and the maximum load applied was 30,000N.

The yield strength, σ_0 was found from experiments on compaction of the prepared powders by fitting the measured compression curves for porosity, *e*, as a function of pressure, *P* (Figure 2.1, Right), using a modified Heckel equation [55]:,

$$\ln\frac{1}{e} = \ln\frac{1}{e_0} + \frac{1}{3k_1}\ln\left(1+\frac{k_1 P}{\sigma_0}\right) \tag{2.3}$$

where e_0 is the initial porosity of the compact and k_1 is a parameter based on Poisson's ratio. Both initial and current porosity values were calculated using theoretical maximum density of the material and the volume of the powder being consolidated.

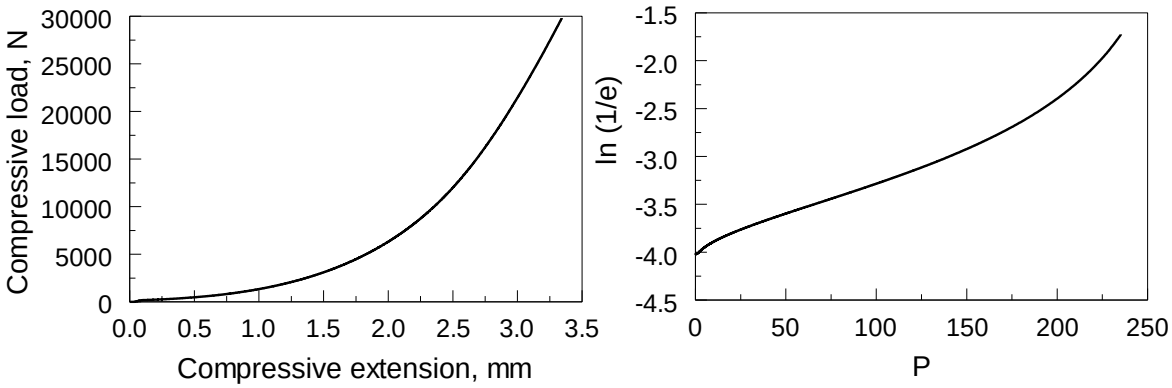

Figure 2.1 (Left) Loading curves from Instron device (Right) Fitting parameters using the modified Heckel equation to obtain yield strength.

2.3. DEM Description

2.3.1 Model Details

Commercial EDEM software by DEM Solutions Inc. [56] was used to describe all the milling devices. The Hertz –Mindlin (no slip) [57] contact model was used for the force calculations. This is a soft-particle contact model [58] and it describes the behavior of milling tools when they come into contact with one another. The time step for the calculations was 1 µs.

The normal (F_n) and tangential (F_t) forces in the model are evaluated using equations (2.4) and (2.5).

$$F_n = \frac{4}{3} Y^* \sqrt{R^*} \delta_n^{3/2} \tag{2.4}$$

$$F_t = -S\,\delta \tag{2.5}$$

where Y^* is the equivalent Young's Modulus, R^* is the equivalent radius, S_t is the tangential stiffness and δ_n and δ_t are the normal and tangential overlaps respectively. Unlike previous models [35, 36], the friction and restitution coefficients were accounted for individually in this code. Coulomb friction limits the tangential force and is given by $\mu_s F_n$, where μ_s is the coefficient of static friction. Also, the rolling friction μ_r is incorporated by applying a torque (τ_i) to the contacting surfaces (Equation 2.6).

$$\tau_i = -\mu_r F_n R_i \omega_i \tag{2.6}$$

where R_i is the distance of the contact point from the center of mass and ω_i is the unit angular velocity of the object at the contact point. The value of the restitution coefficient was selected based on previous reports [36]. The values of the friction coefficients were determined following the procedure outlined below.

2.3.2 Experimental Evaluation of Friction Coefficients

A dedicated experiment and respective DEM model were designed in order to obtain the friction coefficients. In the experiment, a single ball was freely rolling within a milling

vial, as shown in Figure 2.2. Both ball and vial surfaces were coated by the milled powder. The ball's motion in this specific configuration was also described using the DEM model. The values of rolling and static friction coefficients were selected to match the predictions with the experiment.

To prepare the vial and the ball surfaces, Al and MgO mixtures were milled for different times in the planetary mill. The powder and balls were removed from the vial without disturbing the powder adhered to the vial surface; the vial was then placed horizontally, as shown in Figure 2.2.

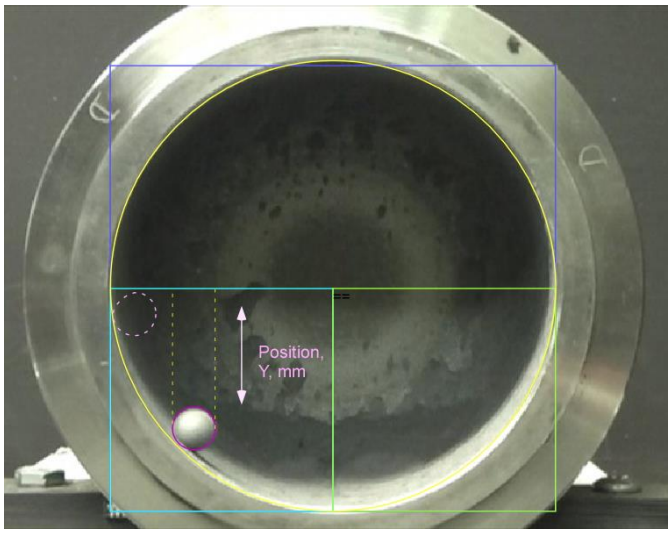

Figure 2.2 A video frame used for tracking the vertical position of the rolling ball. A dashed circle shows the initial ball position. The planetary mill vial shown was taken out after 30 minutes of milling.

A single ball from the milling experiment was dragged to the left-center position (dotted circle in Figure 2.2) of the vial and then released. The ball motion included

several oscillations before it stopped at the bottom of the vial. The experiment was videotaped using a camcorder. From the video, the heights and moments when the topmost positions of the ball occurred were recorded. At those moments, the ball stopped instantaneously, so that its image was less blurred in the videos. Open symbols in Figure 2.2 show coordinates of the topmost positions of the ball as a function of time.

In parallel to experiments, a model of a single ball rolling down a planetary mill vial wall was set up in DEM. The initial position of the ball in the DEM was set to be identical to that in the rolling experiment. The output data extracted from this calculation was the ball position as a function of time.

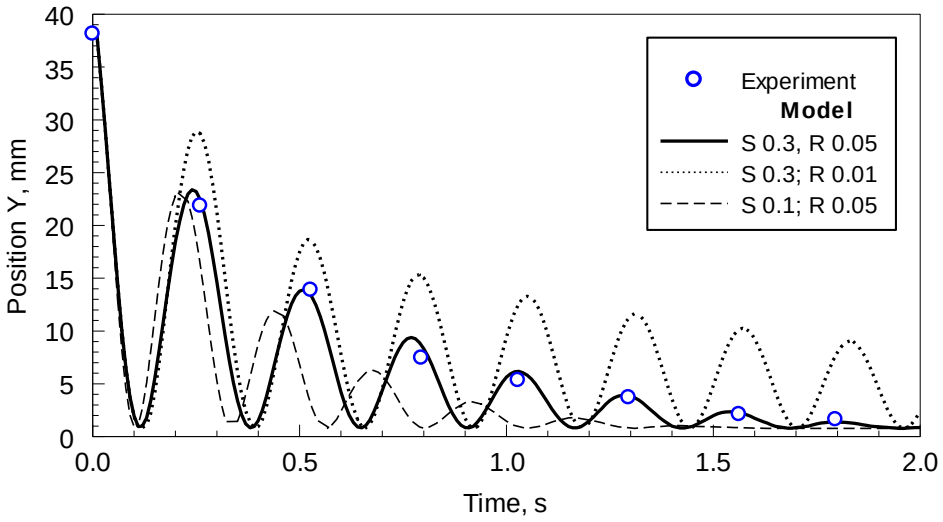

Figure 2.3 Predicted changes of the vertical position of the rolling ball as a function of time compared to the ball locations measured from the video. 'S' and 'R' in the legend represent values of static and rolling friction coefficients, respectively.

The best match between the experimental and predicted ball trajectories was found by systematically varying the values of static and rolling friction coefficients. It was observed that the static friction affected the ball position at early times, when its velocity was high, while rolling friction controlled the ball motion later, when it was decelerating. Therefore, matching the experimental and measured ball's trajectories during the entire experiment enabled us to select the values for both coefficients. Examples of the calculated ball trajectories, presented through the vertical coordinate as a function of time are illustrated in Figure 2.3 for different values of the friction coefficients.

Comparison of experimental and computational results, suggested that the rolling and static friction coefficients should be taken as 0.05 and 0.3, respectively. For this comparison, experimental data were collected using the milling vial and ball coated with the powder formed as a result of 0.5 hour milling at 350 rpm (powder load 30 g). Note that experiments were also performed with powders prepared as a result of milling for 1, 2 and 3 hours. Friction coefficients did not substantially change as a function of the milling time. The static friction coefficient varied in the range of ± 30% from the above values and the rolling friction coefficient remained consistent with that found for the sample milled for 0.5 hours. A small change in the static friction was observed only for the longest duration experiment (3 hours). It was further tested that the rates of energy dissipation calculated by DEM were hardly affected by such small variations in the

friction coefficients. Therefore, all further calculations assumed constant friction coefficients.

2.3.3 Descriptions of Different Milling Devices

Figure 2.4 presents the DEM models for the shaker, planetary and attritor mills. The ball color represents its total energy and the color scale is the same for all the cases, red indicating the highest energy and blue the lowest.

In the shaker mill, the balls are flying across the vial with the primary energy dissipation coming from head-on collisions, consistent with the earlier report [36]. For the planetary mill, the balls are rolling along the vial surface forming a relatively stable two-dimensional structure, also similar to earlier results [35]. For the attritor mill, the balls move much slower; at higher rpm some of the balls are observed to be airborne for short periods of time.

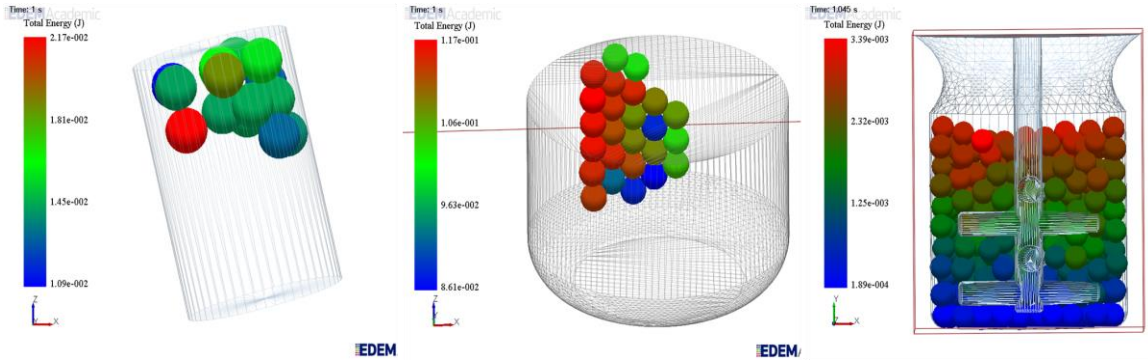

Figure 2.4 DEM models of the three milling devices. The left image shows the shaker mill, the center image is the attritor mill (400rpm) and on the right is the planetary mill (350rpm).

2.4 Results

2.4.1 Yield Strength as an Indicator of Milling Progress

The yield strengths for samples prepared in the three milling devices as a function of milling time are shown in Figure 2.5.

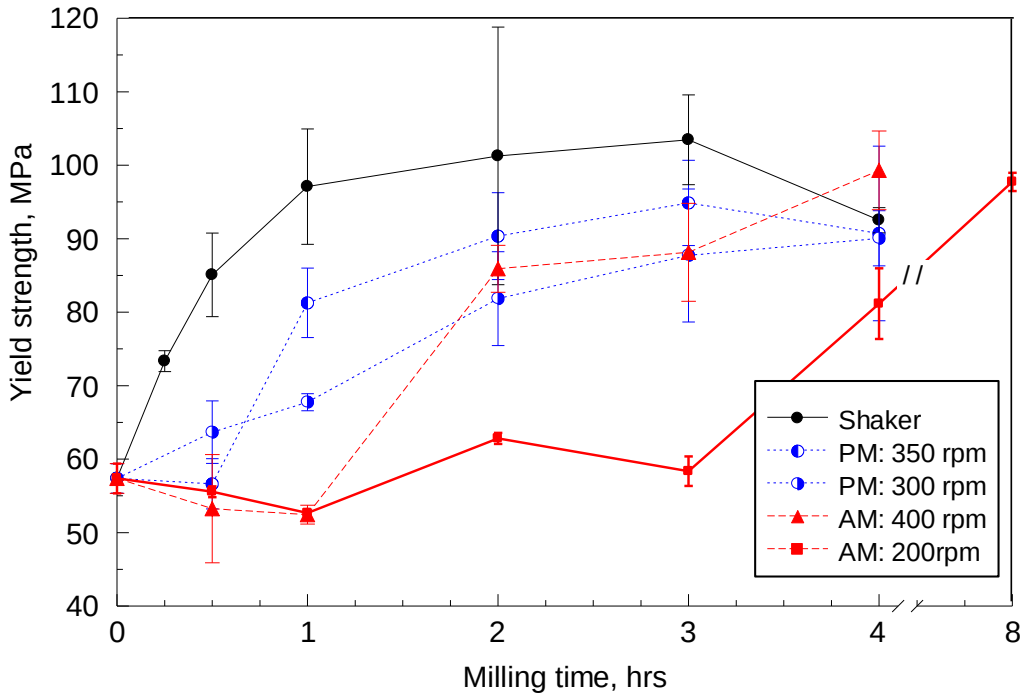

Figure 2.5 Yield strength for different samples as a function of milling time. SM, PM and AM represent shaker mill, planetary mill and attritor mill respectively.

The error bars show standard deviation of the values obtained by processing the experimental loading curves for individual pellets. The yield strength initially seems to be unaffected or even reduced for some of the experiments; however, for all mills and milling conditions the yields strength is observed to increase at longer milling times. Eventually, the value of the yield strength is stabilized. The initially stable or even

reduced yield strength is correlating with the formation of flakes, as illustrated in Figure 2.6. Flakes were observed to form at short milling times in all ball mills. An increase in the measured yield strength at longer milling times correlated with breaking down the flakes and formation of composite equiaxial particles, as also shown in Figure 2.6. When milling times increased further, the particle sizes decreased only slightly, possibly explaining slight reduction in the yield strength of the materials.

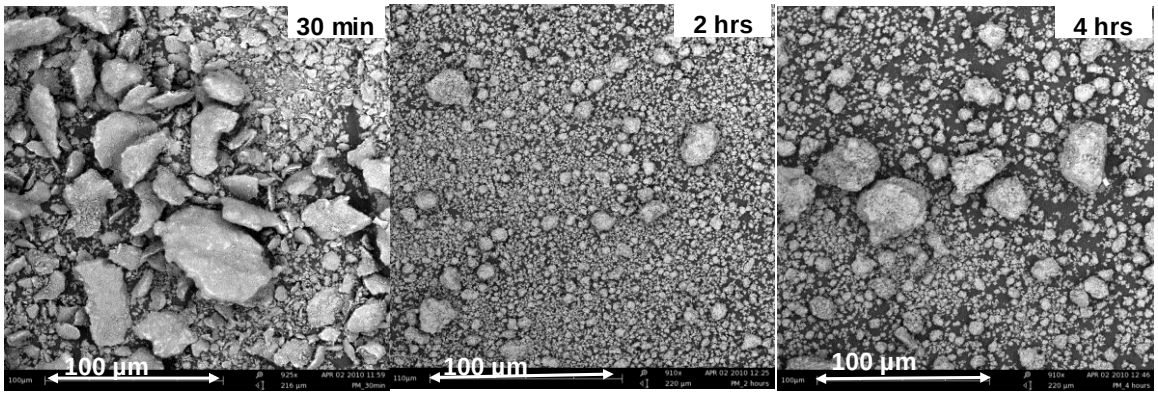

Figure 2.6 Backscattered electron images of milled aluminum-magnesium oxide composite powders prepared at different milling times using planetary mill operated at 350 rpm.

An increase in the yield strength above an arbitrarily selected value of 80 MPa, shown as a dashed line in Figure 2.5 occurred reproducibly for all cases following breaking down the flake-like particles. Yield strength just above this value was measured for the samples recovered after about 30 min milling from the shaker mill, after about 1 and 2 hours for the planetary mill operated 350 and 300 rpm, respectively, and after about 2 and 4 hours for the attritor mill operated at 400 and 200 rpm, respectively. No

significant difference in the particle sizes and shapes for the powders produced in different mills at the above mentioned milling times could be detected. It was assumed that the materials prepared by different mills are nearly identical. Therefore, it was possible to select achieving the yield strength of 80 MPa as an indicator of the material refinement. Milling times corresponding to the yield strength of 80 MPa achieved for different milling devices and conditions were obtained as times at which the experimental trends crossed the 80 MPa level, as shown in Figure 2.5. As discussed below, these times together with the respective energy dissipation rates, E_d, computed by DEM and masses of powder loaded in the vials, m_p, were used to estimate the milling dose, D_m, for each of the milling devices using equation (2.2). If the milling progress indicator is properly selected, and if the energy dissipation rates calculated by DEM are proportional to the milling progress, the value of D_m should be the same for all powders, indicating the same level of refinement achieved by ball milling.

2.4.2 Predicted Energy Dissipation Rate

It is interesting to begin analysis of the DEM calculation by comparing the average energy dissipation rates for different milling devices. Results in terms of energy dissipated in the entire milling vial averaged per 1 ms are shown in Figure 2.7.

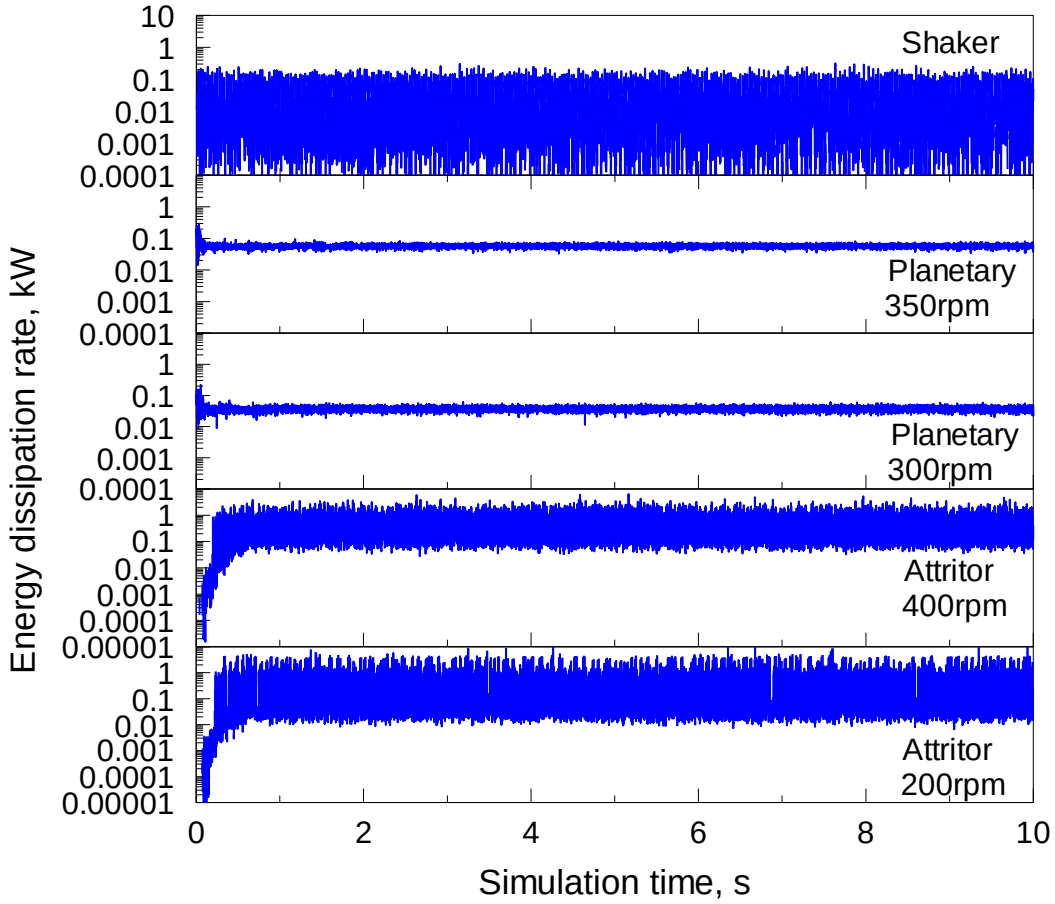

Figure 2.7 Energy dissipation averaged per 1 ms as a function of time for different milling conditions.

Fractions of the same traces are shown in the expanded time scale in Figure 2.8. A relatively short time interval over which the energy dissipation is averaged is selected to observe device-specific trends associated with particular ball motion patterns.

The energy dissipated in the shaker mill varies between very low and moderate values. Figure 2.8 suggests that the variations track the shaking motion of the vial and respective motion of balls flying in the vial side to side. The balls in flight effectively do not transfer any energy to the powder. When they strike the vial sides, the energy transfer

rates are substantially increased. For the planetary mill, the energy dissipation rates are remarkably steady. This is understood considering that the balls are continuously rolling along the vial surface. For the attritor mill, the energy dissipation rate is changing in a broad range. The lower bound for the energy dissipation rate is higher for the 400 rpm case as compared to 200 rpm case, as expected. However, multiple spikes with higher energy dissipation rate appear in both traces and might even be stronger for the 200 rpm case. Such spikes are formed when individual balls occasionally get jammed between other balls and impeller and then released after being significantly compressed. Thus, the energy predicted to be dissipated in such events may not be expended to refine the milled powder; instead it is likely to be transferred directly to the balls causing their heating and plastic deformation. Note that extended plastic deformation is not accounted for in the current DEM model assuming only a limited plasticity for the milling balls. It is also of interest to mention that events similar to the high-energy dissipation events observed here were also reported in Rydin et al. [59]. Nevertheless, unlike the present effort, Rydin et al. [59] referred to these events as “direct impacts” and were postulated to be more effective for powder refinement than lower energy rolling and sliding events.

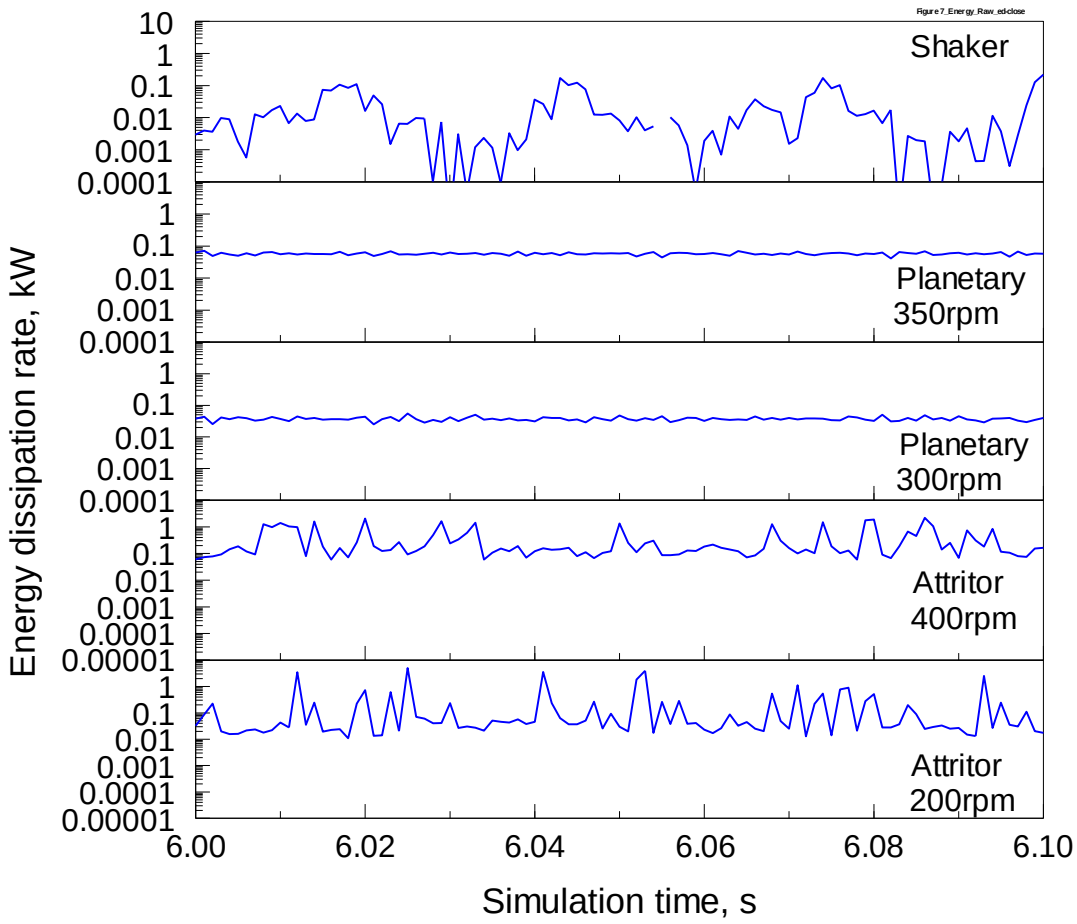

Figure 2.8 Energy dissipation averaged per 1 ms as a function of time for different milling conditions presented in the expanded time scale.

Using the calculated energy dissipation rates for all mills and milling conditions, it is possible to compare the predicted milling progress with that observed experimentally. Such a comparison is presented in Table 2.2.

Table 2.2 Data for Comparison of Predicted and Experimental Milling Progress and Milling Times

Parameters	**Milling Device**				
	Attritor		**Planetary**		**Shaker**
	200 rpm	**400 rpm**	**300 rpm**	**350 rpm**	**1054 rpm**
E_d/m_p, kW/g	8.3±1.5	10.0±1.0	1.3±0.004	1.9±0.05	4.8±0.2
Experimental milling time t_{exp}, to reach 80 Mpa yield strength, hrs	4.0±0.3	1.8±0.1	1.7±0.8	1.0±0.3	0.4±0.1
Milling dose, $D_m = \frac{E_d t_{\exp}}{m_p}$, kW·hr/g	33.3±8.0	18.0±2.8	2.1±1.0	1.9±0.6	1.9±0.5
Milling time, predicted, t_{pred}, hrs	0.23±0.08	0.19±0.06	1.5±0.46	1*	0.4±0.13

*Selected as the reference experiment for choosing the appropriate milling dose

The energy dissipation rates (shown normalized per sample mass, as E_d/m_p) were calculated as averages for five time intervals, 0.1 s each. The ranges shown in Table 2.2 represent standard deviations for the obtained average values. They represent the statistical variation in the DEM-calculated rates of energy dissipation. The ranges shown for the experimental milling time, t_{exp}, reflect the error bars shown in Figure 2.5. The values of milling dose calculated using equation (2.2) and experimental milling times are shown to illustrate the practical use of the DEM results. If one of the milling conditions is selected as a reference, prediction of the milling times required for all other conditions should be possible using the reference milling dose. For example, the experimental milling time of 1 hour observed for the planetary mill operated at 350 rpm is selected as

the reference. Using respective value of the milling dose of 1.9 kW·hr/g, milling times are obtained using equation (2.2) and are shown in Table 2.2.

Based on the milling dose concept, all milling dose values in Table 2.2 are expected to be identical to one another, considering that for all experiments, the experimental milling time is taken as that required to achieve 80 MPa in yield strength for all prepared materials. Indeed, within the expected error, the milling dose values are identical to one another for the shaker mill and for both rpm values used for the planetary mill. However, the predicted milling dose values for both rpm's used for the attritor mill are substantially greater than anticipated. Therefore, using the planetary mill operated at 350 rpm as a reference milling condition would result in significant under-predictions of the milling times required for obtaining the same material in the attritor mill. The reasons for this discrepancy and an approach to correct for it are discussed below.

2.5. Discussion

In order to understand the reasons for the apparent discrepancy between predictions and experimental data, especially substantial for the attritor mill, it is useful to closely examine how the energy dissipation from the milling tools occurs for each milling condition. Energy is dissipated in discrete events or collisions. Each event is identified when milling balls touch each other or touch the milling vial. As a first step, the energy dissipation events for each milling condition were sorted based on the average force

exerted between interacting elements and based on the event duration. The results of the above two classifications are shown in Figures 2.9 and 2.10, respectively. The event statistics shown in Figures 2.9 and 2.10 represent results of DEM calculations for 10 s of milling.

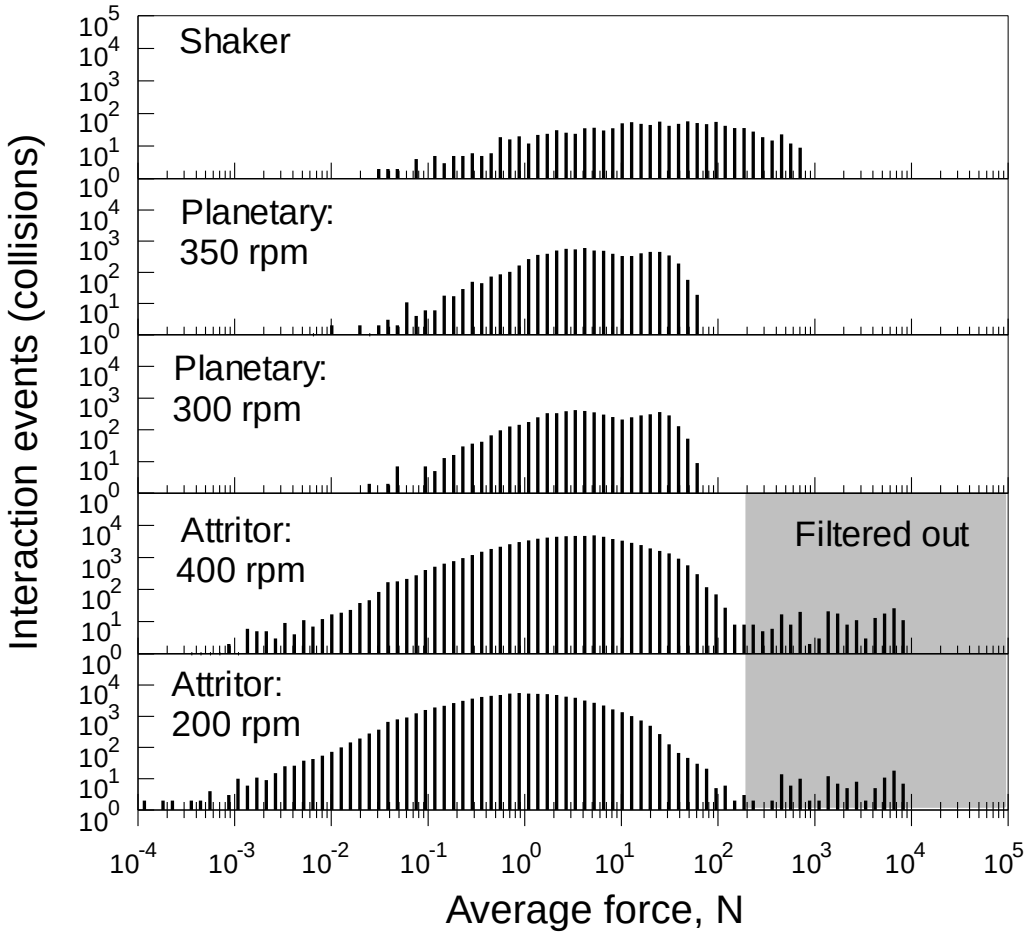

Figure 2.9 Histograms sorting interaction events of milling tools based on the average force.

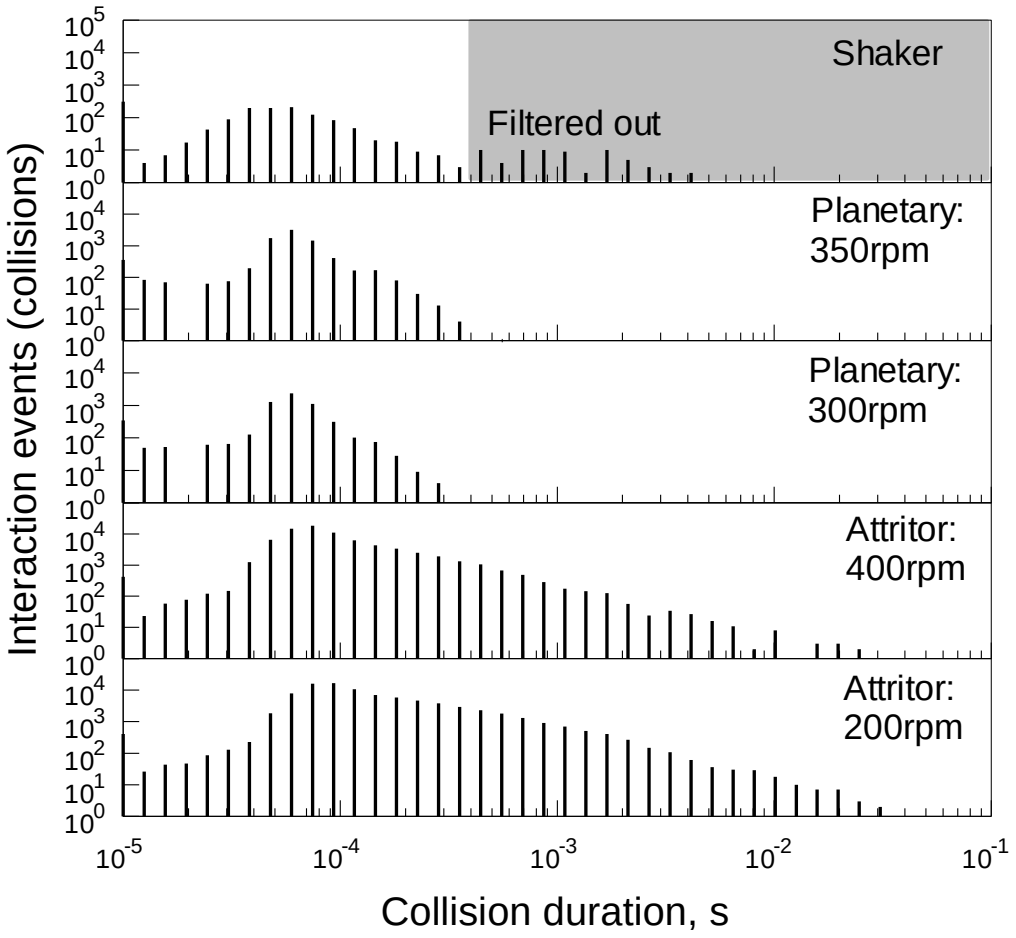

Figure 2.10 Histograms sorting interaction events of milling tools based on the event duration.

Histograms representing the number of interaction events sorted based on the average force shown in Figure 2.9 are very similar to those obtained by sorting the interaction events based on the maximum force (not shown for brevity). The range of forces predicted to develop in the milling tool interactions for the planetary mill is relatively narrow. This is readily understood considering that the ball motion pattern in this case is most regular, compared to other milling devices. Somewhat greater forces are observed for the shaker mill. This is also expected considering that such greater forces

result from multiple head-on collisions occurring in that device. The histograms observed for the attritor mill exhibit multiple events characterized by very low forces. This is likely associated with collective ball motion. The high-force end of the histograms for the attritor appears to be irregular. It is apparent that the main distribution ends for events in which forces are between 100 and 1000 N, similar to the high-force distribution edges for the other milling devices. However, a high-force "tail" is also observed indicating a relatively large number of events with very large forces. A close examination of such individual interaction events shows that these are the same events causing spikes in the energy dissipation traces (Figures 2.7 and 2.8) or "direct impacts" according to Rydin et al. [59]. These events occur when an individual ball gets caught among other balls and is severely compressed as the impeller continues pressing the balls together. As discussed above, such events may indeed occur in experiment; however, the energy dissipated in compression and release of such balls is unlikely to be transferred to the milled powder. Therefore, it is of interest to filter out such events from the overall energy dissipation analysis. The region proposed to be filtered out is shown in gray in Figure 2.9.

A similar examination of histograms showing interaction events sorted by the event duration (Figure 2.10) suggests that some irregularity exists for the shaker mill, for which the histogram appears to be by-modal. It is interesting that for all histograms, the main peak occurs for durations under 0.1 ms, with the peak position shifting to longer durations from the shaker mill to planetary and then to attritor mill. The distribution is

relatively narrow for the planetary mill. The right-side edge of the planetary mill histogram effectively coincides with the right side edge of the first histogram peak observed for the shaker mill. It is observed that longer interaction events for the shaker mill occur when the balls roll along the vial surface. As was shown by Ward et al. [36], only a very small energy is dissipated in such events, and this fraction of the energy dissipation does not correlate with the material refinement observed experimentally. According to recommendations of Ward et al. [36], such interaction events can also be filtered out from the analysis of the energy dissipation. However, unlike the high force interaction events filtered out for the attritor mill, removing of the low-energy collisions for the shaker mill is not expected to appreciably change the total energy dissipation.

The effects of different types of interaction events on the energy dissipation rates predicted by DEM can be seen clearly considering cumulative distributions of the energy dissipation rates as a function of the force and collision duration. These cumulative distributions are shown in Figures 2.11 and 2.12, respectively.

As shown in Figure 2.11, for the planetary mill most of the energy is dissipated in relatively weak collisions. For the shaker mill, the energy is dissipated in collisions with greater force. Filtering out longer collisions hardly changes the cumulative distribution curve for the shaker mill. For the attritor mill, the distributions are somewhat peculiar. The fraction of dissipated energy increases, as for the planetary mill, while the interaction force increases to about 100 N. No head-on collisions produced by airborne balls (as in

the shaker mill) occur, so the fraction of the dissipated energy does not increase appreciably as the force increases further. However, for very large forces, exceeding approximately 1000 N, the energy dissipation rates predicted by DEM increase dramatically. Clearly, removing such interaction events from analysis would drastically reduce the energy dissipation rate and respective value of the milling dose, resulting in reducing the discrepancy observed in Table 2.2.

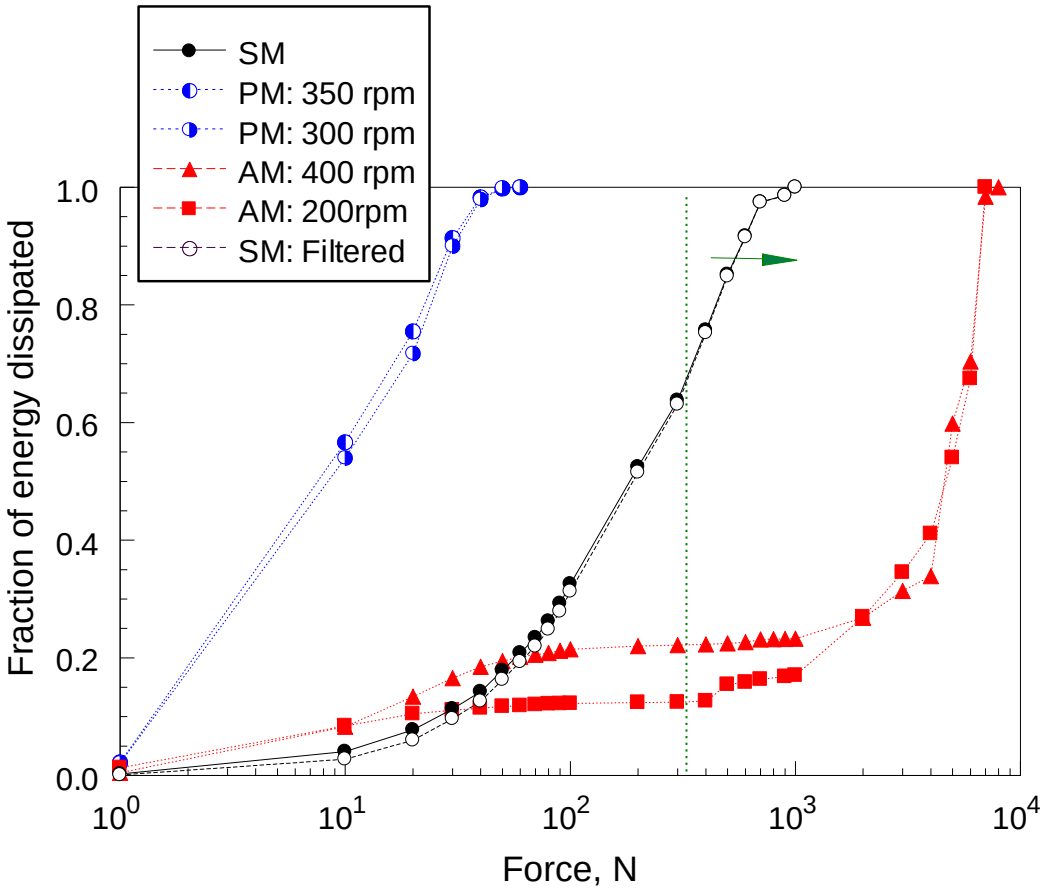

Figure 2.11 Fraction of energy dissipated in different mills as a function of average force observed in individual events of milling tools interaction.

In addition to be characterized by the very high forces, the collisions that need to be filtered out are very long. Indeed, the time required to compress the ball that is jammed among other balls is relatively long, much longer than a typical interaction resulting in refinement of the powder present on the surfaces of the colliding balls, vial or impeller. Indeed, examining the cumulative distributions shown in Figure 2.12, it can be noticed that for all devices, the fraction of the dissipated energy increases continuously as the interaction events increase to about 1 ms. For both shaker and planetary mills, longer interactions are unimportant. However, for the attritor mill, fraction of the dissipated energy increases dramatically for much longer interaction events. Importantly, when the events characterized by the abnormally high forces are filtered out (as suggested in Figure 2.9), it is observed that the longer interaction events disappear as well.

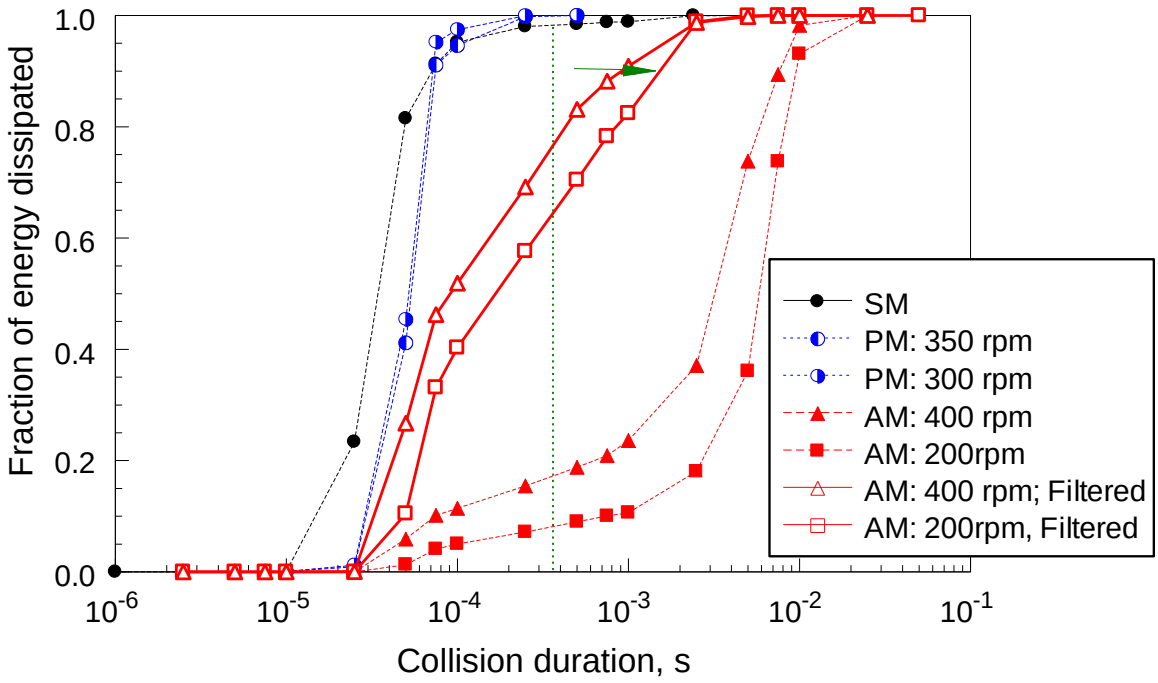

Figure 2.12 Fraction of energy dissipated in different mills as a function of duration of individual events of milling tools interaction.

The milling dose can now be recalculated considering the DEM results corrected by removing the interaction events with abnormally high forces occurring for the attritor mill. For completeness, one can also consider the effect of correction resulting from removal of longer collisions (second peak in the histogram shown in Figure 2.10) for the shaker mill. The corrected results are shown in Table 2.3. For completeness, experimental milling times shown in Table 2.2 and used to calculate the corrected milling dose are repeated in Table 2.3. The discrepancy between different milling devices is substantially reduced.

Table 2.3 Corrected Data for Comparison of Predicted and Experimental Milling Progress

Parameters	Milling device				
	Attritor		Planetary		Shaker
	200 rpm	400 rpm	300 rpm	350 rpm	1054 rpm
Corrected E^*_d/m_p, kW/g	0.4±0.002	1.7±0.06	1.3±0.01	2.0±0.04	4.6±0.1
Experimental milling time t_{exp}, to reach 80 MPa yield strength, hrs	4.0±0.3	1.8±0.1	1.7±0.8	1.0±0.3	0.4±0.1
Corrected milling dose, $D^*_m = \frac{E^*_d t_{\exp}}{m_p}$, kW·hr/g	1.6±0.1	3.06±0.3	2.1±1.0	2.0±0.6	1.8±0.5
Milling time, predicted, t_{pred}, hrs	5.6±1.8	1.2±0.4	1.6±0.5	1	0.4±0.14

2.6. Conclusions

In order to obtain a useful DEM description of the milling process, experimentally validated values for restitution and friction coefficients are necessary. Both static and rolling friction coefficients were obtained comparing simple experiments with powder-coated milling balls rolling inside the milling vial versus respective DEM model. Milling dose defined as the ratio of the energy transferred to the powder from the milling tools to the mass of the milled powder provides a useful description of the milling progress for different devices and milling conditions. The DEM-calculated rate of energy dissipation multiplied by the experimental milling time enables one to calculate the

energy transferred to the powder from the milling tools. This energy determines the material refinement. Once it is found for a material prepared in a specific milling configuration, it can be used for predicting milling time required to prepare that material using a new milling device or altered milling conditions. No corrections or adjustments to the DEM calculations are necessary for both planetary and shaker mills. For attritor mill, the rate of energy dissipation predicted by DEM includes substantial contribution from the milling tool interaction events accompanied by abnormally high forces ($>10^3$ N) and continuing for times exceeding 1 ms. Such events are associated with jamming milling balls and their subsequent release at relatively high velocities. Because of very high forces developed in such events, the energy is likely dissipated to heat or plastically deform the milling tools rather than refine the milled material. Therefore, it is proposed to filter out such high-force, long duration events from further analysis of powder refinement in the attritor mill. Such filtering enables one to obtain a much better correlation of the experimentally achieved powder refinement with DEM prediction. Milling dose implied by the filtered DEM calculations for attritor mill becomes comparable to that obtained for both shaker and planetary mills when all three milling devices are used to achieve the same degree of material refinement.

CHAPTER 3

REAL TIME INDICATORS OF MATERIAL REFINEMENT IN AN ATTRITOR MILL

3.1 Introduction

Mechanical milling is widely used for the preparation of various advanced materials [4]. Material is refined and modified as a result of multiple interactions with milling balls occurring at different impact energies and configurations. Most commonly, the milling progress is assessed by recovery of partially milled samples at regular time intervals. Such samples are evaluated based on their particle sizes, shapes, crystal structures, or mechanical properties to establish the time necessary to prepare the required material [52, 53, 60]. This approach is labor-intensive, and more streamlined methods capable of quantifying the milling progress are desired.

In the past, several research groups have realized the difficulty in such tedious experimental methodologies and tried to identify simpler approaches. Some of the parameters investigated to aid in understanding milling process include measurement of power consumption and torque from the motor attached to the mill [61-64], measurement of temperature inside the milling vial [35, 36, 62], measurement of vibration frequency, amplitude of the vial and impact frequency of ball [65], and visualization by recording high speed videos of the milling process [59].

One of the early attempts at such real-time diagnostics was by R Goodson et al. [61], who utilized Charles equation correlating the specific energy input to the mill E (in kW.hr/ton or W. hr/Kg), and median particle size d_p (in micron), ($E=Ad_p^{\alpha}$), where A and α are parametric constants. The milling experiment was carried out using a laboratory attritor and the sample was a mixture of tungsten carbide and cobalt (6 wt% and 12 wt%) powders. Three different milling conditions were monitored: control run at 125 rpm, run with 25% less balls and high speed run at 200 rpm. The specific energy input data for the Charles equation was obtained from the power draw for the mill. The idea was to be able to postulate the appropriate milling parameters for the final products of the desired size range. The energy input as a function of different filling of the vial volume was also measured. After milling, the powder samples were pressed and vacuum sintered. The density, coercivity, Rockwell hardness and specific magnetic saturation of milled and sintered cylinders were measured as functions of milling time. As an initial attempt, the established correlation between the specific energy input and median particle sizes seems reasonable. However, the theory has not been extended to other materials of interest. Also, it is concluded that the desired final product size can be predicted solely based on the Charles equations and hence, the energy input to the mill alone. In other words, an independence of the final product on milling conditions is claimed, but this major comment has not been not thoroughly validated.

Kimura and Takada [62] set up a data acquisition system on a custom rotating arm ball mill (similar in operation to the attritor mill used in this work). Apart from the torque on the rotating arm, the temperature inside the vial was also monitored as a function of milling time. The aim was to track a solid-state amorphization transformation in Co-Zn alloys. The measured torque was established to be sensitive to changes in powder structure, whereas the attrition temperature was proposed to be a direct indicator of the kinetics of solid-state amorphizing transformations. Overall, the only major outcome is that when there is a reduction in the torque and a spike in the temperature, this would indicate that an exothermic solid-state reaction has occurred in the powders. Apart from this result, which is specific to the material system under consideration, no diagnostic methodology with universal appeal was developed. Besides, the same theory was not extended to other systems with similar amorphization reactions as a further proof of concept. Although the data acquisition seems to be reasonably sensitive to changes in the mill, the milling device itself is not commercial available for use.

Temperature measurement was also considered as a reaction progress monitor in some of the earlier projects from the present research group [35, 36]. The systems under consideration included mechanically alloyed Al-Mg powders as well as materials capable of highly exothermic reactions. Both shaker and planetary mills were instrumented to read out the vial temperature. For the mechanically alloyed powders, the temperature measurement was useful in establishing different stages of the milling process, e.g.,

formation of flake-like particles, breaking down the flakes, and formation of composite and then alloyed powders [66]. For the exothermically reacting materials, as is common in reactive milling [67], the temperature jump in the milling vial may show directly and very clearly when the reaction has occurred.

Mulas et. al [65] employed a piezoelectric transducer and magnetic position sensor to measure impact frequency, impact time and vial velocity in a single-ball vibro-mill and a shaker mill. The primary objective was to establish the right amount of energy and thereby, milling parameters necessary to initiate a self-propagating reaction in the materials system under consideration.

Iossana and Magini reported electrical and mechanical power consumption measurements on a planetary mill in their two successive papers [63, 64]. Their work stemmed from the interest in comparing the theoretical energy consumption in a ball milling process based on mechanistic collision models to that from experimental power consumption measurement. The authors established a satisfactory correlation between the two for a planetary ball mill and suggested that the same concept could be extended to other devices.

In summary, the utility of the real-time measurements of the consumed power, vial temperature and some of the other characteristics of the milling process has been well established. Most successful real time measurements indicated qualitative changes in the material properties, such as formation or destruction of flakes and occurrence of

exothermic, self-sustaining chemical reactions. However, detection of more subtle changes in the materials properties, e.g., evolution of the particle sizes, development of the alloyed phases, altering mechanical strength and hardness, has proven to be more challenging. Most related measurements were performed for specific materials systems and customized milling configurations. Thus, it remains unclear whether such trends, identified rather narrowly for specific materials systems and milling devices, are capable of predicting milling progress for different materials or different milling configuration.

It is also interesting that many related efforts involved shaker and planetary mills, devices that are very common in laboratory experiments, but not readily scalable for commercial manufacturing. Conversely, the data on correlations between real time power consumption and torque and material refinement in the attritor mills are very difficult to find, whereas attritors are most likely to be used in larger scale production of new materials. This lack of data for attritor mills is especially surprising considering that some of the popular commercial attritor mill models, e.g., by Union Process, are routinely equipped with sensors and a data acquisition board, enabling users to read and record power, rotation rate, and torque readily.

This project is aimed to establish an experimental foundation for assessing milling progress while preparing materials in an attritor mill utilizing non-invasive, real time process indicators. A systematic approach is proposed, relying on simultaneous measurements of the motor torque, power, and rotation speed (rpm) during preparation of

mechanically milled materials. In addition to assessing the milling process parameters averaged on the time scale comparable to the overall milling time, short-time deviations of these parameters are also considered to help describing milling dynamics. Such time-resolved data affected by ongoing changes in the material properties might be particularly useful when comparing experiments with numerical descriptions of the ball milling process, e.g., using a discrete element model-based approach [35, 36, 38, 60].

Changes in the time-averaged values of real-time indicators are compared to changes in the structure and mechanical properties of the milled materials. Two materials with distinctly different characteristics are selected for this study. Both materials are metal matrix composites consisting of ductile and brittle components. Selected material compositions are chemically inert, and hence no new compounds could have formed affecting the mechanical properties of the products. Therefore, work hardening and powder morphology evolving as a result of milling were the only parameters affecting mechanical properties of the prepared composite powders. The brittle components were chosen to have substantially different hardness to investigate its effect on both the milling progress and milling parameters measured in real time.

3.2 Experimental

3.2.1 Materials

Prepared composite powders included aluminum, as a ductile component, containing inclusions of one of the brittle components: magnesium oxide or boron carbide. Pure aluminum powder (-325 mesh, 99.9% pure Atlantic Equipment Engineers) served as a starting material for the milling. Starting materials for brittle inclusions were magnesium oxide (-325 mesh, 99% pure, by Aldrich Chemical Company, Inc) and boron carbide (<10 Micron Powder, 99% pure, by Alfa Aesar). As was shown in earlier experiments [60, 68, 69], during milling, aluminum does not react chemically with either MgO or B_4C, and the milling yields Al·MgO and Al·B_4C dispersion-strengthened composites. The compositions for both materials included 30 wt. % of the brittle component. Mechanical properties of the starting components as well as those of the hardened steel milling balls used in experiments are shown in Table 3.1.

Table 3.1 Material Properties of Pure Powders in Comparison to Milling Media [18]

Property	Al	MgO	B_4C	Hardened steel
Vicker's hardness, MPa	167	660	4980	1700-2300
Shear modulus, GPa	25.9	87-124	192	~80
Poisson's ratio	0.31	0.36	0.21	0.28
Density, g/cc	2.7	3.75	2.51	7.8

The milling media material (hardened steel) is harder than magnesium oxide but is softer than boron carbide.

3.2.2 Milling Devices and Conditions

An attritor mill by Union Process, model 01HD, was used in this study. The milling vial volume is 750 mL. It is a stationary vial made of hardened steel. A steel impeller rotating at an assigned speed agitates the milling balls. The vial was cooled by room temperature water. Further details on the geometry of the mill can be found elsewhere [60].

Case hardened carbon steel balls of 9.5 mm diameter were used. The ball to powder mass ratio was 36, powder mass used was 50 g and the rotation speed of the impeller was 400 rpm. The total milling durations used to prepare the Al·MgO and Al·B_4C composite materials were 4 and 6 hours, respectively. Partially milled samples were recovered every 1 hour for mechanical and structural characterization. For some experiments, samples were also recovered and examined in 30-min milling intervals.

3.3 Milling Progress Indicators

3.3.1 Material Characteristics

Various material parameters, including particle size, dimensions of the formed inclusions, mechanical characteristics, or crystallographic characteristics can be used as indicators of refinement achieved as a result of milling. In this study, both mechanical and structural characteristics were exploited. Specifically, yield strength measured while preparing consolidated powder samples and a width for an aluminum peak in the x-ray diffraction (XRD) patterns were determined.

In mechanically milled composites, the yield strength typically increases as milling progresses due to formation of dispersion-strengthened materials. The crystallite sizes decrease when the material becomes more refined, e.g., as a result of a longer milling time. In the XRD measurements, wider peaks correspond to more refined materials. Hence, an increase in the peak width with time is expected.

The methodology to obtain the yield strength was presented in section 2.3.2 and is only briefly outlined here. The powder is compacted in a cylindrical die and the displacement is obtained as a function of the applied load using Instron 5567. The compression curves are re-plotted in terms of inverse porosity as a function of pressure; obtained trends are interpreted using a modified Heckel equation [55], in which yield strength is treated as an adjustable parameter.

XRD experiments were performed on a Phillips X'pert MRD powder diffractometer operated at 45 kV and 45 mA using Cu-*Kά* radiation (λ =1.5438 Å). A typical pattern for the aluminum-boron carbide sample is shown in Figure 3.1. The peaks for which the widths are indicated belong to the aluminum XRD pattern (38.5º and 44.5º). The peak width is measured at the level equal to half of its maximum height, also known as the Full Width Half Max (FWHM). Results for both aluminum peak widths were consistent to each other, so only the FWHM values for the peak at 44.5º are presented.

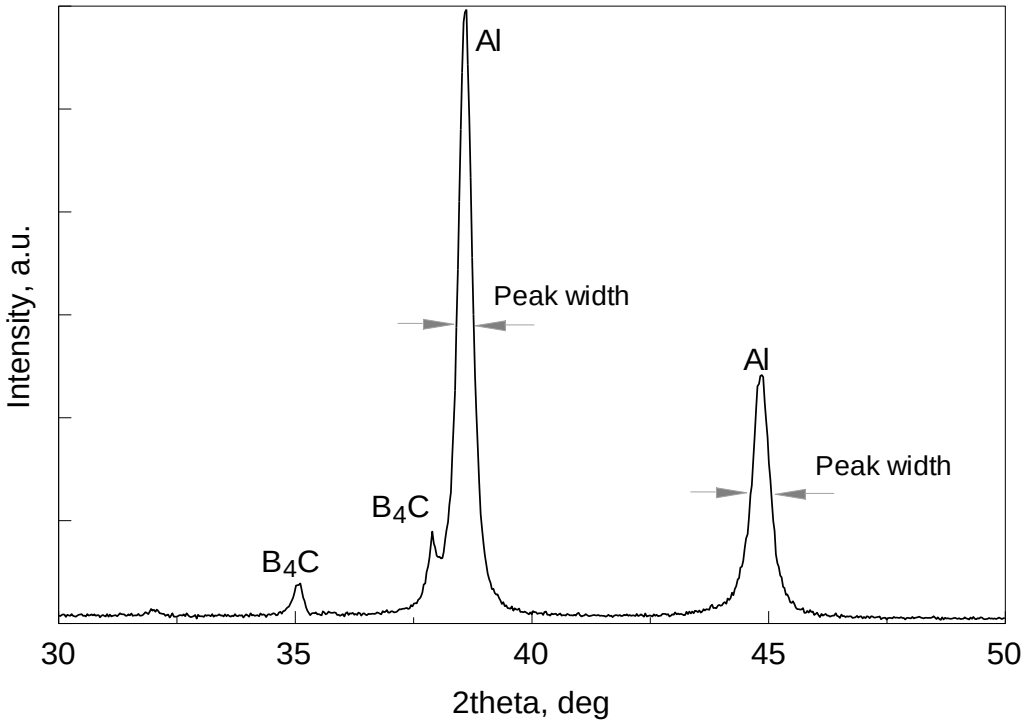

Figure 3.1 X-ray diffraction pattern for Al·B_4C sample recovered from the attritor mill after 2 hours; the FWHM is marked.

3.3.2 Real time milling progress indicators

A data acquisition system by Baldor is built in the control unit of the Union Process HD-01 attritor mill. The parameters measured include speed of rotation (rpm), power, and torque. These measurements, readily available for the attritor mill, were considered in the present paper. The data were recorded after different milling times in 10-s bursts with 1 ms time resolution. Figure 3.2 shows typical acquired signals.

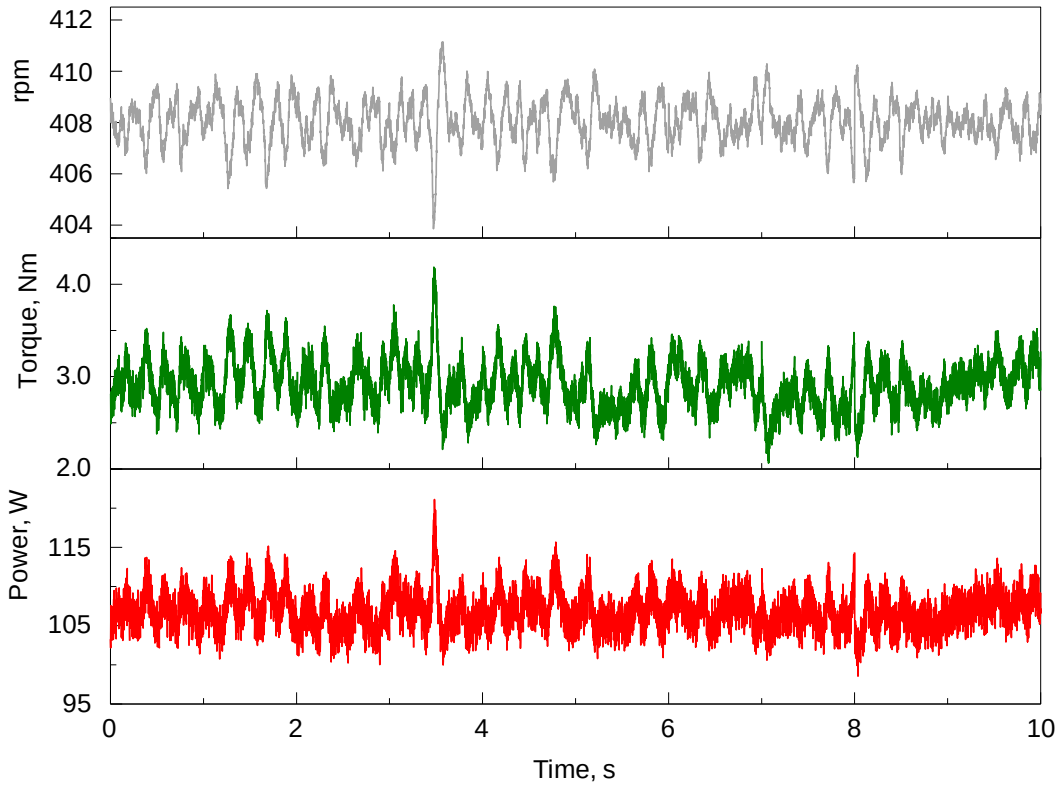

Figure 3.2 Real-time milling process parameters recorded for an Al·B_4C sample after its 2-hour milling.

3.4 Results

3.4.1 Particle Shapes and Sizes

Powders were recovered every 1-hour for both materials and back-scattered Scanning Electron Microscopy (SEM) images were taken. The SEM images of samples obtained at certain milling times are presented in Figures 3.3-3.5 to illustrate the evolution of the particle shapes. In all of these images, a) corresponds to the Al·MgO and b) is Al·B_4C. Also, the pictures on the left and right in each figure indicate the same sample shown at two different magnifications (scale shown at the bottom of each image). The milling times are indicated in the top left corner of each picture.

For both materials a qualitatively similar evolution in the particle morphology as a function of the milling times is observed. It can be broken down into the three steps:

1) Formation of flake-like particles (Figures 3a and 3b for Al·MgO and Al·B_4C respectively)

2) Breaking down the flakes into smaller, more equi-axial fragments (Fig 4a and Fig4b for Al·MgO and Al·B_4C respectively),

3) Agglomeration of the produced fragments into larger particles with relatively stable sizes. (Figures 3.5a and 3.5b for Al·MgO and Al·B_4C respectively)

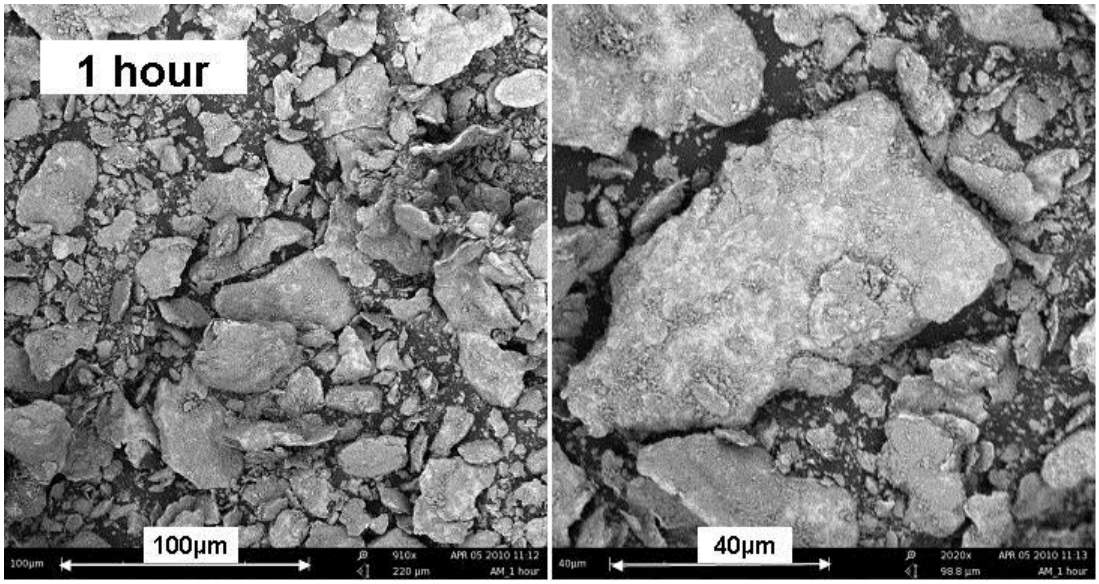

Figure 3.3a) Al·MgO SEM images of samples recovered after 1 hour of milling.

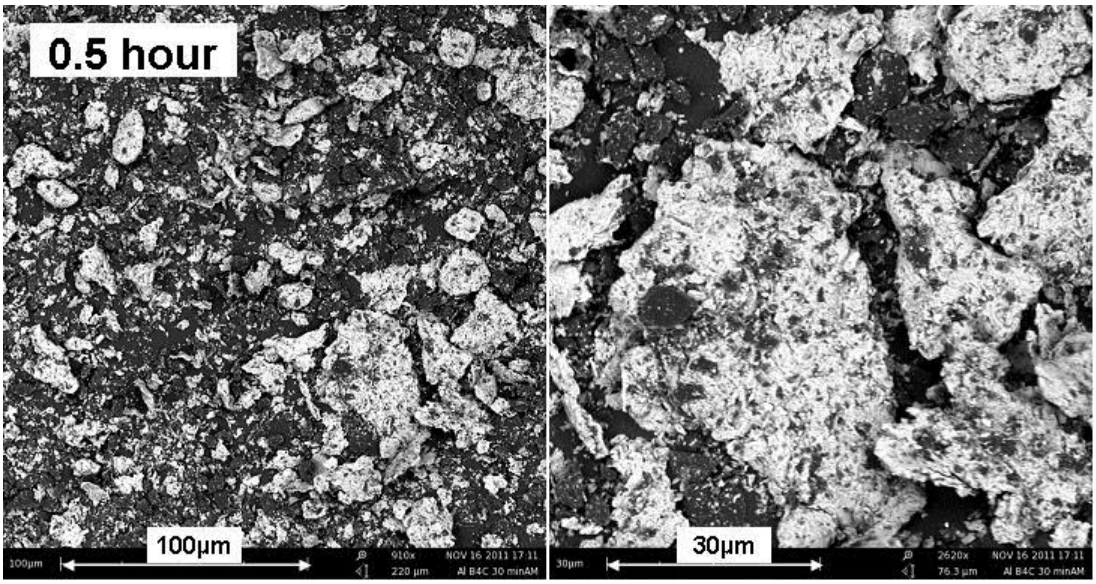

Figure 3.3b) Al·B_4C SEM images of samples recovered after 0.5 hour of milling.

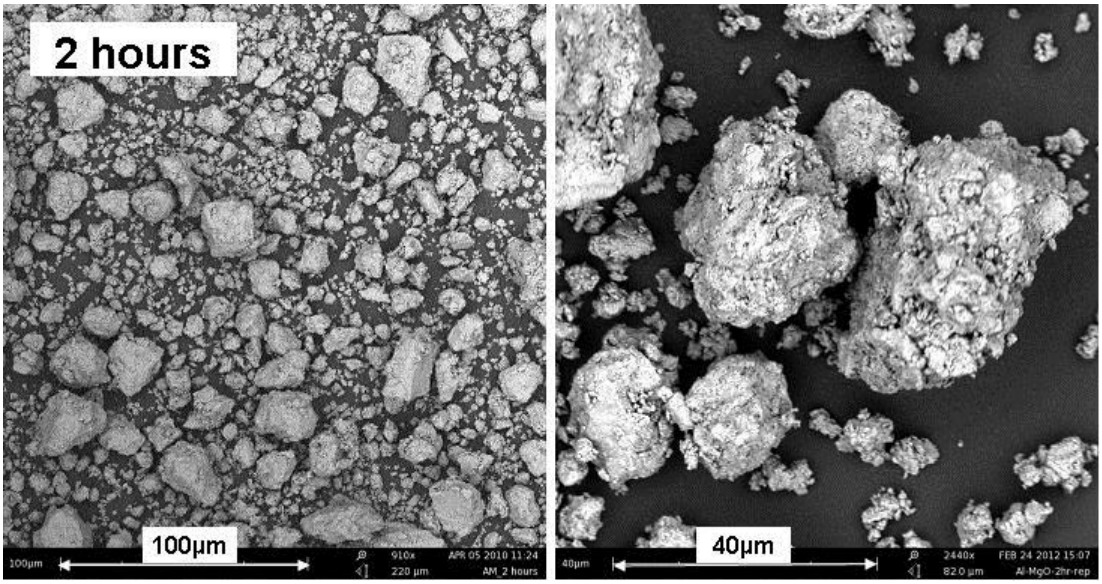

Figure 3.4a) Al·MgO SEM images of samples recovered after 2 hours of milling.

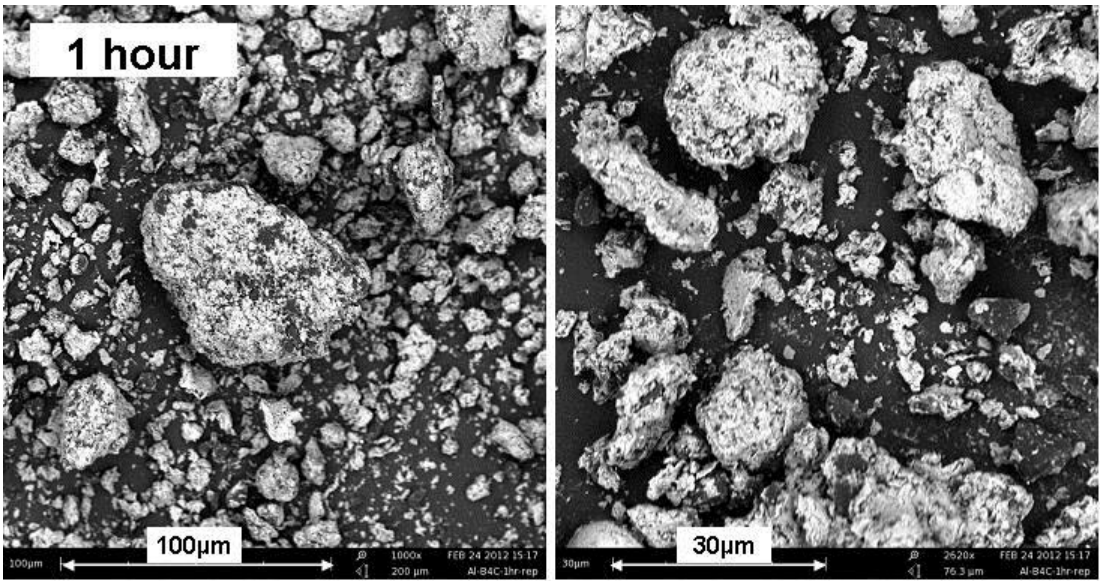

Figure 3.4b) Al·B_4C SEM images of samples recovered after 1 hour of milling.

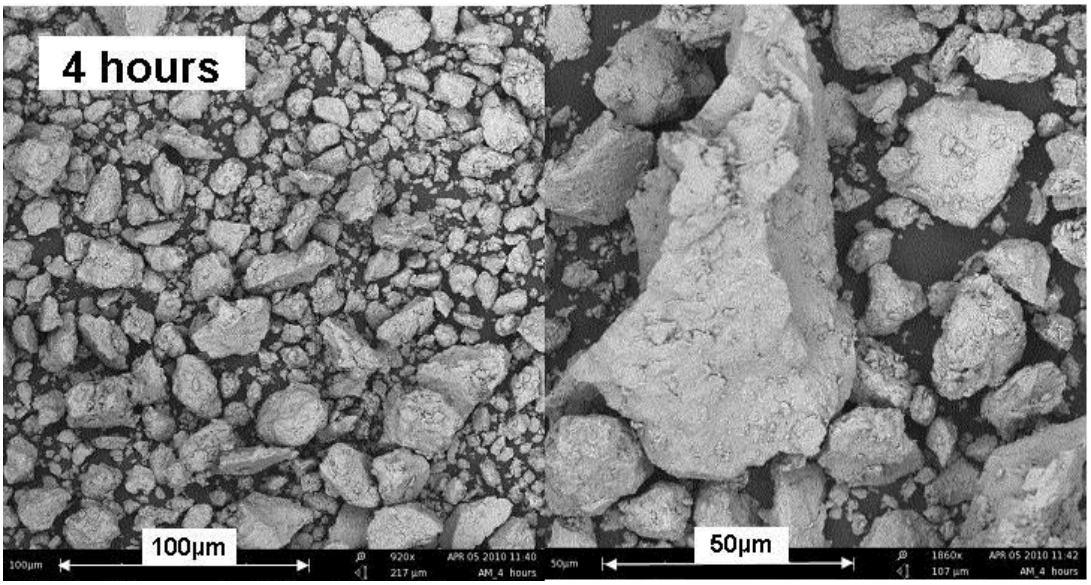

Figure 3.5a) Al·MgO SEM images of samples recovered after 4 hours of milling.

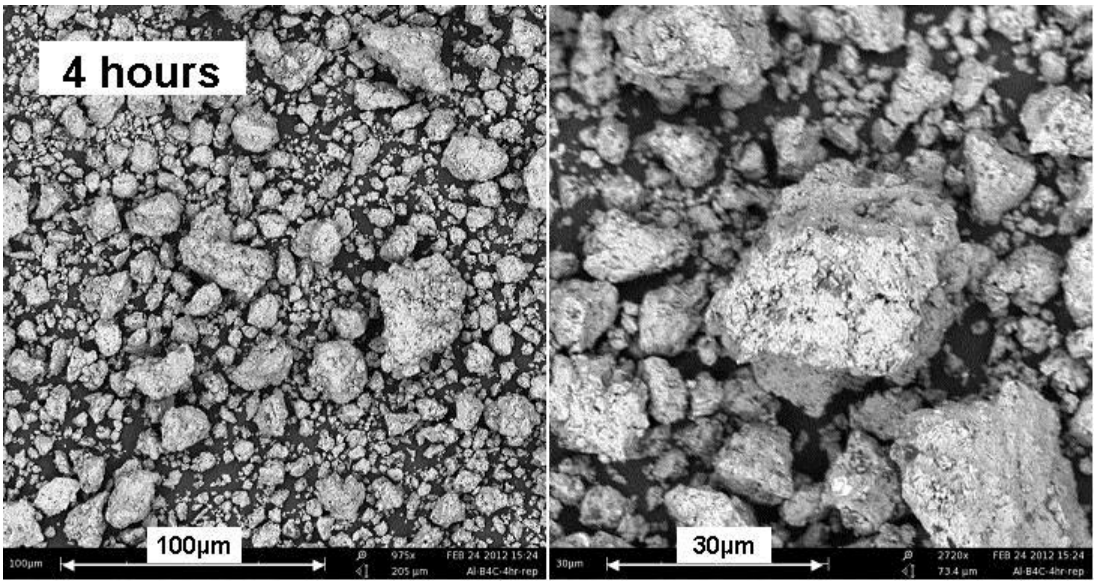

Figure 3.5b) Al·B_4C SEM images of samples recovered after 4 hours of milling.

Within this overall sequence, there were important differences between materials with different compositions. The agglomeration of the broken flake fragments occurred much sooner for Al·B_4C compared to Al·MgO, resulting in the substantially larger dimensions of the stabilized agglomerates of the former compared to latter. Second, the surface of flakes and surface of the formed agglomerated particles was relatively homogeneous for Al·MgO (Figures 3.3a, 3.4a and 3.5a); conversely, inclusions of B_4C were clearly visible at the surface of the Al·B_4C composite particles (Figures 3.3b, 3.4b and 3.5b). Furthermore, unattached B_4C were detected in the Al·B_4C composite material until 1 hr of milling (Figure 3.4b), while unattached MgO particles could not be detected in any of the inspected, partially milled samples.

3.4.2 Yield Strength

The yield strengths for both prepared composite powders as a function of milling time are presented in Figure 3.5.

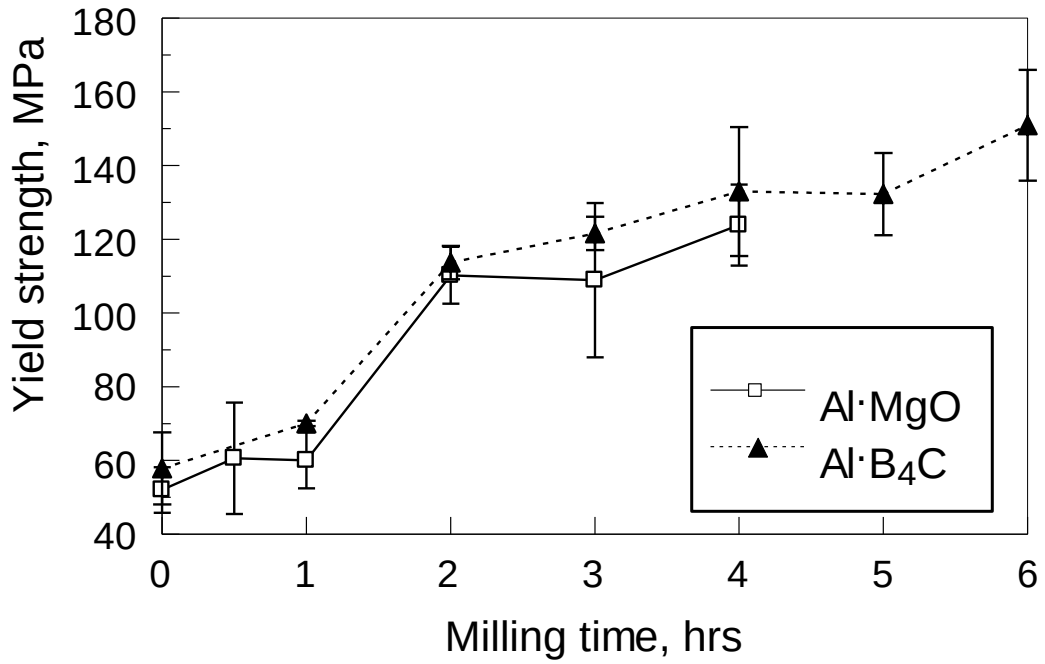

Figure 3.6 Yield strength for Al·MgO and Al·B_4C samples recovered at different milling times.

Each data point is an average of 6 measurements representing 6 consolidated pellets for Al·MgO and 3 measurements/pellets for Al·B_4C. In both the cases, at very short milling times the yield strength is small. This is associated with formation of Al flakes as presented in the SEM images in Figure 3.3, while aluminum is not yet work hardened. The flakes are readily deformed under pressure, resulting in lower measured yield strength. As the milling continues, the flakes are broken apart and composite

particles form. This is accompanied by an increase in the yield strength. This increase is substantial for both materials. Also, upon further milling, the yield strength appears to stabilize for both cases.

3.4.3 X-ray peak width

Figure 3.7 shows the widths of aluminum peaks or FWHM for the two materials as a function of milling time.

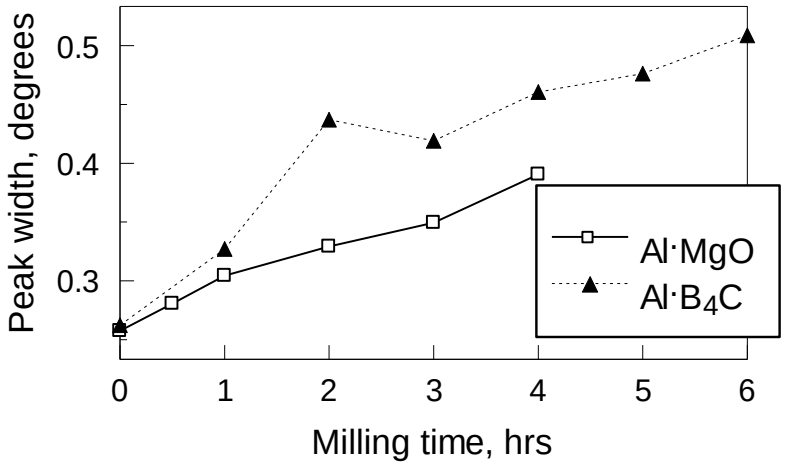

Figure 3.7 FWHM for aluminum XRD peak at 44.5º as a function of milling time.

The overall trends in Figure 3.7 show that the peak width increases as a function of milling time, indicating formation of increasingly more structurally refined materials. The structural refinement appears to occur from the very beginning of the milling process and is unaffected by the formation of flakes at short milling times. For Al·MgO, the refinement of aluminum crystal grains is slower than that for Al·B_4C. Also, the final peak

width achieved is greater for Al·B_4C. These observations are likely explained by a greater effectiveness of boron carbide inclusions as milling aids accelerating the fracture propagation in the composite particles as compared to softer inclusions of MgO.

3.4.4 Real-time measurements

The fractions of data presented in Figure 3.2 are shown at an expanded time scale in Figure 3.8. Changes in power and torque occur in phase with each other whereas changes in rpm occur in the opposite phase. The main period of the observed oscillations, approximately 0.15 s, correlates with the period of the impeller's rotation set at 400 rpm. At different milling times, average values of the measured power, torque, and rpm changed, and these changes were explored as possible indicators of the milling progress. In addition to the change in the average values of the measured parameters, changes in the amplitudes of their respective oscillations were also noticed. The latter changes were quantified considering standard deviations of the measured parameters taken over a period of 10 s.

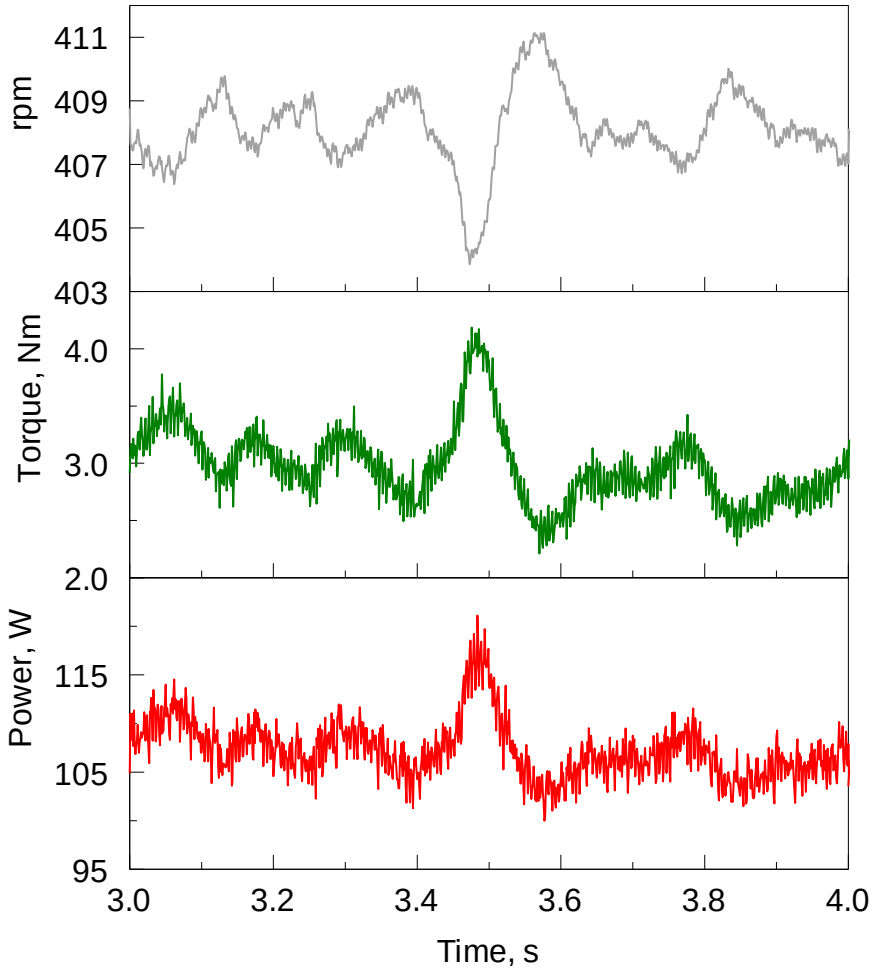

Figure 3.8 Real-time milling process parameters recorded for an Al·B_4C sample after its 2-hour milling (Fig. 2) shown with an expanded time scale.

The processed results of real time measurements for both material systems are shown in Figure 3.9. The standard deviations in rpm are shown instead of the relatively stable average rpm values. The standard deviations for torque and power follow trends similar to the standard deviations for rpm and hence are not shown in separate plots; however, these standard deviations are represented by the error bars for their respective average values shown in Figure 3.9.

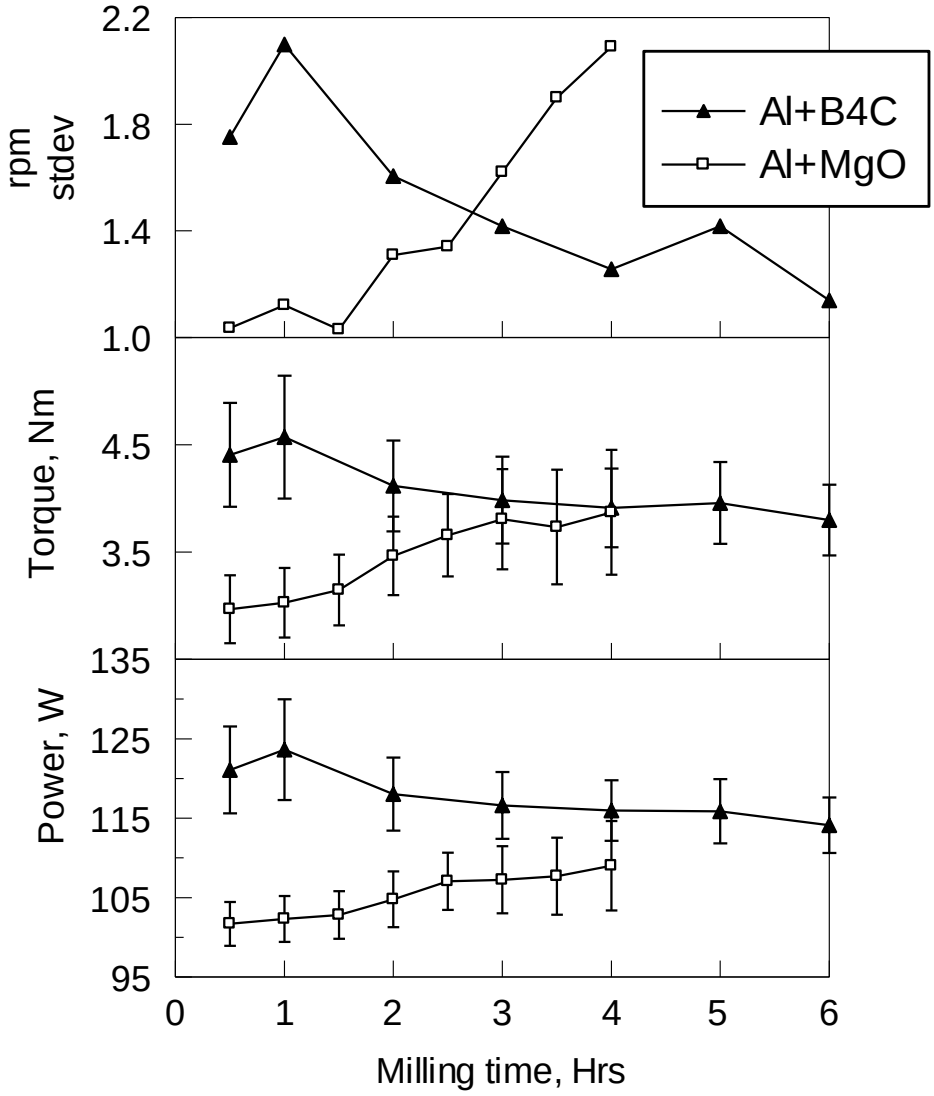

Figure 3.9 Average values and corresponding standard deviations for real-time indicators measured to assess milling progress as a function of the milling time.

All three parameters tracked, including power, torque, and standard deviation of rpm, show opposite time-dependent trends for the two materials systems studied. There is an increase in rpm variations, torque and power for the aluminum-magnesium oxide system as a function of the milling time; however, the same process indicators consistently decrease with milling time for the aluminum-boron carbide composite. Also,

despite identical milling conditions, the initial values for all three real time indicators are much higher at the outset for the boron carbide system.

This disparity in the trends between the two materials is likely a consequence of the different refinement mechanisms in the two powders. This is turn, is attributed to the difference in properties as shown in Table 3.1 and discussed below.

3.5 Discussion

It is first interesting to directly correlate changes in the powder characteristics, yield strength and FWHM, with changes in the milling process parameters measured in-situ. Because measured changes in power, torque, and standard deviation for rpm are well correlated with one another for each material, as shown in Figure 3.9, only changes in power are taken for direct comparison with yield strength and FWHM. These correlations are shown for both materials in Figure 3.10. Please note that vertical scales for power are different for different materials.

For Al·MgO composite, changes in all three trends, presented in Figure 3.10, correlate with one another. As the powder becomes more and more refined and work hardened, the power required to maintain the preset rpm increases, as indicated by the observed trend. Similarly, harder powder becomes more difficult to compact, as indicated by the increasing yield strength. The increase in FHWM shows a consistent structural refinement as a function of the milling time.

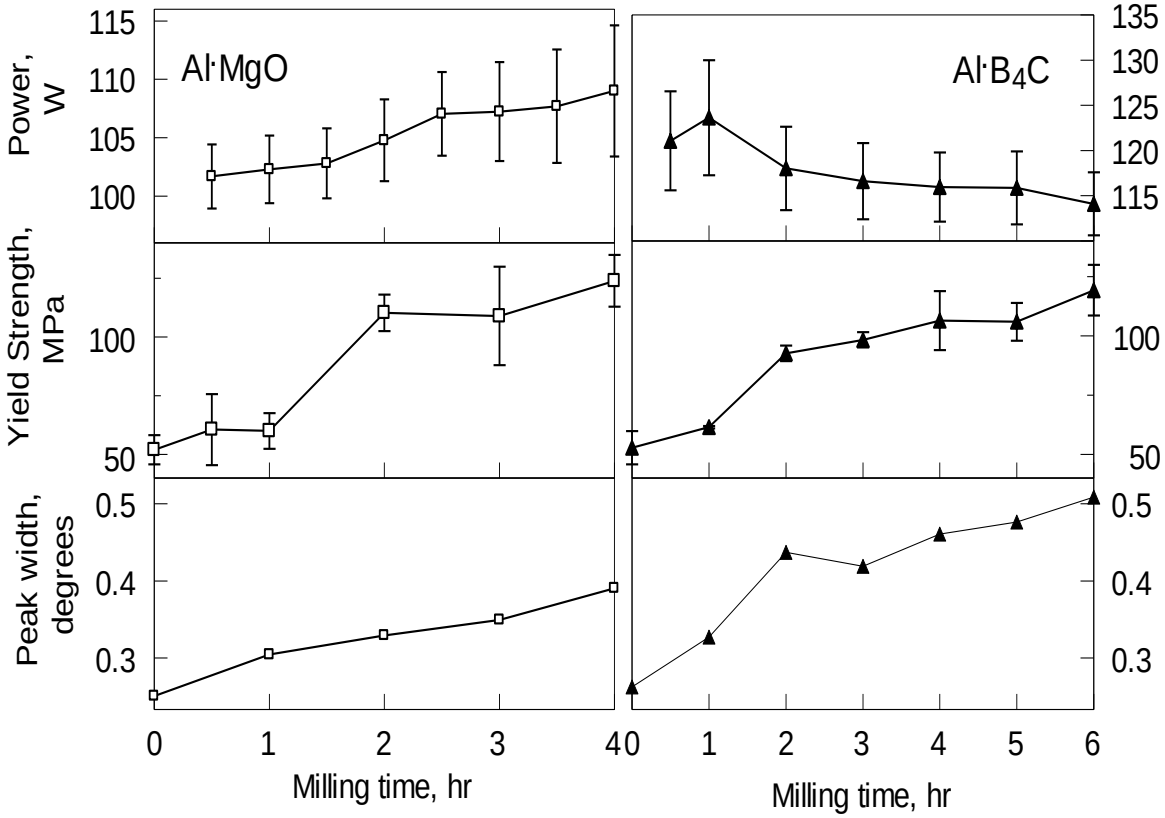

Figure 3.10 Changes in power measured in real time during ball milling compared to changes in parameters of the powder samples (yield strength and FWHM) recovered at different milling times for Al·MgO and Al·B_4C composites.

It is interesting that in Figure 3.10, only changes in yield strength reflect the effect of flake formation at short milling times. From Figure 3.9 it is apparent that changes in the standard deviation of rpm reflect this effect as well. Although not shown in separate plots, changes in standard deviations for torque and power also correlate with the observed flake formation. Thus, both changes in standard deviations of the milling parameters measured in real time and change in the yield strength are useful in tracking the flake formation for this material.

For Al·B_4C composite, the power is observed to decrease as a function of the milling time. This may be attributed to the presence of very hard, fine B_4C particles which behave as an abrasive and create significant friction at earlier times during milling. At longer milling times, when these particles are more and more embedded into Al matrix, their direct interactions with the milling tools are diminished. Apparently, this effect is stronger than that caused by work hardening of the produced Al-matrix composite particles. The yield strength for this powder is also affected by changing mechanical properties of the composite particles as well as by the changes in the particle shapes. At early milling times, when flakes are formed, the yield strength increase is small because of the ease with which the flakes are deforming.

Effect of flake formation on the measured process parameters may be tracked to the increase in power (and torque, Figures.3.9, 3.10) at the short milling times. Embedding abrasive B_4C particles in Al flakes may have caused this effect. For MgO, the flake formation occurred simultaneously with fragmentation of the original MgO particles (not observed in any partially milled samples), while B_4C particles retained their shapes and sizes until much later in the milling process.

The effect of abrasive B_4C particles is less noticeable in the slow compaction, so that the changes in yield strength are dominated by properties of readily deformed Al flakes, similar to Al·MgO.

As soon as the composite particles are produced, the yield strength increases. Its further changes are similar to that of Al·MgO composite, i.e., due to the formation of work hardened aluminum with tiny embedded boron carbide particles as observed in SEM images. However, the measured in real time power and torque decrease; as mentioned above, likely because of the reduced number of abrasive B_4C particles interacting directly with the milling tools.

A consistent increase in the FHWM shows continuous structural refinement of the Al-based composite material. The rate of this refinement appears to be higher when unattached B_4C particles are present (shorter milling times). The rate is reduced once most of the B_4C particles are embedded; however, the structural refinement continued during the entire experiment.

Changes in the motor power measured in real time (and other real time indicators) as well as changes in XRD pattern as reflected by FHWM and the yield strength and were found to correlate with the structural refinement in this material.

3.6 Conclusions

Changes in structural and mechanical characteristics of metal-matrix composite materials prepared by mechanical milling and recovered at different milling times are compared to changes in the parameters characterizing milling process in real time. For the material with components softer than the milling media, increases in yield strength and in the

structural refinement directly correlated with increases in the motor power, torque, as well as with increase in the amplitudes of rapid oscillations of the milling process parameters. Without inspecting the partially milled powders, formation of flakes at early milling times can only be unambiguously correlated with changes in the amplitudes of rapid oscillations of the milling process parameters, but not with time-averaged values of these parameters. For the material with a starting component harder than the milling media, the abrasive action of the harder starting particles (becoming less significant at longer milling times) affected the motor power and torque stronger than the hardening of the prepared composite. Changes in the milling process parameters measured in real time were found useful in tracking the milling progress, although the reduction in the power and torque (as opposed to their increase) correlated with the material refinement. Formation of flakes at early milling times could be correlated with changes in both time-averaged values of power and torque as well as with changes in amplitudes of rapid oscillations of the measured milling process parameters.

CHAPTER 4

DISCRETE ELEMENT MODEL FOR AN ATTRITOR MILL WITH IMPELLER RESPONDING TO INTERACTIONS WITH MILLING BALLS

4.1 Introduction

Ball milling is a versatile and scalable technique for processing and preparation of a wide range of materials, including advanced mechanically alloyed powders [5, 70], powder-like components of energetic materials [49, 71, 72], materials for energy storage [73-75], structural applications in aircraft, automotive and military industries [69], etc. The range of potential applications for mechanical milling as a materials processing technology is rapidly expanding, including preparation of solid dosage forms in pharmaceutical industry [76], battery components [77, 78], materials for food processing [79], artificial bone compositions [16], and remediation of contaminated soil [80]. Despite discovery of many advanced materials that could be prepared by milling, practical and commercial manufacture of such materials poses significant challenges. In particular, it is difficult to predict which milling conditions should be used in a practically scaled milling device to reproduce an advanced material prepared in laboratory experiments. Such predictions should rely on a validated theoretical description of material refinement, suitable to describe milling devices of different types and scales.

Discrete Element Modeling (DEM) is well suited and has been used extensively to describe operation of various ball mills, e.g. [39, 40, 50, 81-84]. However, direct comparisons between the DEM-predicted characteristics of the ball-milling process and experimental results are not straightforward. One common denominator for both experimental and computational data is the energy transferred from milling tools to the powder being milled. Respectively, an energy-based parameter, milling dose, was introduced as a useful concept in our previous work [35, 36, 60]. The milling dose, D_m, is defined as the energy transferred from milling tools to the powder, normalized by the powder mass, m_p:

$$D_m = E_d \cdot t / m_p \tag{4.1}$$

where E_d is the rate of energy dissipation from milling tools and t is the milling duration. It was suggested that the same material could be prepared in different milling devices if the same starting powders were used and if the same milling dose was transferred to the material from milling tools. The successful application of this approach depends on how accurately the milling dose is predicted by DEM descriptions for different milling devices. For example, if a material of interest is prepared in a small scale shaker mill, the D_m value can be obtained using the experimental milling time, t_{exp}, and a DEM model quantifying the energy dissipation rate by milling balls in the shaker mill, E_d. This milling

dose can now be used to predict the milling time required to prepare the same material in a different mill, using DEM to appropriately calculate the respective energy dissipation rate.

The concept of milling dose was explored comparing material preparation in a shaker, planetary, and attritor mills [60]. The first two mills are common in laboratory experiments; the attritor is more suited for commercial scale manufacture. Theoretical models of the milling devices were set-up to obtain the respective E_d terms. In experiments, the same material was prepared using the same starting powders in each mill. Respective milling times, t, and mass loads, m_p, were recorded. The milling dose values for the shaker and planetary mills were close to each other, as expected. However, the computed energy dissipation rate for the attritor was very high, resulting in a much greater than expected milling dose. It was noted that in the attritor mill computation, balls were often predicted to jam, resulting in unrealistically strong forces exerted onto the milling media from the impeller moving at a constant, pre-set speed. These predicted high-force interaction events result in a substantially over-predicted rate of energy dissipation, making the respective DEM description inadequate.

In experiments, ball jams can also occur; however, they cause small changes in the impeller speed. Thus, the variations in the force are attenuated. Santhanam and Dreizin [60] proposed a screening scheme to account for the computationally predicted events associated with unrealistically high forces, in which any events involving

unrealistically high forces were discarded. The resulting, corrected milling dose for the attritor was much closer to that predicted for other milling devices.

Although that approach was effective to obtain the desired outcome, a DEM description that represents the actual operation more directly, without superficial screening, is desired and developed here. The model enables instantaneous changes in the rotation speed of the impeller responding to instantaneous changes in the resistance caused by the milling balls. Recent results on experimental monitoring of rotation rate and torque in the attritor mill [60] as well as additional experiments are used to tune the developed model. The predictions of the developed model are discussed in terms of both accuracy of the assessed energy dissipation and its use for evaluation of the milling dose.

4.2 Materials and Methods

4.2.1 Experimental

Detailed descriptions of the milling conditions, materials and characterization techniques can be found elsewhere [60], and they are only briefly outlined here. An oxide dispersion strengthened aluminum-magnesium oxide (Al·MgO) composite was prepared in three different mills, including an attritor, shaker and planetary, in order to assess and compare the milling dose required to prepare the same material in different devices [60]. The same starting materials, pure aluminum (-325 mesh, 99.9% pure, by Atlantic Equipment Engineers) and magnesium oxide (-325 mesh, 99% pure, by Aldrich Chemical Company,

Inc.) blended at 70%/30% Al/MgO volume ratio were used. The same 9.5-mm diameter hardened steel milling balls were used in all three mills.

In each mill, the milling balls became coated with the powder and thickness of the formed coating was assessed experimentally. First, mass of uncoated balls was recorded, and then the balls coated with the powder were recovered after selected milling times and weighed. The results of these measurements are shown in Table 4.1 in terms of the average weight of the powder coating on one milling ball and its standard deviation from measurements taken at different milling times. The mass shown in Table 4.1 is affected by both pre-set ball to powder mass ratio and dynamics of ball motion in each mill.

Table 4.1 Average Mass of Powder Coating Per Milling Ball for Different Mills

Milling Device	**Ball to Powder Mass Ratio**	**Mass of Powder Coating per Milling Ball, g**
Shaker Mill	10	0.010±0.009
Planetary Mill	3	0.019±0.011
Attritor Mill	36	0.007±0.005

Yield strength of consolidated powders served as an indicator of the milling progress and was measured as a function of milling time for the powders prepared in each mill. The present model focuses on experiments using an attritor mill, model 01HD by Union Process. In this mill, milling balls are agitated by a steel impeller rotating at a designated speed. In the experiments, the impeller was set to rotate at 400 rpm. The attritor mill contains a built-in data acquisition unit by Baldor. It was used to measure the

torque and rotation speed as a function of milling time [60]. The mechanical power required to turn the impeller was calculated from the product of torque and the rotation speed. The data were collected at different milling times; each collected data set was recorded for 1 s with a time resolution of 1 ms.

In order to explore the effect of powder properties on the energy dissipation rate, in addition to experiments with Al·MgO composites, experiments were also performed with a powder blend of Al and B_4C (70/30 % by volume) and with sand. In experiments [60], the attritor vial filled with the steel milling balls contained 1.8 kg of balls and 50 g of powder. Additional experiments were performed, in which the torque and rotation rate were measured for reduced loads. Specifically, balls were loaded with their masses representing one half (0.9 kg), one third (0.6 kg) and a quarter (0.45 kg) loads. No powder was added for these additional experiments.

Friction coefficients necessary for DEM calculations were obtained experimentally as described previously [60] for the 'full load' for different materials. For the cases when no powder was used, the tabulated friction coefficients for the plain steel ball rolling on steel vial surface were used. The values of the friction coefficients characterizing different materials are shown in Table 4.2.

Table 4.2 Friction Coefficients Characterizing Different Milling Configurations

Material System	**Static Friction Coefficient**	**Rolling Friction Coefficient**
Steel (no powder)	0.25	0.01
Al·MgO	0.30	0.05
Al·B_4C	0.34	0.07
Sand	0.60	0.09

Torque and rotation rate measured in real time for partially loaded vials and for the fully loaded vials with the Al·MgO blend are shown in Figure 4.1. The torque is increasing with the increased vial load. The change is most substantial when the load increases from ½ to full load. In addition, oscillations in the recorded torque become stronger as the load is increasing. Similarly, stronger oscillations are observed for the rotation rate at increased loads. The average rotation rate remains unaffected for $^1/_4$, $^1/_3$, and $^1/_2$ loads; however, it decreases slightly when the full load is achieved.

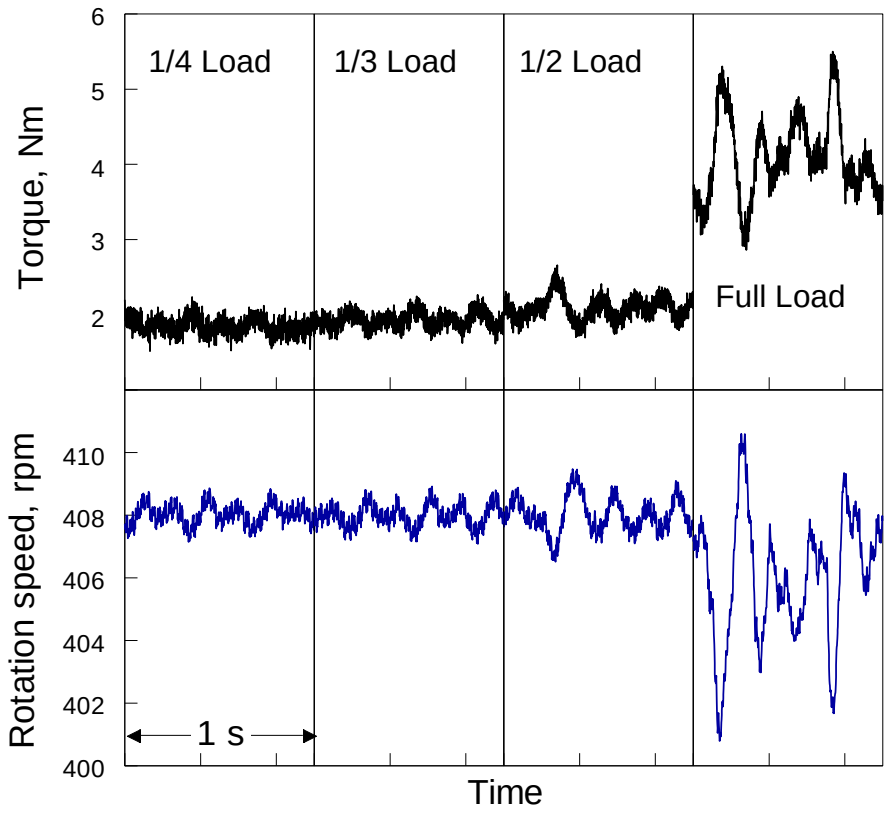

Figure 4.1 Torque and rotation rate measured in experiments with different vial loads.

4.2.2 Model

EDEM, a commercially available DEM code by DEM Solutions was used to describe the attritor mill in this work. The model parameters are briefly mentioned here and detailed descriptions can be found elsewhere [60]. Hertz-Mindlin (no-slip) contact model was used to describe particle-vial, particle-impeller and particle-particle interactions. The time step for simulations was 1 μs and data were recorded every 100 μs. Material properties corresponded to the actual materials used. The static and rolling friction coefficients for the milling balls coated with the powder being processed were determined using additional experiments [60], see Table 4.2. EDEM, as well as other DEM codes, solve equations of motions for particles, i.e., milling balls in this simulation. The motion of

“geometry elements”, i.e., milling vial and impeller, is pre-defined by the setup and is not adjustable in response to interactions between “particles” and “geometry elements.” The issue of defining a DEM approach to describe response of a rigid body upon its interaction with particles has been discussed in the literature [85, 86] However, this issue has not been addressed for the present attritor mill configuration.

Short of modifying the entire DEM code, in this work, the attritor’s impeller was modeled as a large, complex shape particle, or cluster of particles as shown in Figure 4.2. The impeller is constructed using 12.72 mm spherical particles spaced within 2 mm to one another, so that a nearly smooth surface is achieved. The length of the impeller is 140 mm. There are four side-arms, each is 64-mm long. A total of 216 fused particles are used to construct the impeller. Once the particles are positioned together to create the desired shape, contact forces are not generated between these individual particles. This technique of ‘fusing’ spherical particles together to create particles of complex shapes has also been reported elsewhere [87-90]. The impeller is inserted into the vial through an opening in the vial’s lid. The diameter of the opening is 16.7 mm. Since the impeller’s diameter is smaller than that of the opening (as is the case for the actual mill), the impeller can tilt and move horizontally.

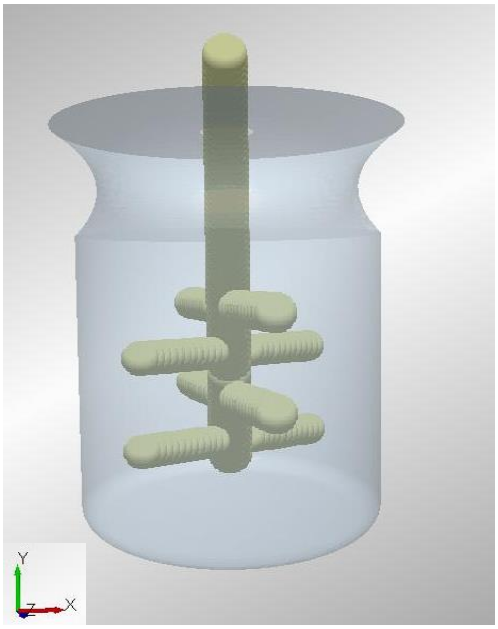

Figure 4.2 Model description of the vial with impeller.

In the actual mill, the impeller is mounted in a motor transmission system, so its effective inertial response to interactions with the milling balls is affected by the way it is mounted. To imitate the impeller's inertial response in the code, its mass was varied systematically. Figure 4.3 shows schematically three impeller designs considered.

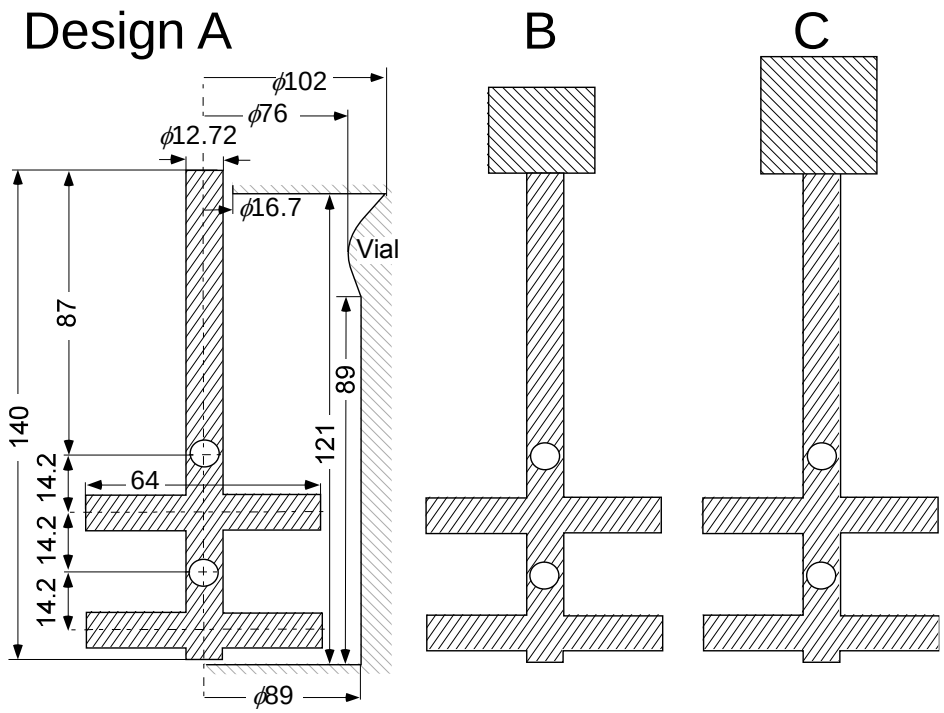

Figure 4.3 Schematic diagrams of impellers with different masses. A, B, C are respectively the impellers with its actual mass, double, and triple mass.

In case A, the impeller in the code simply reproduces the dimensions of the actual impeller. In case B, a metal cylinder is added at the top of the impeller. This added cylinder's dimensions are selected so that the mass of impeller B is twice that of impeller A. Similarly, in design C, the added cylinder results in the overall mass to be triple that of A. The cylinders added on to the impellers B and C also comprise of fused spherical particles.

The impeller was moved by an applied torque. The torque was varied depending on the rotation speed, the variation was determined based on experimental data. It was observed that in experiments, instantaneous values of torque and rotation speed change in

the opposite phase [60], see also Figure 4.1. The data collected previously [60] was re-processed to establish an overall correlation between the measured torque and rotation speed, as shown in Figure 4.4. A linear fit for the observed experimental trend is also shown. This fit was used in the code to describe the impeller motion.

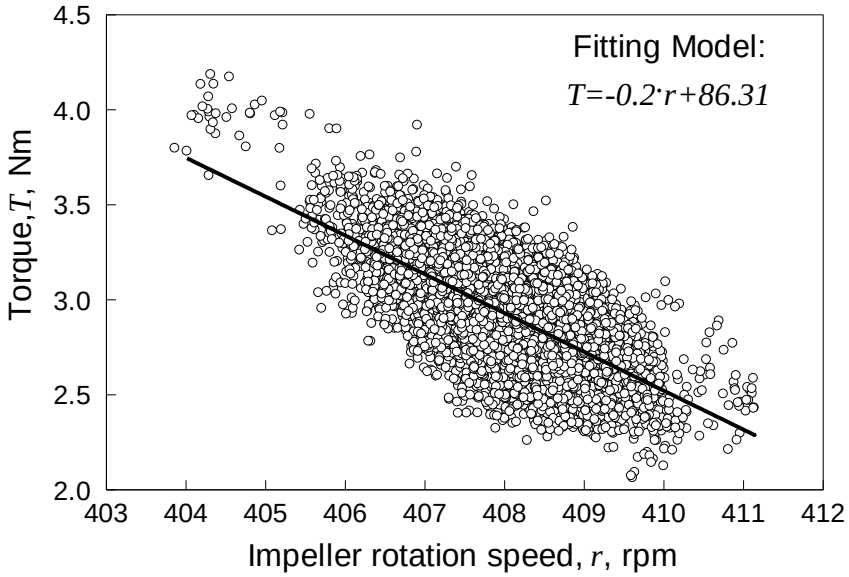

Figure 4.4 Relationship between torque and rotation speed of impeller as obtained from real-time measurements.

Data shown in Figure 4.4 also indicate the range of practically observed changes in the rotation speed and torque during the mill operation. In preliminary calculations, it was observed that the impeller can still be jammed, causing much greater instantaneous changes in its rotation rate compared to data in Figures 4.1 and 4.4. To avoid this situation, the impeller's motion was finally described as follows:

$$\begin{cases} \omega < 403\,rpm; & T = 100\,[Nm] \\ \omega \geq 403\,rpm; & T = -0.2 \cdot \omega + 86.3\,[Nm] \end{cases} \tag{4.2}$$

Where ω is the impeller rotation speed and T is the torque.

An increase in the torque for the rotation rate below the observed range (ca. 403 rpm) describes the response of the transmission system that maintains the rotation rate in the mill. The value of 100 Nm is selected after testing higher and lower torque values and observing the resulting predicted range of rotation rates. For lower torque values, the return of the rotation rate to the pre-set range occurred slowly; higher values of torque resulted in instantaneous acceleration of rotation rate above the experimental range.

4.3 Results

The overall range of rotation rates and torque values produced by the DEM description correlated well with the experimentally observed ranges, as illustrated in Figure 4.5. For this preliminary comparison, the calculations represent impeller described by design A in Figure 4.3. The data are presented for a 1-s interval. The experimental data were acquired with a time resolution of 1 ms. In the calculation, the data were saved every 0.1 ms; then the average of 10 points was used to reduce the time resolution to 1 ms to be directly comparable with experiments.

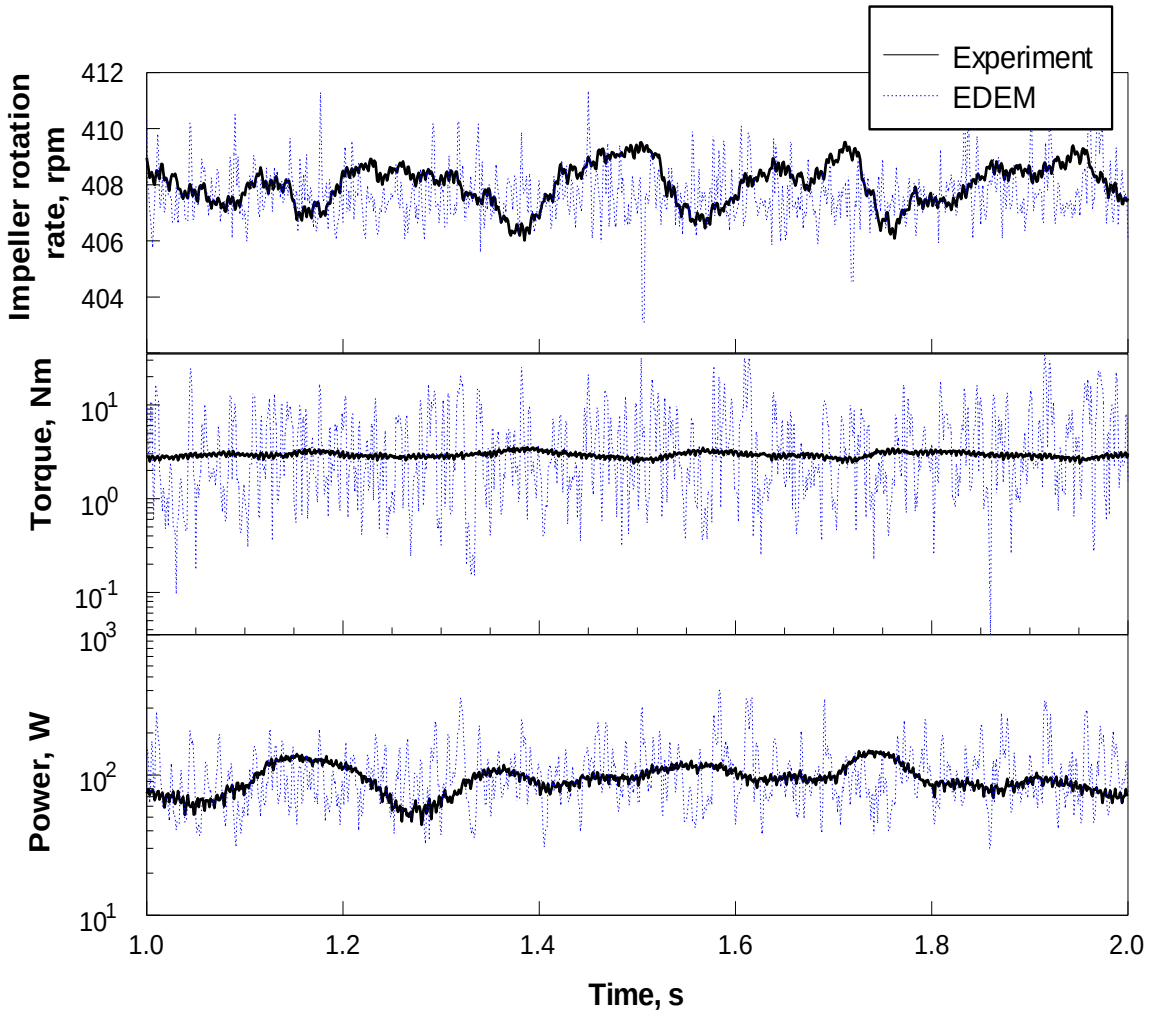

Figure 4.5 Calculated and experimental instantaneous values of rotation rate, torque, and power. Impeller design A (Figure 4.3) was used in calculations.

The experimental trace (similar to that shown in Figure 4.1) appears to exhibit oscillations with both high and low frequencies. The period of the low frequency oscillation is close to the time of one full rotation for the impeller. It is difficult to interpret the high-frequency oscillation because it is only weakly depending on the load of the milling vial. In other words, the high frequency pattern is observed even for the

empty ball mill. The DEM prediction shows only a relatively high frequency oscillation pattern.

The power dissipated by the milling tools was also compared for experimental data and predictions. For experiments, the mechanical power was calculated as a product of the torque and impeller rotation speed. In the model, power was obtained directly as the sum of energies dissipated in individual collision events per second. In both cases, the power characterizes the rate of energy transfer from milling tools to the powder.

The comparison between the experimental and calculated power values is shown in Figure 4.5. The instantaneous changes in both values are significant; however, the changes occur in the same range, suggesting that the calculations are generally consistent with the experiments.

The average and standard deviation data for power as obtained from experiments and DEM models A, B, and C are shown in Figure 4.6. The variation in experimental load was described previously. A power increasing with the load was observed in experiments and was well reproduced in the model. The influence of both load and impeller design on both the predicted power and the range, in which it varies, is observed. The average values of power are shown in the top plots and standard deviations are in the bottom. The best match of experimental and computed data is observed when double impeller mass (design B) is used in the DEM model. It is interesting that the match improves simultaneously for both the average power value and for its standard deviation.

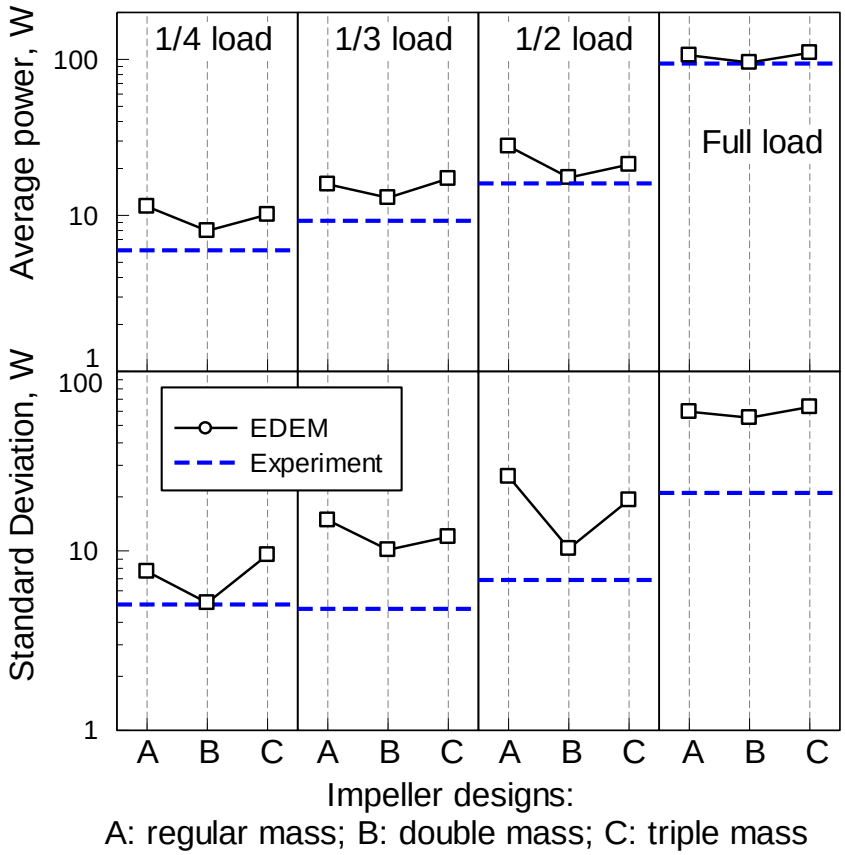

Figure 4.6 Results of parametric investigation: average power and its standard deviation at different vial loads for model and experiment. The model results are shown for three impeller designs A, B and C.

The range of power variation (expressed through standard deviation in Figure 4.6) is systematically greater for the model compared to experiments. The difference appears to increase at higher loads. It is likely that this discrepancy of calculations and measurements is caused by the finite time resolution of the experimental data acquisition system, compared to the instantaneous capture of the torque and rotation rate values in the DEM output.

To understand why design B exhibits the best match with experimental data in Figure 4.6, the impeller's motion for each design was examined further. Locations of the bottom tip of the impeller as a function of horizontal coordinates, *X* and *Y* are shown in Figure 4.7. Each data point represents a position of the impeller's tip at an individual time step during the simulation. The data are shown for a simulated time of 1 s.

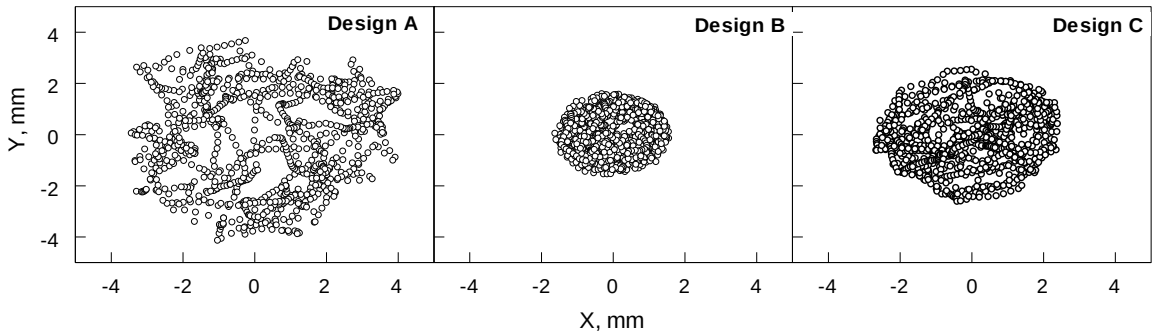

Figure 4.7 Horizontal coordinates of the bottom tip of the impeller for designs A, B, and C.

It was observed that the impeller by design B is generally more confined in space compared to both designs A and C. It can be qualitatively explained as follows. When a lighter impeller (design A) is used, its position is strongly affected by the interactions with milling media and it is displaced from its central location easily. On the other hand, in a much heavier design C, the impeller's inertia is high. Thus, once displaced, it takes a long time to return to the central position. Design B appears to result in the most confined and realistic motion pattern, also yielding the best match between experimental and predicted energy dissipation rates.

4.4 Discussion

4.4.1 Predicting Power Dissipation

A direct DEM validation can be obtained if the power dissipated during milling is predicted accurately for preparation of different materials. The effect of material is included in the DEM through adjustment of the directly measured restitution and friction coefficients [60]. Comparisons of the present "responsive" impeller model with the experimental data collected during milling three different materials: Al·MgO and Al·B_4C composites, sand, as well as operation of the mill with milling balls only [60] are shown in Figure 4.8. The friction coefficients shown in Table 4.2 were utilized in the calculations. The model employed impeller design B.

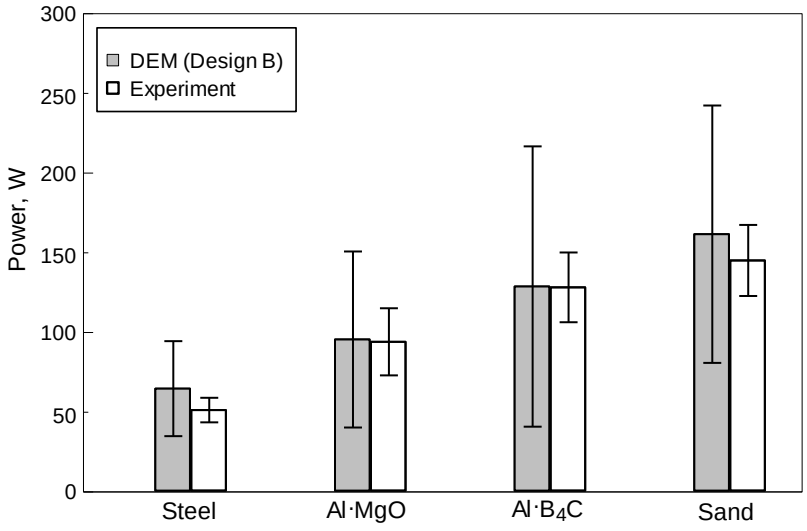

Figure 4.8 Comparison of average and standard deviation in powder from EDEM and experiments.

The match between the predicted and measured power is good for all cases. The error bars show standard deviations from the average value for both calculations and measurements taken for 1 s, which was the time of data acquisition in both experiments and computations. A greater error bar observed for the predicted values of power is, as earlier mentioned, likely associated with a higher time resolution obtained in calculations compared to experiments. Comparisons shown in Figure 4.8 validate the present DEM description of the milling in an attritor and show that the energy dissipation from the milling tools is predicted accurately.

4.4.2 Evaluation of the Milling Dose

Using design B, for which, as shown in Figure 4.8, the energy dissipation in the attritor is accurately predicted, the milling dose was reevaluated for the experimental conditions used previously [60]. The material prepared in those experiments was Al·MgO composite powder; different powders prepared using different milling devices were assumed to be identical if they exhibited the same yield strength. Because the same powders were prepared using different mills, it was anticipated that an accurate model would yield the same milling dose for each of the milling conditions. However, this was not the case for the attritor, as discussed in more detail previously [60].

It was established that ball jams resulted in unrealistically high forces leading to substantially overestimated rate of energy dissipation in the attritor. To identify the issue, individual collision events in the milling vial were sorted based on the average force exerted in these events. The results are shown in Figure 4.9. The data for shaker, planetary and attritor mill presented earlier [60] are shown for reference.

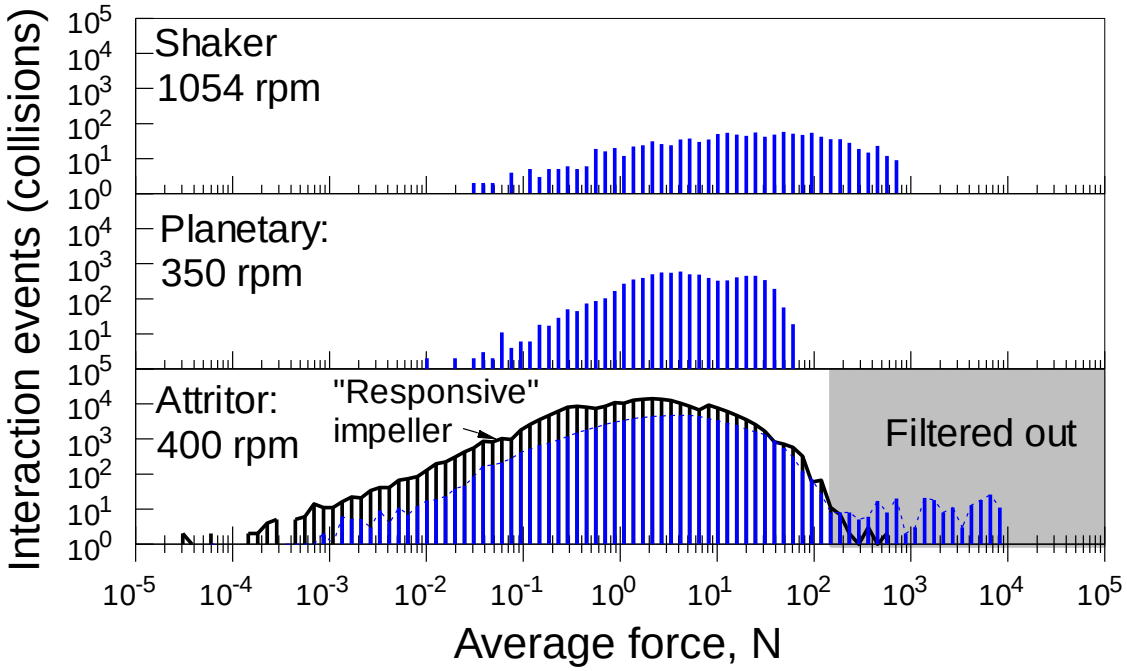

Figure 4.9 Histograms sorting interaction events of milling tools based on the average force for different milling devices.

For the attritor mill, the energy dissipation rate predicted considering the constant rotation rate of the impeller was previously manually filtered to remove the high force events, falling into the shaded region in Figure 4.9. An overlapped histogram shows data from the current "responsive" impeller model. The very high force "tail" for the attritor

mill disappeared, so no superficial data filtering is necessary. On the other hand, more interaction events with lower forces are observed. Estimates suggest that such low-force events do not result in a substantial increase in the overall energy dissipation by the milling tools and are, therefore, unimportant for assessing the milling dose.

The milling dose values calculated for different mills for the experiments [60] are presented in Table 4.3. The calculations for shaker and planetary mills as well as the "unscreened" and "screened" values obtained for the attritor with impeller rotating at a constant rate were reported earlier. The energy dissipation term (obtained from the model) used to determine the milling dose is an average over five consecutive time intervals of 100 ms each. The milling dose for the "responsive" impeller obtained in the present calculations is close to its "screened" value and thus represents the experiments reasonably well, without the superficial screening.

Table 4.3 Comparisons of Milling Dose and Associated Parameters for Three Milling Devices

Parameter	**Shaker mill**	**Planetary mill**	**Attritor mill**		
			Unscreened	Screened	"Responsive" EDEM model
E_d/m_p, W/g	4.6±0.1	2.0±0.04	10.0±1.0	1.7±0.1	1.9±0.2
Experimental milling time, t, hr	0.4±0.1	1.0±0.3	1.8±0.1		
Milling dose, D_m, W·hr/g	1.8±0.5	2.0±0.6	18.0±2.8	3.06±0.3	3.4±0.4

Despite removal of the unrealistically high forces, the milling dose implied by the DEM predictions and experiments [60] for the attritor remains somewhat higher than for the other two mills. In defining the milling dose, the energy dissipation rate predicted by DEM is distributed over the entire powder load, as shown in Equation (4.1). However, it is possible that the mechanical refinement in real time occurs just for the powder coated on the milling balls and the vial surface. This involves only part of the powder, which can be established using data from Table 4.1. Clearly, the coating is being removed and re-applied continuously during milling, so that eventually all the powder gets refined. However, the efficiency of mechanical refinement may depend on how much powder is coated on the milling tools instantaneously. This correction can be significant for the attritor, in which the ball to powder mass ratio is much greater that in the other mills (Table 4.1), so that a greater fraction of powder may be continuously refined. To explore this hypothesis, an alternative milling dose (D_m^*) definition was considered,

$$D_m^* = E_d \cdot t / m_c \tag{4.3}$$

where m_c is the mass of the powder coated on the surface of milling tools (including the surface of the milling vial). The value of m_c was calculated for each case considering mass of coating on an individual ball and assuming that the coating thickness is uniform throughout.

Deriving from previous knowledge of the mill operation in different devices, the surface area of vial geometry used to calculate m_c was different for the three cases. For the planetary mill, the primary material processing is a result of rolling along the surface of the vial and hence, surface area of vial walls was used. In the shaker mill, the collisions on the top and bottom of the vial are important and hence, surface area of the vial wall as well as top and bottom vial surfaces were included. In the attritor mill, the powder processing is independent of the top lid surface and hence, the vial walls and bottom surface were used. The values of D_m^* and D_m for different mills are shown in Figure 4.10.

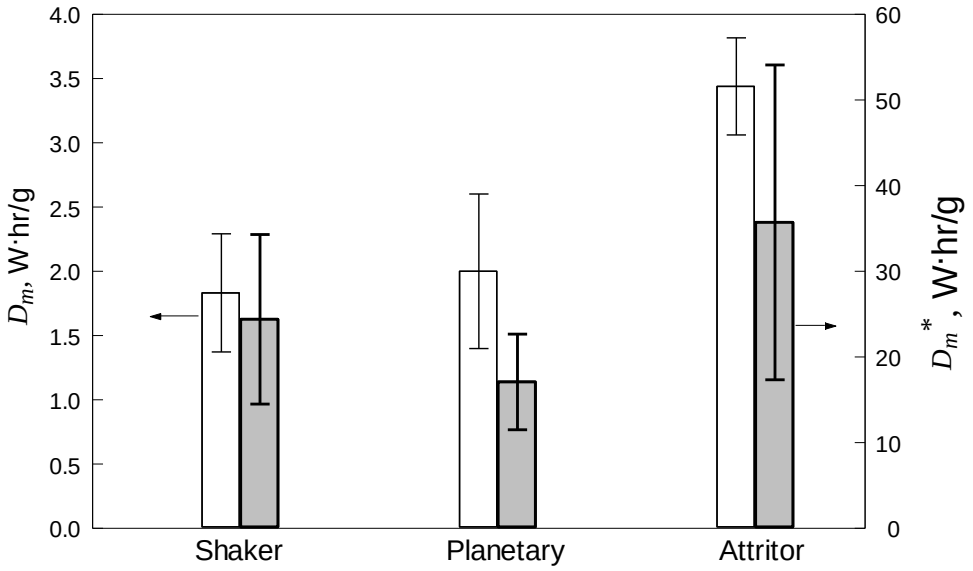

Figure 4.10 Milling dose predicted based on the entire powder load, D_m, and an alternatively defined milling dose D_m^* defined based on the mass of the powder coated onto the milling balls.

The responsive impeller model was considered for the attritor mill. As expected, because of a greater fraction of the powder coated on the milling tools in the attritor, the resulting value of D^* is reduced and becomes closer to those for the other two mills. It is apparent that the match between different mills is improved. Note that the error bar for D_m^* takes into account substantial error in the measured coating thickness shown in Table 4.1.

Milling dose defined by Equation (4.2) does not directly account for the rates of coating removal and re-applying during the milling and thus may need to be refined further. However, the approach taking into account the powder coated onto milling tools may be useful for more accurate predictions of the milling progress in different types of mills.

4.5 Conclusions

The accuracy of DEM representation of material processing in an attritor is significantly improved when interactions of the moving impeller and the milling balls are accounted for by enabling the impeller to instantaneously slow down when the balls jam, and then return to its pre-set rotation rate. It is shown that in the model, the rotation of such "responsive" impeller can be described using an experimentally obtained correlation between instantaneous values of torque and rotation rate. This correlation can be programmed into DEM to describe the torque applied to the impeller for the range of

rotation rates observed experimentally. When the rotation rate falls below the experimental range, the torque needs to be further increased.

It is also shown that the mass or moment of inertia of the responsive impeller is affecting its predicted motion pattern and the energy dissipation rate for the entire system. Parametric analysis established the specific mass for the impeller for the present laboratory scale attritor, for which DEM provides the best correlation with the experimental data. This mass used in DEM accounts best for the way the impeller is mounted and connected to the motor in the actual mill; similar parametric analysis would be necessary to describe responsive impellers in different attritor mills.

The DEM employing responsive impeller is accurately predicting energy dissipation rates for milling different materials when the accurate values of restitution and friction coefficients are included. Such values can be obtained from separate simple experiments for each type of material.

Considering responsive impeller, no superficial filtering for the DEM results are required to predict a reasonable milling dose for the powder prepared in attritor as compared to the same powder prepared in the shaker and planetary mills. The definition of the milling dose may need to be corrected to account for the fraction of the powder coated onto the milling tools, rather than the entire powder charge in the vial.

CHAPTER 5

INTERACTION PARAMETERS FOR DISCRETE ELEMENT MODELING OF POWDER FLOWS

5.1 Introduction

Discrete Element Modeling (DEM) [58] is gaining recognition as a valuable tool elucidating phenomena occurring on the scale of individual particles in powder systems. Current research ranges from modeling of particulate flow in hoppers [91, 92] and mixers [93, 94], describing mills [60, 95, 96], fluidization [97, 98], particle packing studies such as compaction [99, 100], as well as conveying operations [101, 102]. Despite the broad appeal of DEM, a significant caveat exists. In order to describe the experimental phenomena accurately, the model must use the correct particle interaction parameters. For most DEM codes, these parameters include coefficients of restitution and friction for particle-particle and particle-wall interactions.

Both collision and friction phenomena are widely studied for macroscopic bodies, including spherical particles of different dimensions. Coefficients of restitution were reported based on experimental sphere-sphere collision by multiple authors, e.g., Refs. [103], [104], [105], [106], and [107]. The materials studied range from polystyrene, glass, stainless steel to granite balls. However, even the smallest ball size of about 2.5 mm [104] is still much greater than the typical particle size in most powders.

Several studies reported that the restitution coefficient becomes greater for lower impact velocities [103, 107, 108]; conversely, it was also suggested that its dependence on velocity is weak [104, 105, 109]. The effect of impact velocity may be important for powder systems, where relative particle velocities are reduced because of the collective powder flows.

Although designing experiments to directly monitor collisions of micron level particles is difficult, theoretical efforts [110, 111] show that the mechanisms governing energy dissipation in collisions alter for smaller particle sizes. Hence, values of coefficients of restitution determined in experiments with macroscopic bodies may not be describing appropriately collisions of much finer particles.

Defining both rolling and static friction coefficients is required for state of the art DEM codes, such as EDEM [56, 60]. The values for powders are typically obtained from experimental shear cell [112-114] or compaction studies [115, 116], empirical correlations, conventional practice, or tailored in the model to match experimental data. Shear cell and compaction measurements yield generic "wall friction" and "internal friction" values, which are difficult to relate directly to the rolling and static friction coefficients employed in the DEM particle interaction models.

Since friction is defined by the surface roughness, asperities, and defects, that may, for bulk materials, be comparable in size to the dimension of powder particles, the physics governing friction forces for individual powder particles may be changing [117]. No

direct friction measurements for fine particles could be found in the literature, leaving the data implied by the bulk friction coefficients as a reasonable preliminary assessment for the static friction. Also, no data could be found for measured rolling friction coefficient. In several papers [118], [119], [120], empirical correlations were proposed expressing the rolling friction coefficient as a function of the particle diameter. These correlations are summarized in Table 5.1. The proposed reduction in the rolling friction for finer particles might be associated with the respectively reduced size of surface asperities.

Table 5.1 Rolling Friction Empirical Correlations $\mu_{rolling} = X \cdot D_{\max}$

X [1/m]	**Particle Diameter, D_{max} [m]**	**Reference**
0.001	N/A	[118]
0.01	0.0118-0.014	[119]
0.015	0.02	[120]

A set of focused, systematic studies of the effect of particle interaction characteristics on DEM-predicted powder flow was reported by Ketterhagen et. al [92, 121, 122]. Unfortunately, it was concluded in Ref. [121], that similar results could be predicted using various combinations of friction coefficients. It appears that the above conclusion suggests that the experimental data available were inadequate to properly "calibrate" the DEM and thus identify the true particle interaction characteristics.

This work offers an approach for such a calibration combining simple experiments and their DEM representations. There are two essential features in the present approach:

- The experimental system includes a relatively small but statistically significant number of narrowly sized, spherical powder particles (20,000), so it can be completely described by DEM.
- Experiments with the same powder are performed with systematically varied powder flow parameters; each experimental configuration is also represented computationally, which enables simultaneous adjustment of unknown coefficients of friction and restitution.

5.2 Experiments and Materials

5.2.1 Experimental Setup

A vibratory powder feeder with a miniature hopper was designed as illustrated in Figure 5.1. The hopper size was selected to fit approximately 20,000 50-μm diameter spherical particles to enable a description of the entire system by a DEM code. Respective powder mass can vary in the range of 2.6 to 7.9 mg, for powder densities of 2 - 6 g/cm^3. The hopper was built using several inserted miniature brass tubes, as shown in Figure 5.1. The tubes were soldered on the outside.

The hopper's outlet was inserted into a horizontal tube through which an air was flown. Thus, the particles falling out from the hopper were carried away by the air. The entire assembly was rigidly mounted on the diffuser of a loudspeaker. The loudspeaker was powered by an amplified signal from a frequency generator. Powder feed rates were measured at different frequencies: 120, 240, and 500 Hz.

The powder was loaded into the hopper before starting the experiment; however, it did not fall out until the hopper was vibrated. Both the hopper and powder were dried at a reduced pressure of about 0.2 atm and at 75 °C before each experiment. The hopper was typically dried for 2 hours and the powder was dried for at least 48 hours. The hopper assembly was weighed before loading; it was also weighed before and after each experiment. A Mettler Toledo AX 205DR Delta Range balance was used with the mass resolution of 0.01 mg. Therefore, the loaded powder mass and powder mass remaining in the hopper were determined.

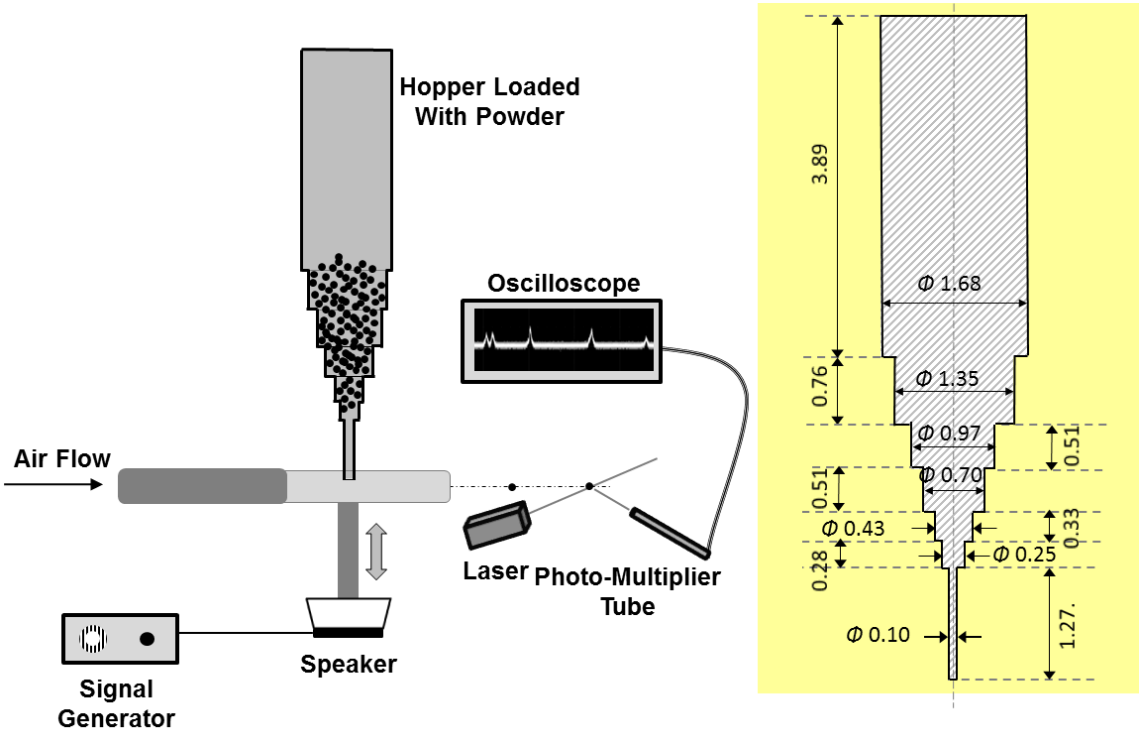

Figure 5.1 Schematic of experimental set-up. In the inset, all dimensions are in mm.

The air jet carrying particles that fell from the hopper was illuminated by a laser sheet. A photomultiplier tube (PMT) equipped with a collimator was positioned to detect the light scattered by the particles passing through the laser sheet. The angle between the incident and scattered light beams was selected to be 120º optimized for Mie scattering [123]. The PMT output was fed to an oscilloscope. Thus, light scattering peaks produced by individual powder particles were recorded.

A typical sequence of recorded light scattering pulses is shown in Figure 5.2. In this example, eight pulses occur during 100 ms, indicating an average feed rate of 80 particles per second.

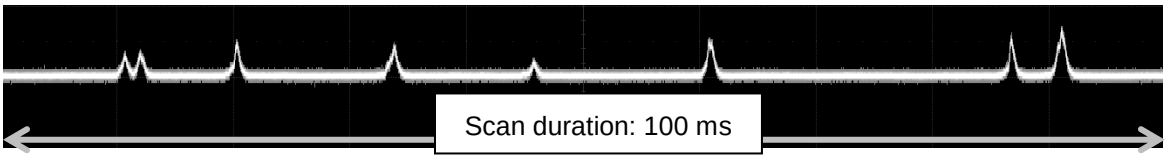

Figure 5.2 Typical PMT measurement

5.2.2 Vibration Characteristics

The amplitude of vibration was measured using photographs of the exit tube, rigidly connected to the hopper. A Casio Elixir EX-FH 25 camera with a custom close-up lens was used to obtain a magnified image of the exit tube against a white background. The images were taken without and with tube vibration using different pre-set frequencies. The exposure time was always selected to exceed the period of vibrations. An image of

motionless tube was then overlapped with that of a vibrating tube, using ImageJ processing software, as illustrated in Figure 5.3.

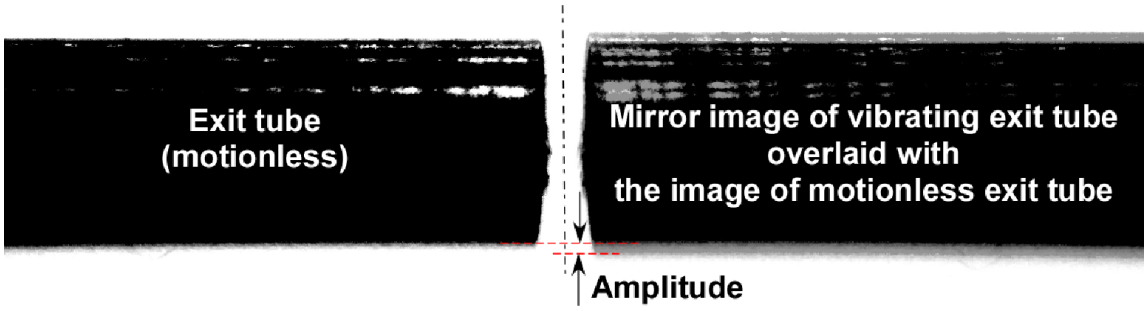

Figure 5.3 A photograph of a motionless exit tube (left) and a mirror image of the overlaid images of the vibrating and motionless tube (right). The gray band shows the displacement of the tube edge used to estimate the amplitudes for modeling studies.

The difference between the edge positions in the overlapped images shows the maximum amplitude of vibration. Positions of the bottom edge of the tube, where the focus was better, were monitored and used to estimate the amplitudes. Five consecutive images were taken for the duration of 1 s while the hopper was vibrating. Each image was used to obtain a data point. It was observed that although most amplitude measurements performed at each frequency setting were consistent to one another, there were outliers for some cases, typically showing lower amplitude. The average values from the consistent data points were calculated and entered as the amplitude in the model. Table 5.2 presents the average measured amplitude values which were used in EDEM for the three frequencies.

Table 5.2 Vibration Amplitudes for Different Frequencies Obtained from the Image Processing

Frequency, Hz	Amplitude, mm
120	0.31
240	0.16
500	0.10

Although outliers were ignored for the purpose of calculating the average amplitude, they could have been indicative of a modulated output from the speaker. To test this, sound waves were recorded using a microphone and visualized using Matlab as shown in Figure 5.4.

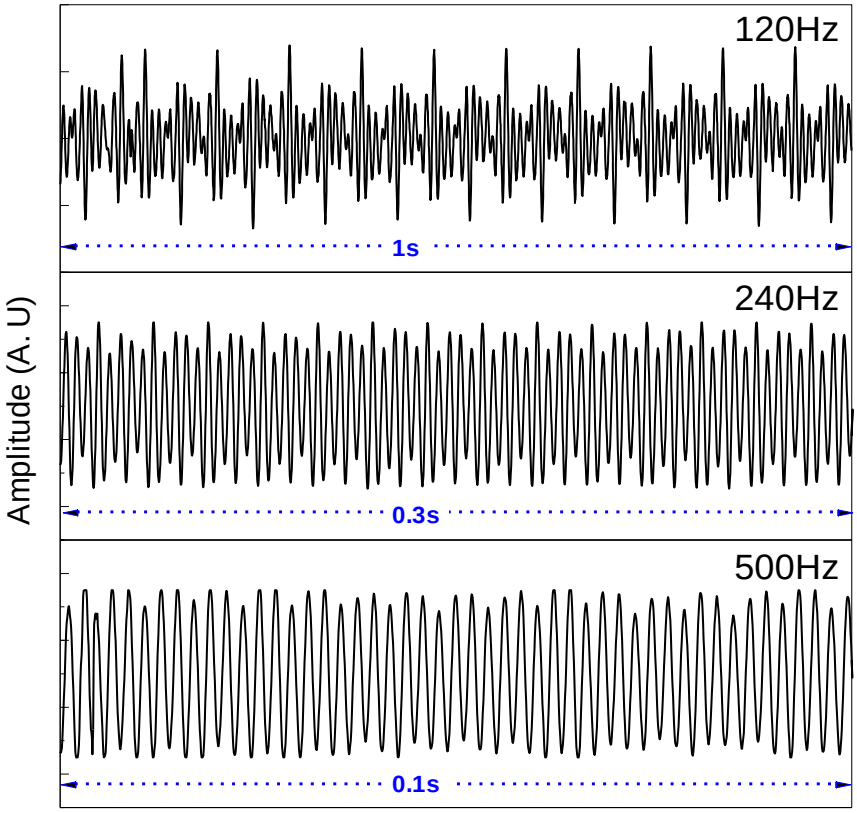

Figure 5.4 Sound waves recorded at different frequencies.

Fourier transforms were obtained for each of the recorded waves, showing that each signal contains four basic waves. Two of these basic waves were comparably strong; while two others were rather weak. The frequencies and amplitudes of the two stronger waves were recorded.

To model the modulated signal, two waves were superimposed over each other in DEM. The strongest wave represented the pre-set frequency with its initial amplitude, as shown in Table 5.2. The amplitude and frequency for the second wave were calculated considering the ratios between amplitudes and frequencies of the two strongest basic waves obtained in the Fourier transform for each recorded sound signal. A comparison of the experimental and modulated two-wave oscillation used in DEM is shown in Figure 5.5 for a nominal 120 Hz case. It appears that the pattern used in the DEM follows closely the experimental vibration pattern.

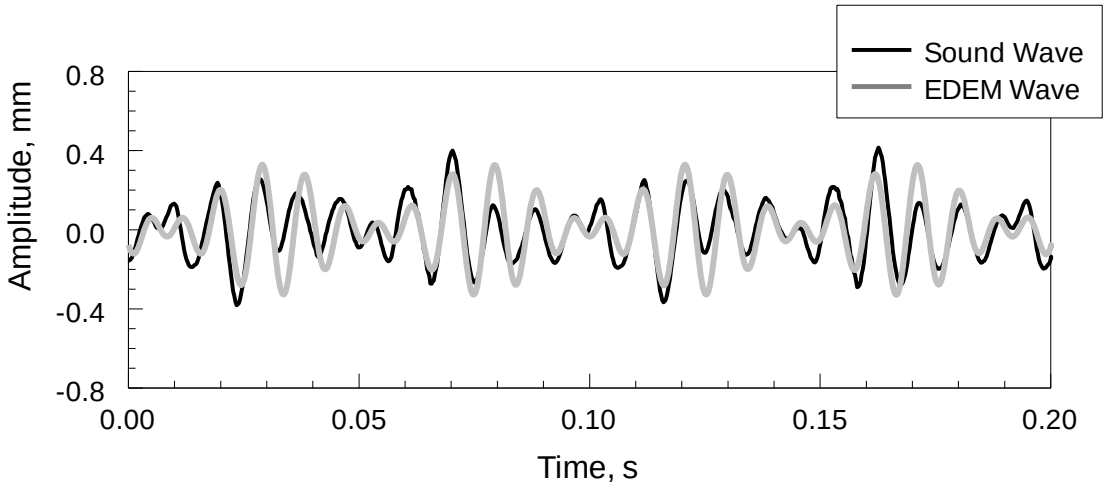

Figure 5.5 Sample wave match for EDEM based on experimental measurement (120Hz).

Results obtained with both single mode sinusoidal oscillations with pre-set frequencies and modulated waves including two stronger basic waves are presented and discussed.

5.2.3 Materials

The material used in this study was yttrium stabilized zirconia beads (Tosoh USA, Inc.) with the nominal size of 50 μm. A scanning electron microscopy (SEM) image of the beads is shown in Figure 5.6. Multiple SEM images were taken and diameters of zirconia spheres were measured.

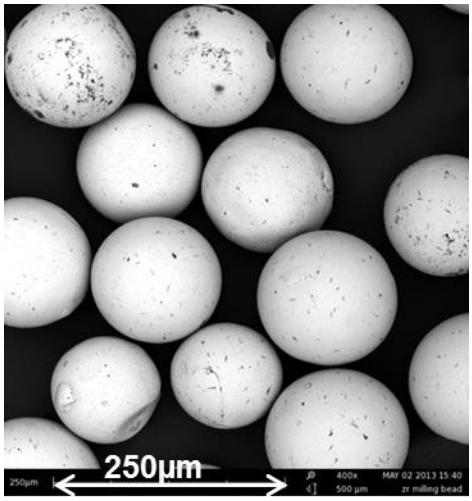

Figure 5.6 SEM image of Zirconia beads.

In total, 323 particles were processed and the obtained relatively narrow particle size distribution is shown in Figure 5.7. This distribution was used in DEM in addition to the cases describing a monodisperse, 50-μm powder.

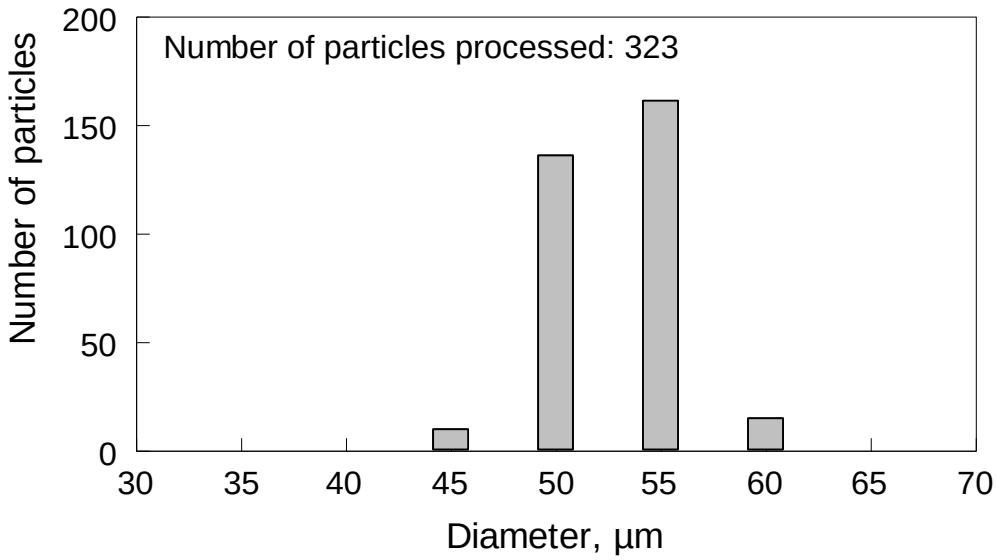

Figure 5.7 Size distribution of Zirconia beads (from SEM image processing).

5.3 Model

Commercially available DEM software, EDEM (DEM Solutions Inc.) was utilized in this research [56]. The Hertz-Mindlin (no slip) soft particle contact model was used for the force calculations. This model combines Hertz's elastic theory for the normal contacts and Mindlin's solution for the tangential contacts [58]. Further details can be found in Ref. [60].

The hopper geometry (brass) and the particles (zirconia) were described by EDEM. The properties of the brass and zirconia were obtained from literature [124]. The properties required in the model include density, shear modulus and Poisson's ratio. Both mono-disperse particles (with the diameter of 50 μm) and the particle size distribution shown in Figure 5.7 were considered.

The calculations were aimed to establish the values of coefficients of restitution and friction, for which predicted and experimental powder feed rates match each other at different hopper vibration frequencies. As a starting point, the values of restitution coefficient and friction coefficients for the particle-wall interactions were taken from an earlier work [125]. The initial values of friction coefficients for particle-particle interactions were evaluated using larger zirconia spheres and following an experimental method outlined in Ref. [60]. The starting values of coefficients are shown in Table 5.3.

Table 5.3 Initial Values of Restitution and Friction Coefficients Used in EDEM

Interaction	**Friction Coefficient**		**Restitution Coefficient**
	Static	**Rolling**	
Particle-Particle [60]	0.7	0.03	0.5
Particle-Wall [125]	0.3	0.1	0.5

5.4 Results

5.4.1 Experimental Results

At least six experiments were performed for each pre-set vibration frequency. Measured feed rates are shown in Figure 5.8. A hashed bar shows the experimental number of particles per second obtained using the measured mass change of the hopper before and after the test divided by the time the powder was being fed. For this estimate, it was assumed that particles were mono-sized, with 50 μm diameter and density of 5.68 g/cm^3, corresponding to zirconia. A solid bar shows feed rates obtained using direct

peak counts from the recorded oscilloscope traces. Each peak corresponded to one particle. The feed rates are based on counting 300 – 500 pulses for each pre-set vibration frequency. The two measurements are in good agreement with each other.

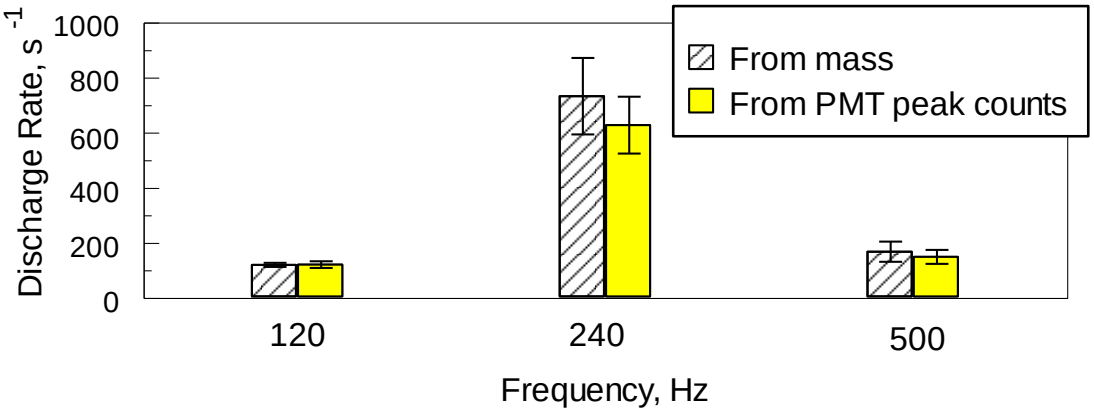

Figure 5.8 Comparison of discharge rates estimated from the hopper mass change vs. that inferred by the counted PMT peaks.

At 120 Hz, the particles were fed at a consistently low rate. At 240 Hz, the feed rate increased markedly. At 500 Hz, the feed rate was reduced. In the latter case, it was noted that the powder always jammed after a period of time. Once a jam occurred, the powder flow could not be resumed, even if the oscillatory pattern was disrupted by varying the signal frequency and amplitude. The maximum duration of an individual experiment was 3.2 min; however, if a jam occurred, the feed rates shown in Figure 5.8 were calculated accounting only for the time before the jam, typically less than 2 min.

The average percentages of the powder removed from the hopper in individual experiments determined from the hopper weighing before and after tests are shown in Figure 5.9. More than 90% of the particles were removed from the hopper at 120 Hz. The amount of powder removed at 240 Hz is also close to 90 %. At 500 Hz, only about 50% of the powder was removed from the hopper before it jammed.

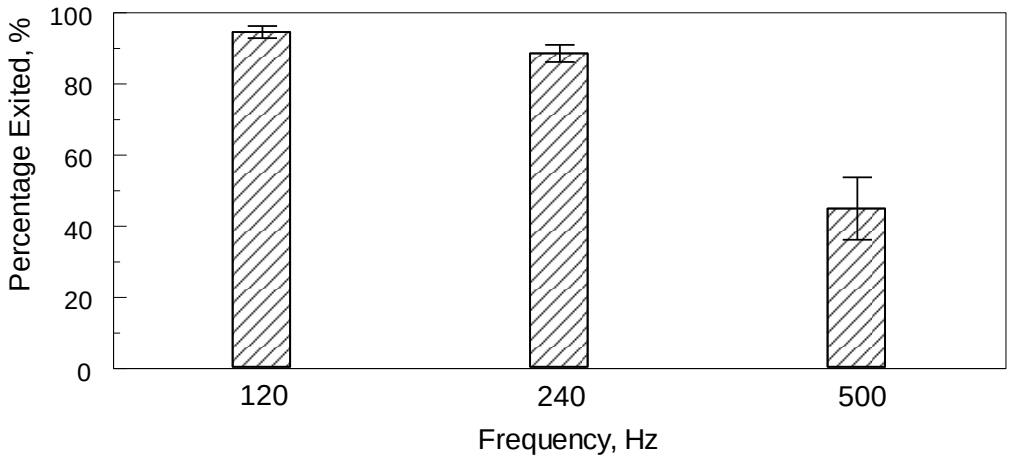

Figure 5.9 Percentage of powder removed from the hopper in vibration runs using different frequencies.

5.4.2 Predicted Powder Motion Patterns

Results of preliminary calculations using friction and restitution coefficients given in Table 5.3 are illustrated in Figure 5.10. Each simulation described 0.1 s of real time and considered 20,000 of 50-μm diameter zirconia particles. For each frequency, five images are selected showing different instants of the simulation.

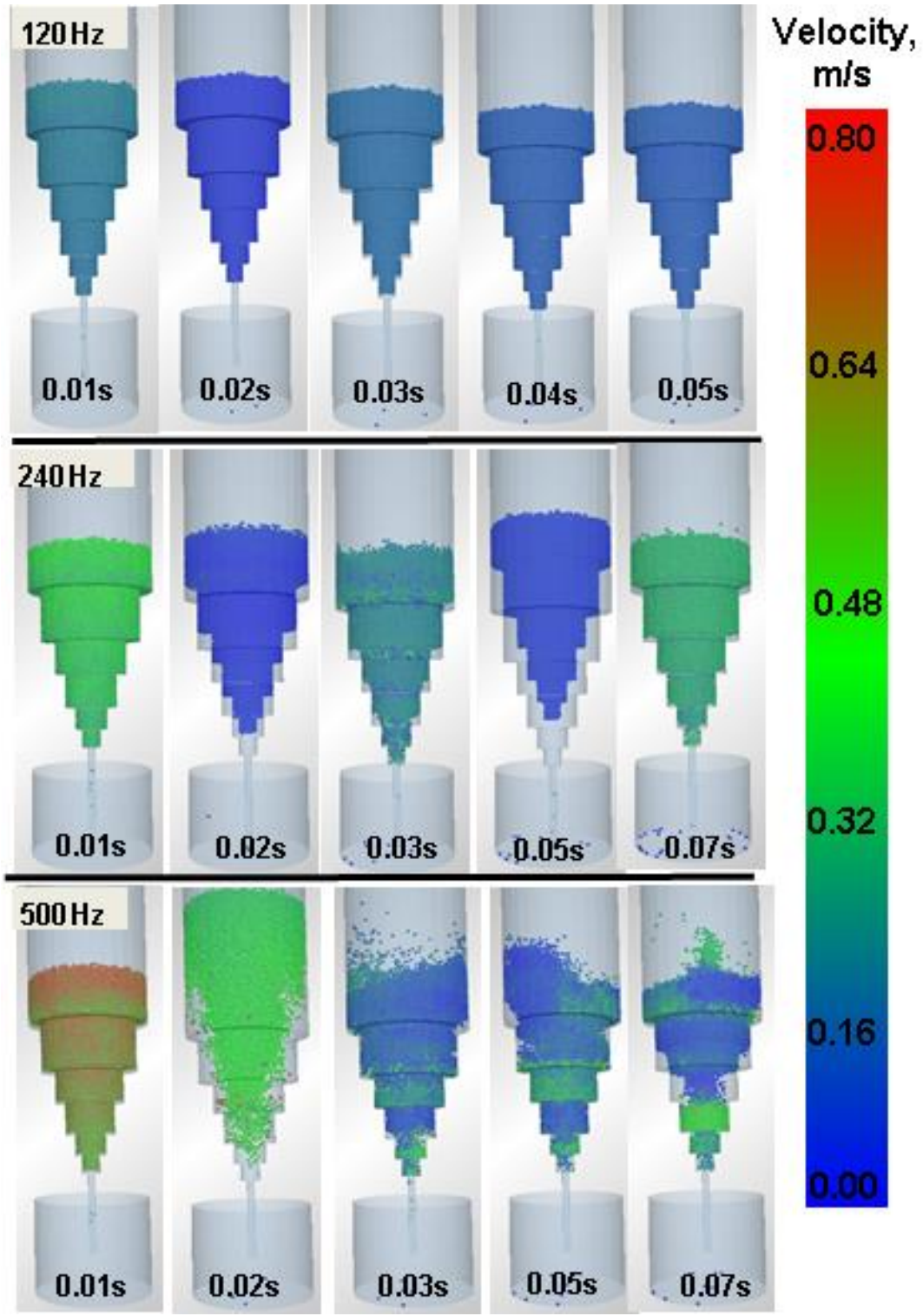

Figure 5.10 Frames from EDEM illustrating motion patterns of particles inside the hopper for different frequencies. The particle velocities are color-coded.

The cup seen in the image (into which the particles are discharged) is a feature of the model and is not present in the actual experiment, where particles are removed by an air flow. The color scale represents velocity, red being the maximum and green the minimum for each simulation. At 120 Hz, the particles appear to closely follow the hopper motion collectively. At 240 Hz, the powder bed begins fluidizing. Finally, at 500 Hz, well-fluidized motion patterns are observed; there are significant differences in the particle velocities throughout the sample.

Particle velocity histograms are shown in Fig. 11. Velocities of individual particles were saved at each sampling interval (0.01 s) during the entire simulation time (0.1 s). The histograms represent the data integrated over the entire simulation. The initial simulation period (0-0.01 s) was provided for the particles to completely settle down and hence, the velocities at this time were not considered for this processing. The values of velocities are relatively low (compared to several m/s typical for interaction of macroscopic bodies, such as milling balls [103]). For 120 Hz, there are several narrowly defined spikes corresponding to velocities less than 0.5 m/s. This pattern is likely to represent collective motion of the powder interacting with the vibrating hopper. A qualitatively similar velocity pattern is observed for 240 Hz. For 500 Hz, the velocity distribution changes substantially. Instead of discrete narrow peaks, a broader distribution is observed, indicative of substantial energy exchange among individual

colliding particles. This change in the velocity pattern is consistent with the appearance of the fluidized powder in Figure 5.10.

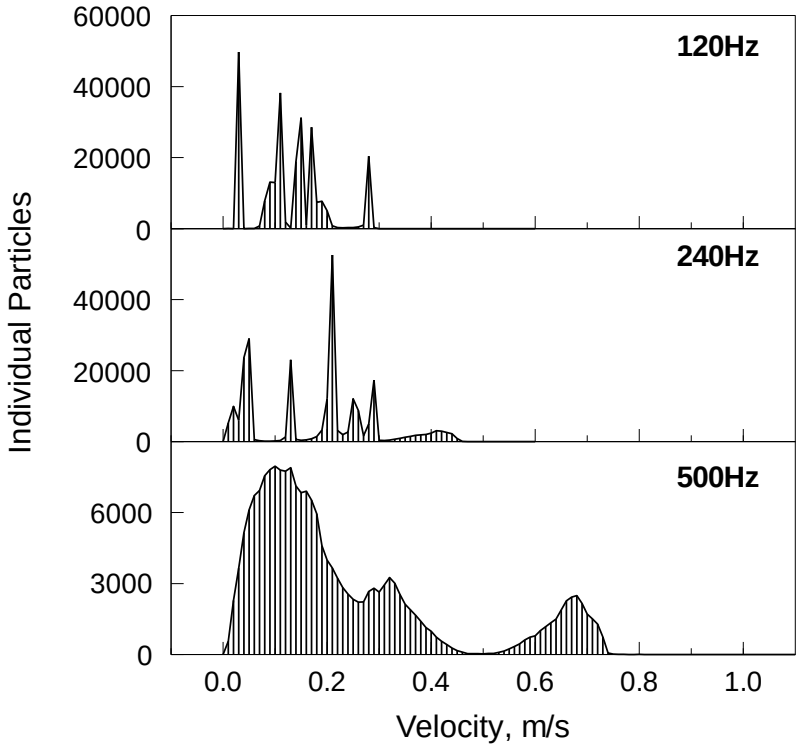

Figure 5.11 Velocity histograms for individual particles obtained from EDEM.

5.4.3 Sensitivity of DEM Predictions to Coefficients of Restitution and Friction.

Three interaction parameters, including coefficients of rolling and static friction, μ_r and μ_s, respectively, and coefficient of restitution, C_R, need to be defined for both particle-particle (PP) and particle- wall (PW) interactions. Thus, a total of six parameters (cf. Table 3) should be identified. The following calculations are aimed to establish how important is the selection of each individual interaction parameter for the prediction of the powder flow rate. Predicted results are compared to one another, whereas

comparison with experiments is discussed later, after the effects of particle size distribution, amount of powder, vibration pattern, and amplitude are considered. A comprehensive list of all the simulation runs is presented in Table C.1 in the appendix.

5.4.3.1 Restitution Coefficient

The effect of C_R on the predicted powder discharge rate is illustrated in Figure 5.12. For these calculations, the oscillation frequency was taken as 240 Hz and 20,000 of mono-dispersed particles were considered. Coefficients of restitution and friction were the same for both PP and PW interactions for each calculation. It is observed that for low values of C_R<0.5, its effect on the discharge rate is relatively small. However, for C_R > 0.5, its increase results in a substantial growth in the predicted discharge rate. A qualitatively similar effect of C_R on the discharge rate was also observed for other frequencies and values of μ_s and μ_r.

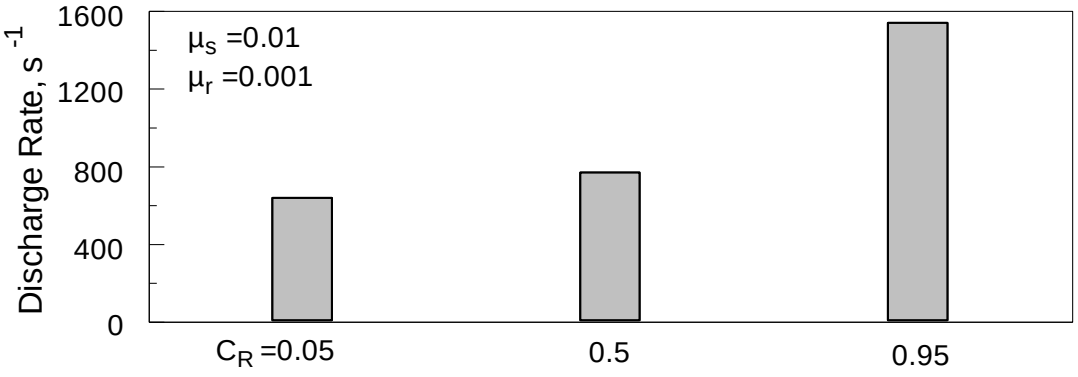

Figure 5.12 Effect of coefficient of restitution; vibration frequency 240 Hz (Runs 1-3, Table C.1).

A relative effect of C_R for PP and PW interactions is illustrated in Figure 5.13. A reduction in C_R for either of the individual PP or PW interactions results in a substantially lower predicted discharge rate. The effect of PP interactions appears to be somewhat stronger.

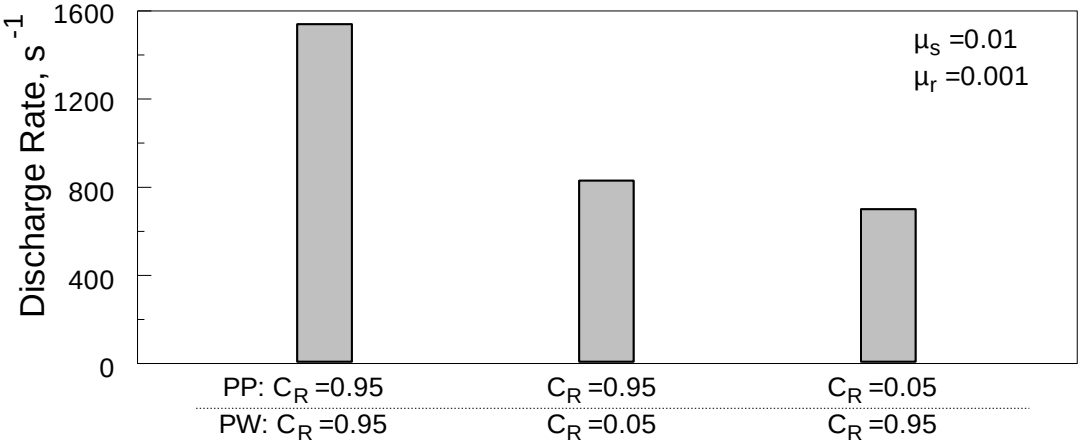

Figure 5.13 Effect of coefficient of restitution: particle vs. wall interactions; vibration frequency 240 Hz (Runs 3-5, Table C.1).

5.4.3.2 Friction Coefficient

Effect of changes in the values of μ_s and μ_r on the discharge rate is illustrated in Figure 5.14. The value of C_R=0.5 for both PP and PW interactions. As earlier, 240 Hz vibrations are considered for 20,000 of mono-disperse particles. The values of friction coefficients are reduced systematically compared to those given in Table 5.3, according to a general trend expected for fine powders. A reduction on the PP friction coefficients results in a greater increase in the predicted discharge rate compared to a similar change

in the PW friction. Altering both PP and PW friction coefficient results in the most significant increase in the predicted discharge rate.

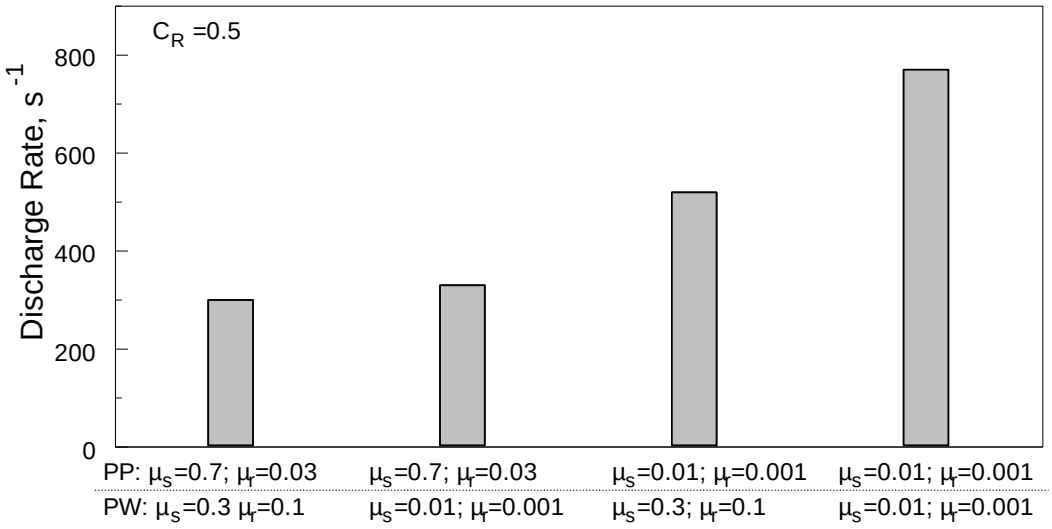

Figure 5.14 Effect of friction coefficient: particle vs. wall interactions; vibration frequency 240 Hz (Runs 2, 6-8, Table C.1).

5.4.3.3 Static vs. Rolling Friction

Individual effects of changes in static and rolling friction coefficients for PP interactions on the predicted discharge rate are illustrated in Figure 5.15. A reduction in the PP coefficient of static friction results in a relatively small increase in the discharge rate. An increase in the discharge rate is strong when the rolling friction coefficient is reduced from 0.003 to 0.001. Somewhat unexpectedly, the discharge rate decreases, when further reduction in the rolling friction coefficient is considered. Although Figure 5.15 only shows results for one set of calculations, a qualitatively similar behavior indicating a

non-monotonic change in the discharge rate as a function of μ_r for PP interactions was observed for different vibration frequencies.

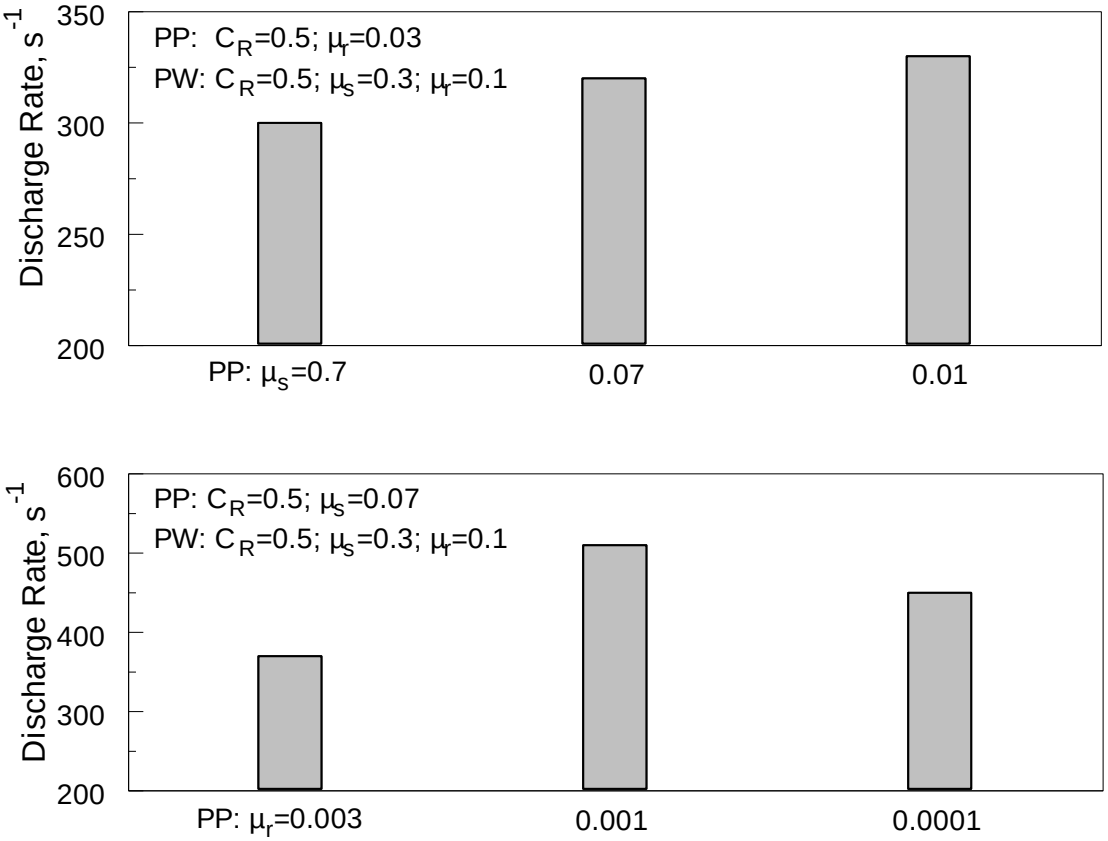

Figure 5.15 Effect of individual static and rolling friction coefficients for PP interactions; vibration frequency 240 Hz. (Top: Runs 9-11; Bottom: Runs 12-14, Table C.1).

Sensitivity of the predicted discharge rate to the changes in the PW static and rolling friction coefficients is illustrated in Figure 5.16. Reduction in both μ_r and μ_s for the PW interaction results in an increase in the predicted discharge rate. The discharge rate is more sensitive to changes in μ_s.

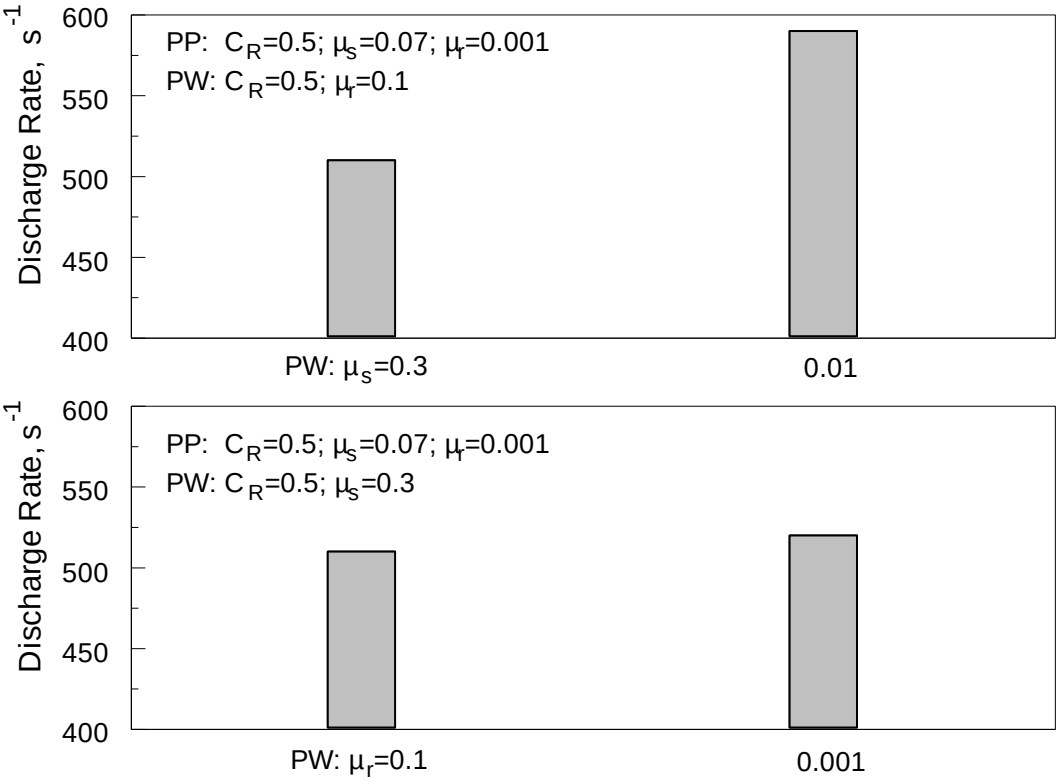

Figure 5.16 Effect of individual static and rolling frictions for PW interactions; vibration frequency 240 Hz. (Top: Runs 13, 15; Bottom: Runs 13, 16, Table C.1).

5.4.4 Sensitivity of DEM Predictions to Particle Size Distribution

Particle size distribution shown in Figure 5.7 was replicated in EDEM using an approach outlined earlier [125]. The particles were generated in individual size bins. Four bins were created simultaneously. The model generates particles from all bins randomly within the defined geometry (hopper), generated particles are allowed to fall down and settle in the gravitational field. It was observed that the particles of different sizes created by the code mixed uniformly while settling down in the hopper. Color coded images of the particles initially packed in the hopper were taken with the particles colored based on their sizes. It was clearly observed that differently sized particles were mixed

homogenously. The vibration of the hopper was started only after the particles were completely settled.

It was observed that even a very narrow particle size distribution accounted for in the DEM, results in a substantial change in the predicted discharge rate, as shown in Figure 5.17. Similarly to Figure 5.17, a reduced discharge rate was predicted when particle size distribution was accounted for while other process parameters were varied, including vibration amplitude, frequency, and friction coefficients.

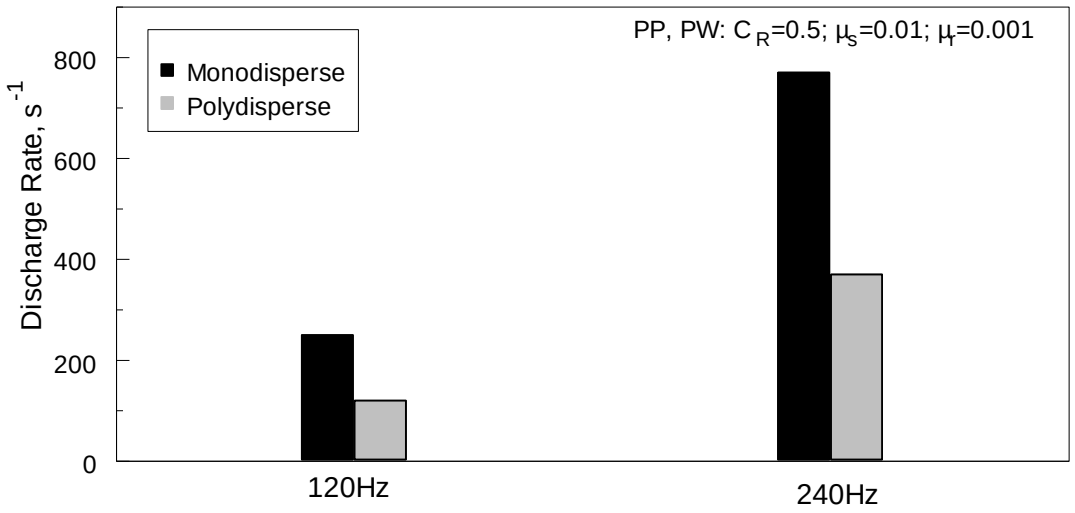

Figure 5.17 Effect of using a size distribution on the discharge rate (Runs 2, 17-19, Table C.1).

5.4.5 Sensitivity of DEM Predictions to the Vibration Amplitude

Amplitudes of vibrations measured using photographs of the exit tube were determined with a finite accuracy (see Table 5.2). The expected effect of the error in the measured vibration amplitude on the predicted discharge rate is shown in Figure 5.18. For both 120

and 500 Hz vibrations, an increase in the vibration amplitude results in an increase in the predicted discharge rate. Conversely, at 240 Hz, an increase in the amplitude causes a reduction in the discharge rate. It also appears that the sensitivity to the vibration amplitude is greatest for the 240 Hz case.

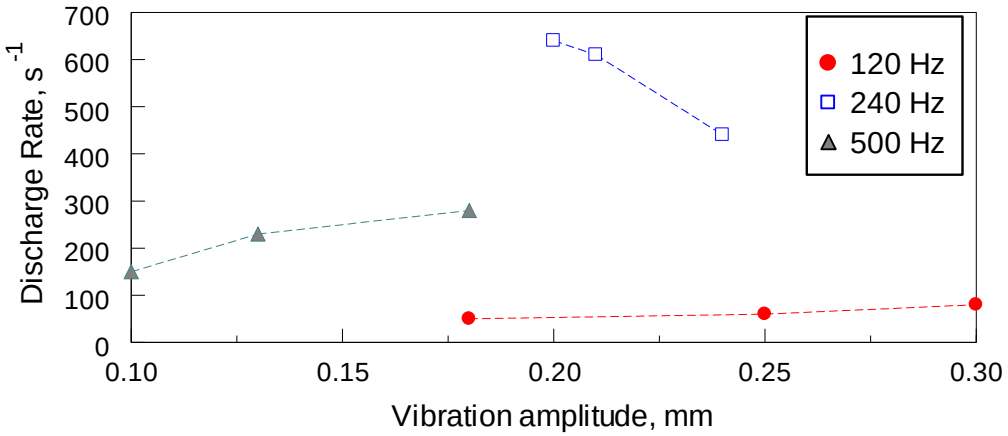

Figure 5.18 Sensitivity of different frequencies to change in amplitude. (Runs 1, 20, 21, in Table C.1)

5.4.6 Sensitivity of DEM Predictions to the Type of Vibratory Motion

As mentioned previously, two types of vibratory motions were tested. The first is a single sinusoidal oscillation and the second is a modulated wave obtained as a superposition of two sinusoidal vibrations. Discharge rates from the models obtained for these two situations are presented in Figure 5.19. All these simulations were performed with 5000 poly-dispersed particles using the friction and restitution data listed in Table 5.3. Further details can be found in Table C.1.

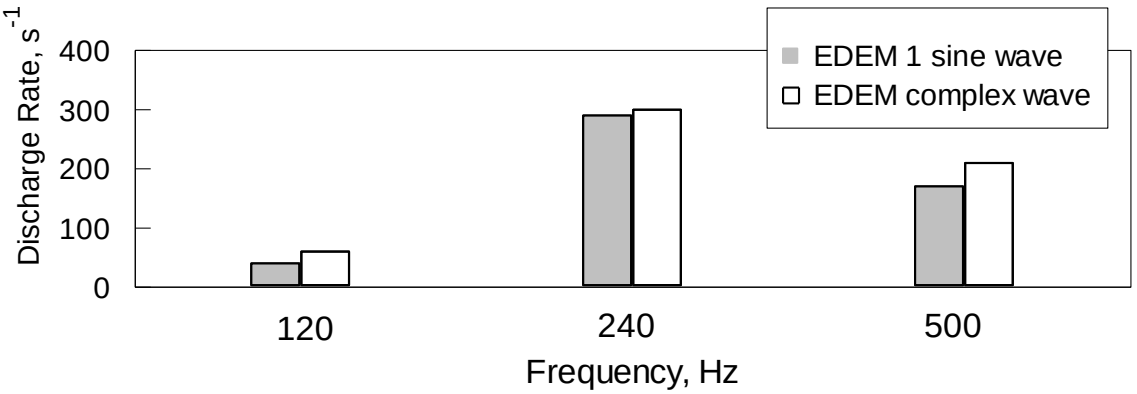

Figure 5.19 Effect of using a single size wave vs. a modulated wave on discharge rate. (Runs 22- 27 in Table C.1)

Using a modulated wave results in a slight increase in the discharge rate for 240 Hz and in a more substantial increase for both 120 and 500-Hz vibrations. Thus, using a modulated wave in DEM appears to be significant when the actual experimental conditions should be represented accurately.

5.5 Particle Interaction Parameters for Zirconia Beads

The appropriate interaction parameters should enable one to match the observed and predicted discharge rates for different vibration frequencies used. Based on the analysis presented in the previous section, it is concluded that poly-disperse powder should be considered in the model. Effect of the modulation is not negligible and a modulated wave should be employed by DEM for the final comparisons with experiments. It was also observed that both PP and PW interaction parameters are essential and need to be adjusted separately. Effect of each of the interaction parameters on the predicted

discharge rate was addressed in detail above for the vibration at 240 Hz. Because these effects may be different for different vibration frequencies, each frequency must be considered separately. Details of all computations performed in this study are given in the appendix, Table C.1, and the results are summarized in Table 5.4. It is remarkable that all parameters, including coefficient of restitution and both static and rolling coefficients of friction may affect the discharge rate in either proportional or inverse way, depending on frequency. Note that a limited range of parameter variation was considered, as shown in Table 5.4.

Table 5.4 Qualitative Effect of Change in Interaction Parameters on the Discharge Rate at Different Vibration Frequencies

Interaction Parameter		**Frequency, Hz**		
		120	**240**	**500**
PP	$0.50<C_R<0.75$	Proportional↑	Proportional↑	Inverse↓
	$0.07<\mu_s<0.7$	Inverse↓	Weak	Inverse↓
	$0.003<\mu_r<0.03$	Inverse↓	Inverse↓	Proportional↑
PW	$0.50<C_R<0.75$	Proportional↑	Proportional↑	Inverse↓
	$0.03<\mu_s<0.3$	Weak	Inverse↓	Proportional↑
	$0.01<\mu_r<0.1$	Inverse↓	Weak	Proportional↑

Using findings shown in Table 5.4 as a guideline, the values of interaction parameters were selected to achieve the closest match with the experimental data, as shown in Figure 5.20. In these calculations, 5000 poly-disperse particles and modulated amplitude vibration were considered. Considering the experimental errors, the fine tuning of the values of C_R, μ_s, and μ_r for both PP and PW interactions was not attempted; instead, an

approximate range of values was found for each parameter that enabled us to approach the experimental data for all frequencies simultaneously. The results are shown in Figure 5.20. Experimental data are compared to predictions obtained using the restitution and friction coefficients shown in Table 5.3 and newly identified friction coefficients enabling a better match with experiments.

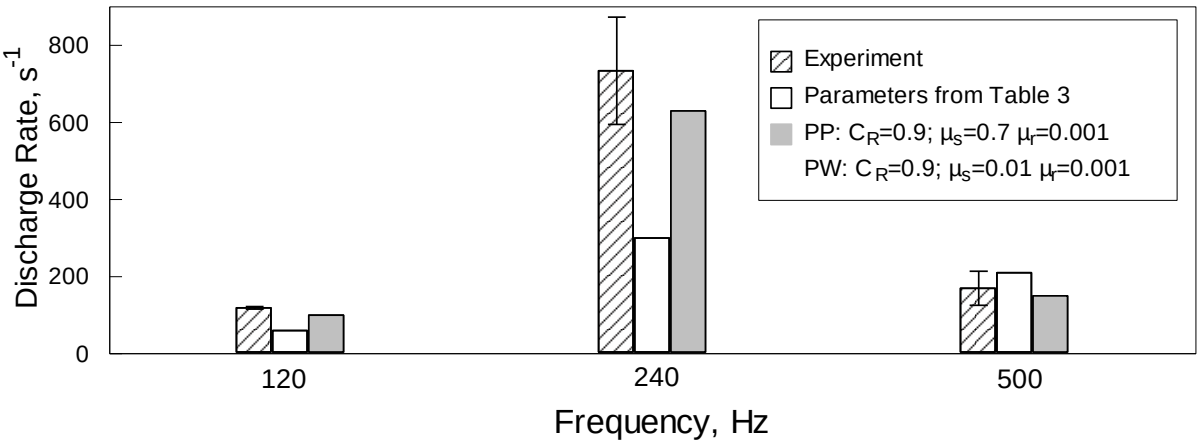

Figure 5.20 Effect of change in individual parameters for different frequencies (Runs 25-30 in Table C.1). The legend shows the values of friction and restitution coefficients.

Finally, the effect of the total number of particles on the simulation results is illustrated in Figure 5.21. Instead of 5000 particles used in preliminary calculations, 20,000 particles were used for the final comparisons of the experimental and predicted discharge rates. It is observed that the match improves further when a greater number of particles are used. However, the effect of the number of particles is relatively weak,

supporting the present observations of a relatively consistent discharge rate throughout the experiment, while the amount of powder in the hopper was decreasing.

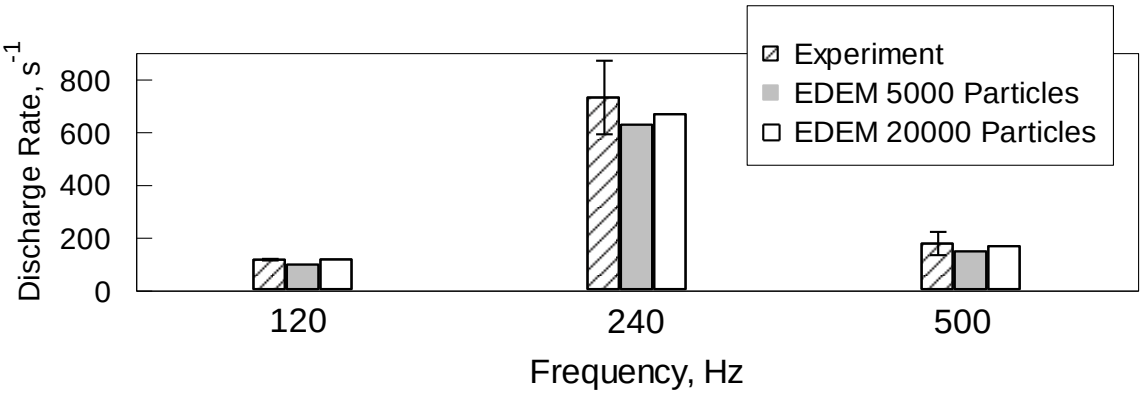

Figure 5.21 Discharge rate for different frequencies conducted using a modulated wave. Effect of using a higher number of particles is shown. Runs 28-33 Table C.1).

5.6 Discussion

It is possible that the trends identified here for the effects of different interaction parameters on the discharge rate or, more generically, on the dynamics of particular motion, may change if powders of different materials are considered. It is most likely that the changes in the predicted discharge rate for different particle size distribution, vibration modulation, and amplitude are mostly affected by the type of powder motion. In all cases, it is clearly established that neglecting to account for either of the considered parameters would cause gross errors in the DEM-predicted powder flow. It is particularly interesting that using an even very narrow particle size distribution changes the results critically, making it possible to match the experiment, compared to the calculation with the uniform particle sizes over-predicting the discharge rates substantially.

It is not surprising that changes in both restitution and friction coefficients for the PP interactions affect the predicted discharge rate stronger than comparable changes in the PW interaction parameters. Based on the number of interactions, PP interactions dominate and this domination becomes more significant for greater numbers of particles.

Considering that the relative particle velocities in the present calculations and experiments are low (Figure 10 and Figure 11), the high value of C_R=0.9 required to match the calculations and experiment appears to support an inverse relationship between C_R and the particle velocity proposed in the literature [103, 107, 108].

The observed effect of friction coefficients on the discharge rate for the high frequency oscillation (500 Hz) is surprising for the cases when an increase in the friction coefficient results in an increase in the discharge rate (Table 5.4). Similarly surprising is a reduction in the predicted discharge rate for very low coefficients of rolling friction for the PP interactions, as shown in Figure 5.15. Qualitatively, it may be proposed that there are situations when low friction and associated inefficient energy dissipation among moving powder particles slow down their re-distribution in the hopper. On the other hand, particle packing needs to be continuously re-adjusted in order to allow a flow of particles.

5.7 Conclusions

The most significant outcomes of the present work are an illustration of the importance of different simulation parameters on the accuracy of the DEM representation of a powder flow, and a methodology combining a small scale experiment and its DEM description enabling one to identify the appropriate interaction parameters for powder systems. The experiment uses a miniature vibrating hopper and can be applied to characterize the powder flow for different powders with varied compositions and particle size distributions.

It is shown, in particular, that all six interaction parameters, including coefficients of restitution, rolling and static friction characterizing both particle-particle and particle-wall interactions must be carefully selected. The values of these parameters for powders are generally not the same as those established for macroscopic bodies. One exception identified in this work for zirconia beads is the static friction coefficient for particle-particle interactions, which appears to closely match that used for larger zirconia spheres.

It is shown that the effect of different interaction parameters on the powder flow may be both direct and inverse, depending on the vibration frequency. For zirconia powder fed in a brass hopper, it is established that C_R=0.9 and μ_r=0.001 for both PP and PW interactions. The values of μ_s are 0.7 and 0.01, for the PP and PW interactions, respectively.

In addition to selecting the appropriate friction and restitution coefficients, it is shown that considering a realistic particle size distribution in DEM affects the calculations substantially. Weaker, but not negligible effects are established for the vibration amplitude, accounting for the modulation of the vibratory motions, and for using a realistic number of interacting particles.

CHAPTER 6

CONCLUSIONS AND FUTURE WORK

6.1 Conclusions

In the first segment of this thesis, a scale-up model was developed based on the concept of milling dose, which is defined as the ratio of the energy transferred to the powder from the milling tools to the mass of the milled powder. This concept has been shown to be able to provide a universally useful description of the milling progress, irrespective of devices and milling conditions. Importantly, the energy transfer by both impact and friction must be considered. To account for the friction, both sliding and rolling motions of the milling balls in which the energy is transferred to the material being milled must be considered. The DEM-calculated rate of energy dissipation multiplied by the experimental milling time enables one to calculate the energy transferred to the powder from the milling tools. This energy directly determines the material refinement. Once it is found for a material prepared in a specific milling configuration, it can be used for predicting milling time required to prepare that material using a new milling device or altered milling conditions.

For a useful and accurate description of the milling process in DEM, experimentally validated values for restitution and friction coefficients are necessary. Both static and rolling friction coefficients were obtained comparing simple experiments

with powder-coated milling balls rolling inside the milling vial. The same experiment was directly modeled by DEM. A comparison of the experimental and observed ball motion patterns enabled us to determine the appropriate friction coefficients.

The DEM calculations for shaker and planetary mills were found to be accurate. However, the energy dissipation predicted by the attritor DEM model was much higher than expected. It was discovered that the calculated energy dissipation in this device included contribution from events with abnormally high forces, which were a result of breaking jams occurring inside the mill. Such jamming of the milling media and its subsequent release resulted in high forces in the model stemmed from the constant rate of the impeller's rotation. The magnitudes of the predicted forces were not realistic. Hence, it was proposed to filter out such high-force, long duration events from further analysis of powder refinement in the attritor mill. After this filtering, a much better correlation of the experimentally achieved powder refinement and DEM predictions was obtained. Subsequently, the milling dose calculated for all three milling devices became comparable to each other and the validity of the developed scale-up approach was established.

In the process of validation of the scale-up model, extensive experiments were conducted which were used as indicators of milling progress. In these experiments, the same powder was prepared in three milling devices, including shaker, planetary, and attritor mills. Partially milled samples were recovered at regular time intervals and yield

strength was measured for each of these samples. The yield strength was treated as a milling progress indicator, increasing at longer milling times. In the second phase of this thesis, a distinctive approach to characterize milling progress, which would eliminate the extensive experimental procedures, was investigated. Subsequently, *in-situ* measurements of such parameters as power, torque, etc., readily quantifiable during the milling, were identified as a potential replacement for the extensive sample characterization efforts and thus, indicators of material refinement.

Metal-matrix-composites were found to be suitable candidates to pursue this study. As an authentication, changes in structural and mechanical characteristics of these materials prepared by mechanical milling recovered at different milling times were compared to changes in the parameters characterizing milling process in real time. It was discovered that before utilizing this procedure for tracking milling progress, it is essential to know the hardness of the material being milled relative to the milling media. For the material with components softer than the milling media, increasing yield strength, and structural refinement directly correlated with increasing motor power, torque, as well as with increase in the amplitudes of rapid oscillations of all milling process parameters. For the material with a starting component harder than the milling media, the abrasive action of the harder starting particles (becoming less significant at longer milling times) affected the motor power and torque stronger than the hardening of the prepared composite.

Overall, changes in the milling process parameters measured in real time were found useful in tracking the milling progress, although the reduction in the power and torque (as opposed to their increase) correlated with the material refinement. This technique was found to be quite effective and even minute changes in morphology such as the formation of flakes at early milling times could be correlated with real time measurements.

During the initial development of scale-up model, it was reported that the attritor mill model resulted in substantially high force events as a result of the jamming events inside the model. In actual experiments, such jamming events indeed occur, however the motor develops an appropriate response, which provides an additional torque for the impeller to overcome the jam. Replicating such a "responsive" impeller in DEM was the objective of the third portion of this thesis.

It is shown that in the model, the rotation of such "responsive" impeller can be described using an experimentally obtained correlation between instantaneous values of torque and rotation rate. This correlation can be programmed into DEM to describe the torque applied to the impeller for the range of rotation rates observed experimentally. When the rotation rate falls below the experimental range, the torque needs to be further increased. The accuracy of DEM representation of material processing in an attritor is significantly improved when interactions of the moving impeller and the milling balls are accounted for by enabling the impeller to instantaneously slow down when the balls jam,

and then return to its pre-set rotation rate. The performance of this responsive impeller was tested with different materials, and it was found to accurately predict the energy dissipation rate or power for all programmed cases. Hence, this advance model aids in eliminating the superficial filtering process that had to be conducted initially in the scale-up model development.

The final chapter in this thesis focuses on development of a novel methodology for identification of friction and restitution coefficients for particle-scale DEM studies. The lack of appropriate values for such coefficients is a major omission in existing research utilizing DEM descriptions to understand various unit operations. A miniature vibratory hopper feeder was developed and used to feed several fine spherical powders. The hopper was directly described in DEM. In calculations, sensitivity of the DEM predictions to selection of different interaction parameters, using mono-disperse vs. poly-disperse powder models, accurately representing vibration pattern and amplitude were quantified. Further, comparing experimental and predicted powder discharge rates, appropriate values of coefficients of restitution and friction were established for both particle-particle and particle-wall interactions. The developed approach combining miniature hopper experiment and its DEM description can be used in the future to characterize interaction parameters for different fine powders.

6.2 Future Work

A few suggestions for future directions that could be pursued based on the investigation and outcomes from this thesis are presented in this final section.

In the initial development of the scale-up model, experimental validation was achieved via tracking the mechanical as well as structural properties of the prepared non-reactive composites. In addition to this, perhaps advanced reactive materials could be prepared and characterized with the same intent, to further establish the modeling approach. In addition to the transfer of manufacturing from one device to another or small to large scale, a model based on study of reactive materials could potentially even serve as a way of prediction of "safe" manufacturing conditions for such materials.

The use of *in-situ*, real-time indicators of milling refinement was focused on the attritor mill in this thesis. Taking this study forward, such an indicator could perhaps be also obtained in the planetary and shaker mill. The author recommends temperature monitoring as one of the ways to accomplish this goal.

An important shortcoming was encountered during the real-time milling progress assessment for materials milled at cryogenic temperatures. For these materials, it was observed that the power, torque and variations thereof remained essentially constant during the entire milling duration (around 24 hours). Details of these measurements are provided in the appendix. Hence, it was not possible to predict powder morphological changes and milling behaviors for cryogenically milled samples as exhibited for powders

milled at room temperature (Chapter 3). This is an important concern since some of the sensitive materials can currently be prepared in laboratory scale only under cryogenic temperatures. Reasons for the incompetence of current real time parameters for such materials as well as other non-invasive monitoring techniques need to be explored.

Although the current work as well as all the other modeling approaches reported in literature contribute towards a better understanding of the ball-milling process itself, it would be interesting to consider a "dynamic" model as opposed to the a "steady-state" one. It is a known fact that powders undergo welding, fracture and agglomeration as milling progresses. In this thesis, the morphological transitions were also shown via real-time measurements in collaboration with scanning electron microscope images of partially milled samples. When these modifications happen, the properties of the milled samples in terms of hardness, cohesivity, etc., are rapidly changing. The thickness of coating on the milling media is rapidly changing as well. Thereby, the interaction parameters (friction, restitution coefficients) of the milling media are modified with time. Having said that, the possibility of developing a model, which contains "dynamic" parameters such that it can perhaps account for the variations the powders go through inside the mill with time, is most fascinating. It can be contemplated that an advanced model of this nature would perhaps contain time sensitive interaction and physical properties. In fact, another varying factor could be the force model itself. In all of the presented results, the Hertz-Mindlin force model was utilized. In literature, it has been

presented to run a more advanced and effective calculation than the linear spring dashpot model and hence, was a straightforward choice. However, if one considers the development of a dynamic model, then a transition from simplistic force model to a model including cohesion or even electrostatics-incorporated case could be considered.

In literature, a few reports were found that boast of a better calculation in DEM when a velocity dependent restitution coefficient is used. Some of these works were cited in Chapter 5 of this thesis. The motivation for these studies came from one of the primary caveats in the existing Hertz-Mindlin model, which is the factor deciding the end of contact. In the current Hertz-Mindlin model, a contact ends when the displacement returns to zero and this results in a net normal attractive force at the end of a contact. The current argument is that contact, in fact, should end when the force returns to zero and not the displacement. A few authors [126-128] have therefore presented the need for a velocity-varying coefficient of restitution. However, all of the numerical developments are based on two-body collisions and it appears that the problem of multiple body collisions and resulting mathematical problem of varying velocities and restitution coefficients has not been solved yet. This could result in an extensive study if pursued and would be quite a valuable contribution to multi-body simulation studies.

During the operation of the attritor mill, the entire vial-cooling jacket assembly was also observed to wobble at the instances where the impeller “responses” to potential jamming conditions. Such a “responsive” vial was not incorporated in the current study

and it would be interesting to see the outcomes of such a model. It is anticipated that maybe that would make the model outcomes even better and improve the milling dose comparisons.

For preparation of advanced materials with tailored particle sizes, a unique two-step milling methodology was recently developed in this research group [129]. In such an approach, the samples are first milled under one set of milling conditions and the resultant materials are then subjected to a different set of conditions (in the same device). It would be quite interesting to think about how such a process could be effectively modeled in DEM such that appropriate scale-up parameters can be obtained.

APPENDIX A

REAL-TIME INDICATORS OF MILLING PROGRESS: CRYOGENIC SYSTEMS

The real-time milling progress indicators for two cryogenic temperatures are presented.

The left and right groups presented in Figure A.1 carry no specific reason.

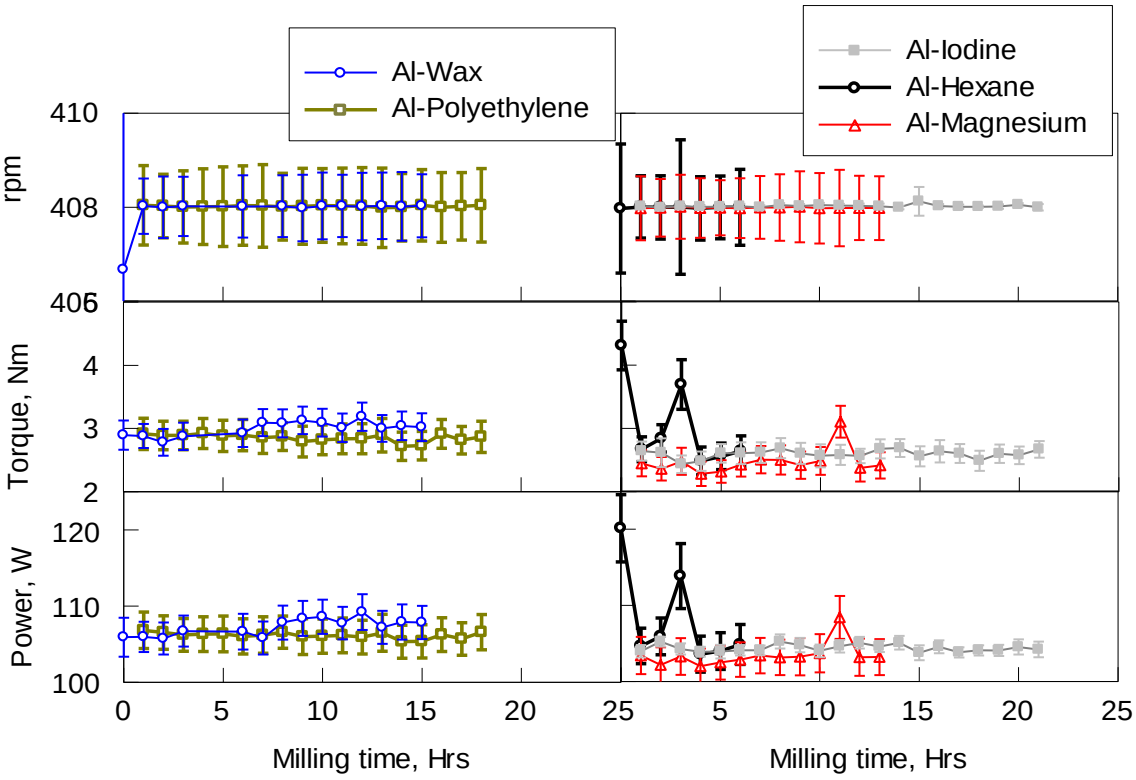

Figure A.1 Real-time measurements of impeller rotation speed, torque and power for five systems. The average and standard deviations are shown.

APPENDIX B

EFFECT OF HARD-SOFT COMPONENTS IN ATTRITOR MILL PROCESSING

In chapter 3, the effect of powders being harder or softer than milling media was discussed. Another system is added to the same comparison and characterization results are presented here.

Table B.1 List of Hardness Values for Materials

Material	Vicker's Hardness, MPa
Al	167
MgO	660
Silica	8900
B_4C	4980
Steel (Milling media)	1700-2300

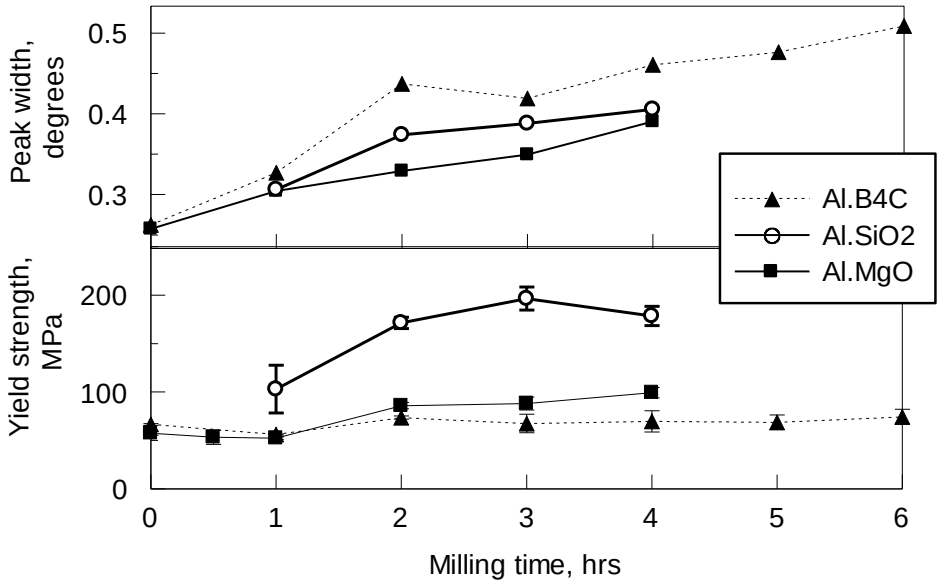

Figure B.1 Comparison of experimental milling time indicators for three material systems.

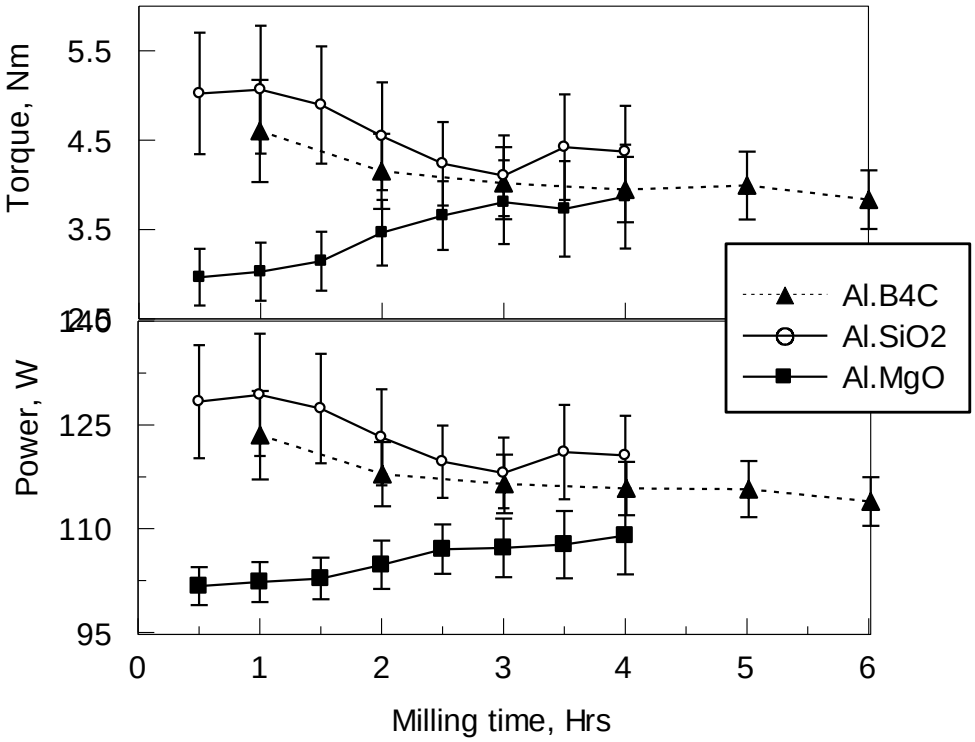

Figure B.2 Comparison of real time milling progress indicators for three material systems.

APPENDIX C

DETAILED LIST OF ALL PERFORMED SIMULATIONS

Table C.1 Detailed List of all Performed Simulations in Chapter 5

Sl #	Particle-Particle			Particle-Wall			Frequency, Hz	Particles	Number of particles	Amplitude	Discharge rate, #/s
	C_R	μ_s	μ_r	C_R	μ_s	μ_r					
1	0.05	0.01	0.001	0.05	0.01	0.001	240	M	20000	Sin	640
2	0.5	0.01	0.001	0.5	0.01	0.001	240	M	20000	Sin	770
3	0.95	0.01	0.001	0.95	0.01	0.001	240	M	20000	Sin	1540
4	0.95	0.01	0.001	0.05	0.01	0.001	240	M	20000	Sin	830
5	0.05	0.01	0.001	0.95	0.01	0.001	240	M	20000	Sin	700
6	0.5	0.7	0.03	0.5	0.3	0.1	240	M	20000	Sin	300
7	0.5	0.01	0.001	0.5	0.3	0.1	240	M	20000	Sin	520
8	0.5	0.7	0.03	0.5	0.01	0.001	240	M	20000	Sin	330
9	0.5	0.7	0.03	0.5	0.3	0.1	240	M	20000	Sin	300
10	0.5	0.07	0.03	0.5	0.3	0.1	240	M	20000	Sin	320
11	0.5	0.01	0.03	0.5	0.3	0.1	240	M	5000	Sin	330
12	0.5	0.07	0.003	0.5	0.3	0.1	240	M	5000	Sin	370
13	0.5	0.07	0.001	0.5	0.3	0.1	240	M	5000	Sin	510
14	0.5	0.07	0.0001	0.5	0.3	0.1	240	M	5000	Sin	450
15	0.5	0.07	0.001	0.5	0.01	0.1	240	M	5000	Sin	590
16	0.5	0.07	0.001	0.5	0.3	0.001	240	M	5000	Sin	520
17	0.5	0.01	0.001	0.5	0.01	0.001	120	M	5000	Sin	250
18	0.5	0.01	0.001	0.5	0.01	0.001	120	P	5000	Sin	120
19	0.5	0.01	0.001	0.5	0.01	0.001	240	P	5000	Sin	370
20	0.5	0.7	0.03	0.5	0.3	0.1	120	M	5000	Sin	50
21	0.9	0.7	0.03	0.9	0.3	0.1	500	P	5000	Sin	150
22	0.5	0.7	0.03	0.5	0.3	0.1	120	P	5000	Sin	40
23	0.5	0.7	0.03	0.5	0.3	0.1	240	P	5000	Sin	290
24	0.5	0.7	0.03	0.5	0.3	0.1	500	P	5000	Sin	180
25	0.5	0.7	0.03	0.5	0.3	0.1	120	P	5000	Mod	60
26	0.5	0.7	0.03	0.5	0.3	0.1	240	P	5000	Mod	300
27	0.5	0.7	0.03	0.5	0.3	0.1	500	P	5000	Mod	210
28	0.9	0.7	0.001	0.9	0.01	0.001	120	P	5000	Mod	100
29	0.9	0.7	0.001	0.9	0.01	0.001	240	P	5000	Mod	630
30	0.9	0.7	0.001	0.9	0.01	0.001	500	P	5000	Mod	150
31	0.9	0.7	0.001	0.9	0.01	0.001	120	P	20000	Mod	120
32	0.9	0.7	0.001	0.9	0.01	0.001	240	P	20000	Mod	670
33	0.9	0.7	0.001	0.9	0.01	0.001	500	P	20000	Mod	170

Legend:

C_R: Coefficient of Restitution, μ_s: Static friction, μ_r: Rolling friction, M: Mono-disperse, P: Poly-disperse, Sin: Sinusoidal wave, Mod: Modulated wave

APPENDIX D

ALUMINUM-TITANIUM SYSTEM STUDY FOR MILLING PROGRESS

Instead of the Aluminum-Magnesium Oxide results presented in Chapter 2, the study was initially done with Aluminum-Titanium (composition $Al_{0.8}Ti_{0.2}$). The results are shown here.

Table D.1: Milling Parameters for Aluminum Titanium System

Parameter	Mill		
	Attritor	Planetary	
Powder load, g	50	50	100
Charge ratio	36	3	3
Ball mass, g	1800	150	300

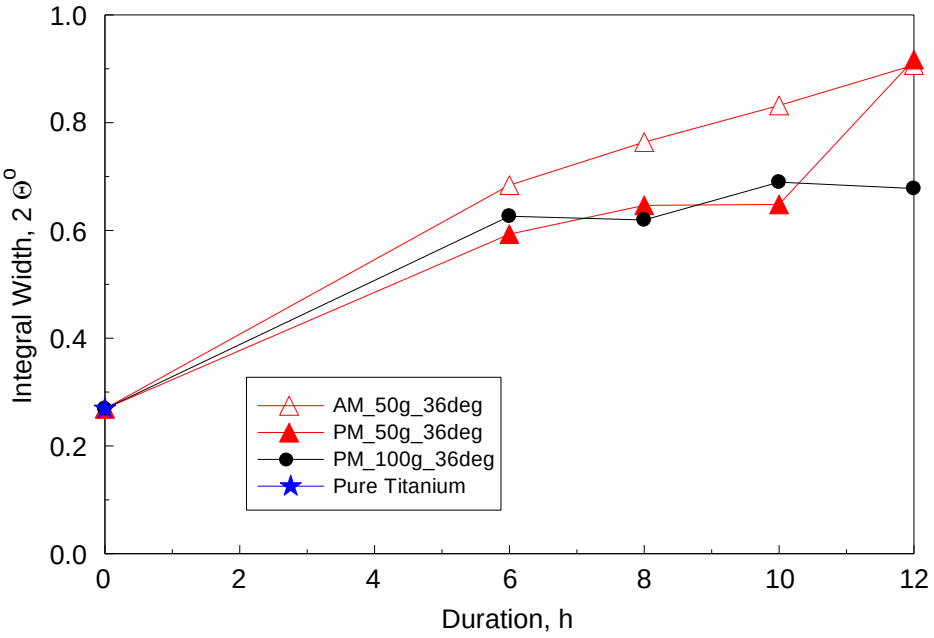

Figure D.1 Peak width data for Al-Ti prepared in different devices.

APPENDIX E

FRICTION COEFFICIENT RESULTS

This section presented the results of single-ball rolling experiments to obtain friction coefficients for systems not shown in the main chapters in this thesis.

Table E.1 Friction Coefficient Processing Results

Run	Milling Duration	Case	Friction Coefficient	
			Static	Rolling
Plain	N/A	Plain ball on plain vial	0.28	0.0075
Dry milling, Al·Ti	2 hours	Coated ball	0.17	0.02
		Highly coated ball	0.1	0.01
	8 hours	Coated ball	0.25	0.032
Wet milling, $8Al MoO_3$	15 min	Coated ball	0.1	0.09

APPENDIX F

AMPLITUDE RESULTS DETAILS

The amplitudes discussed in Chapter 5 were measured by monitoring both top and bottom position of the hopper tip. Detailed outcomes are shown in the following plot.

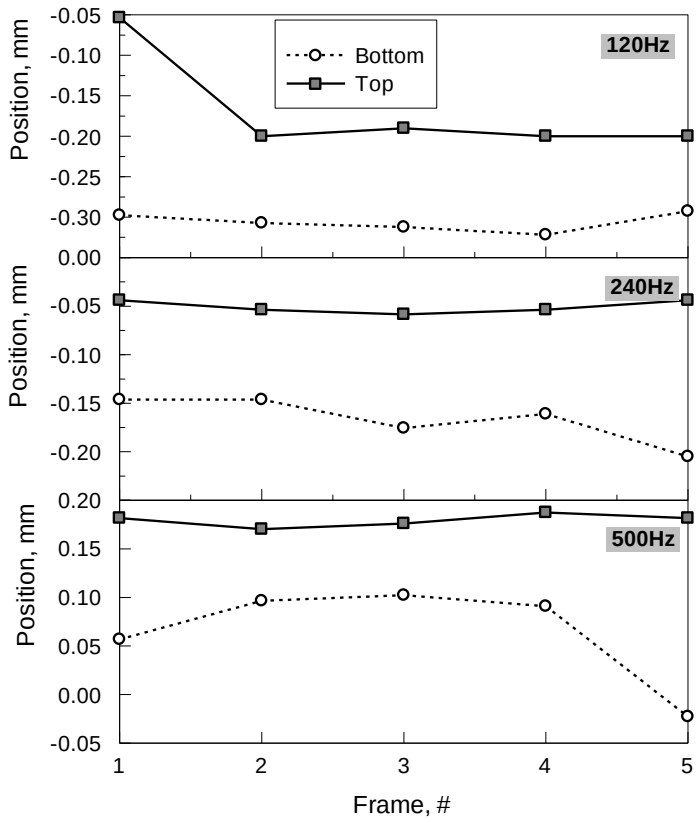

Figure F.1 Amplitude data calculated at each frame for different frequencies.

APPENDIX G

ADDITIONAL RESULTS FOR DIFFERENT MATERIAL SYSTEMS (ADDENDUM TO CHAPTER 5)

The experiments discussed in Chapter 5 for Zirconia were also performed for two other materials: PMMA and Titanium. The respective characterization and hopper discharge rate results are presented in this appendix.

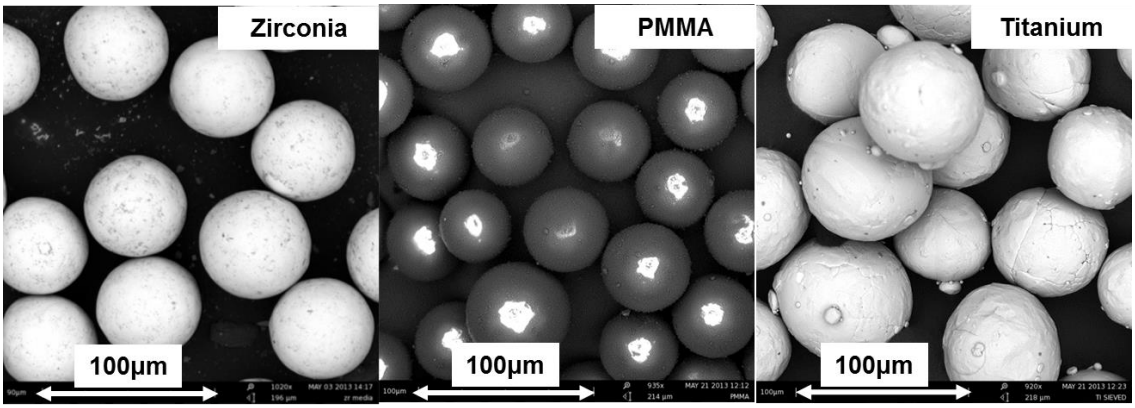

Figure G.1 SEM Images of the three material systems.

The particle size distributions for these materials are shown in Figure G.2. The outcomes for Zirconia and PMMA were obtained by image processing of SEM images (as described in Chapter 5). 323 and 217 particles were processed for Zirconia and PMMA respectively. The distribution for Titanium was obtained from a LS-230 Coulter device. This Titanium is manufactured by Super Conductors Inc. and the presented distribution was obtained after sieving the sample.

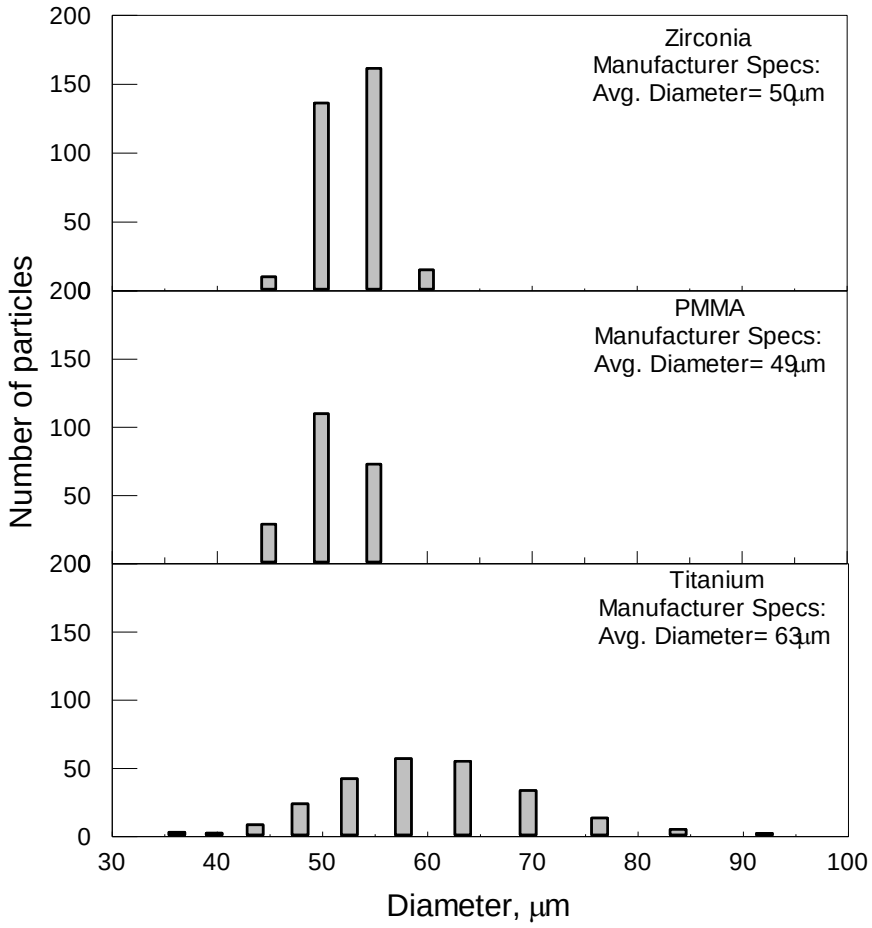

Figure G.2 Particle size distribution for the three cases.

Hopper discharge rates are shown in Figure G.3 and the percentage exited in Figure G.4.

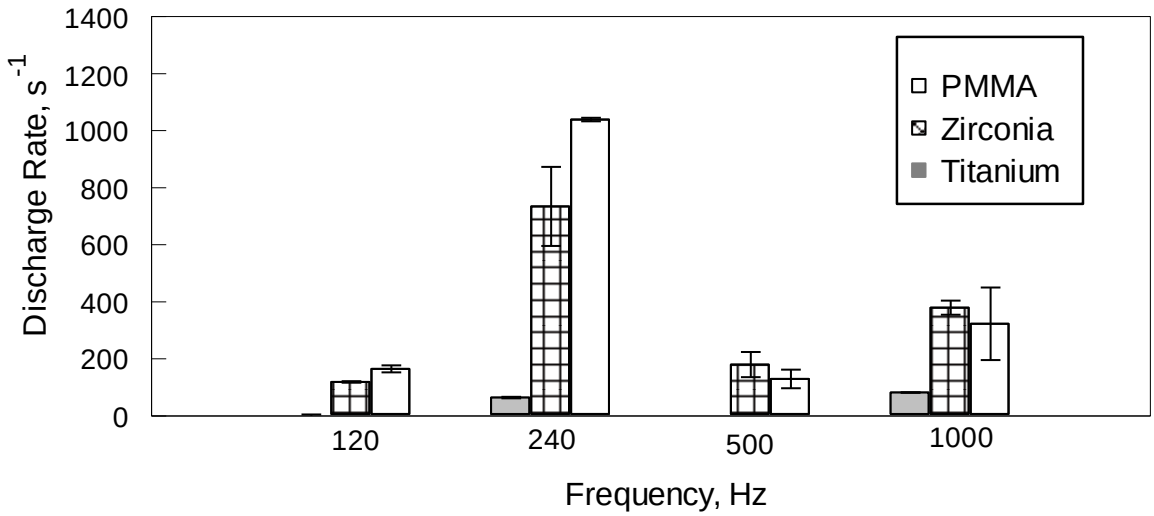

Figure G.3 Discharge rate comparisons for various cases.

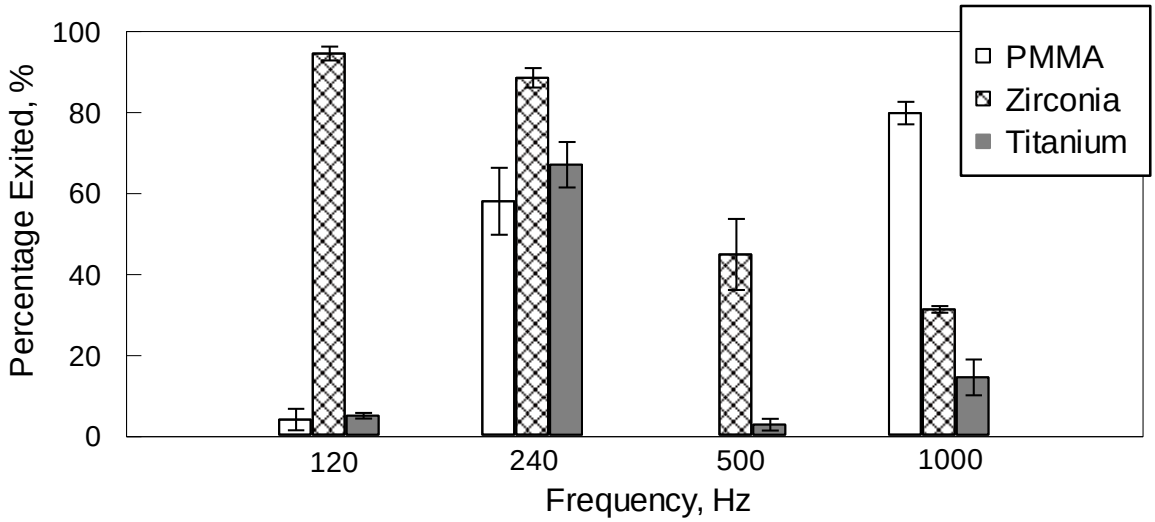

Figure G.4 Percentage mass exited at different frequencies for the three material systems.

Initially, when the PMT was set-up in these experiments, it was anticipated that the peak voltages measured for each particle could be used to interpret the particle sizes being discharged as well. Although this particular study was not pursued later, the results of the

peak voltages (obtained by processing of PMT pulses) for the three particle systems are shown in Figure G.5. The number of particles (or peaks) processed for each case are shown in the insets.

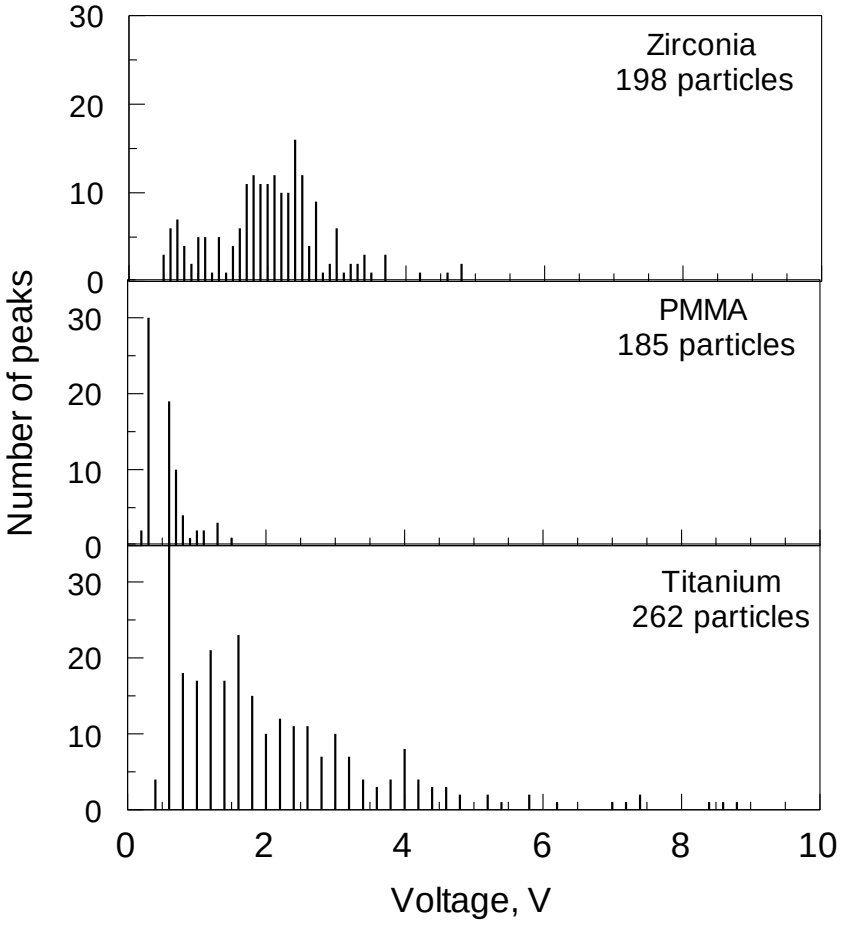

Figure G.5 Histograms of the measured voltage peaks for the three materials.

APPENDIX H

TRANSFER OF PARAMETERS FROM PLANETARY TO ATTRITOR: *IN-SITU* MEASUREMENTS

Both real time and experimental milling progress indicators are shown in Figure H.1.

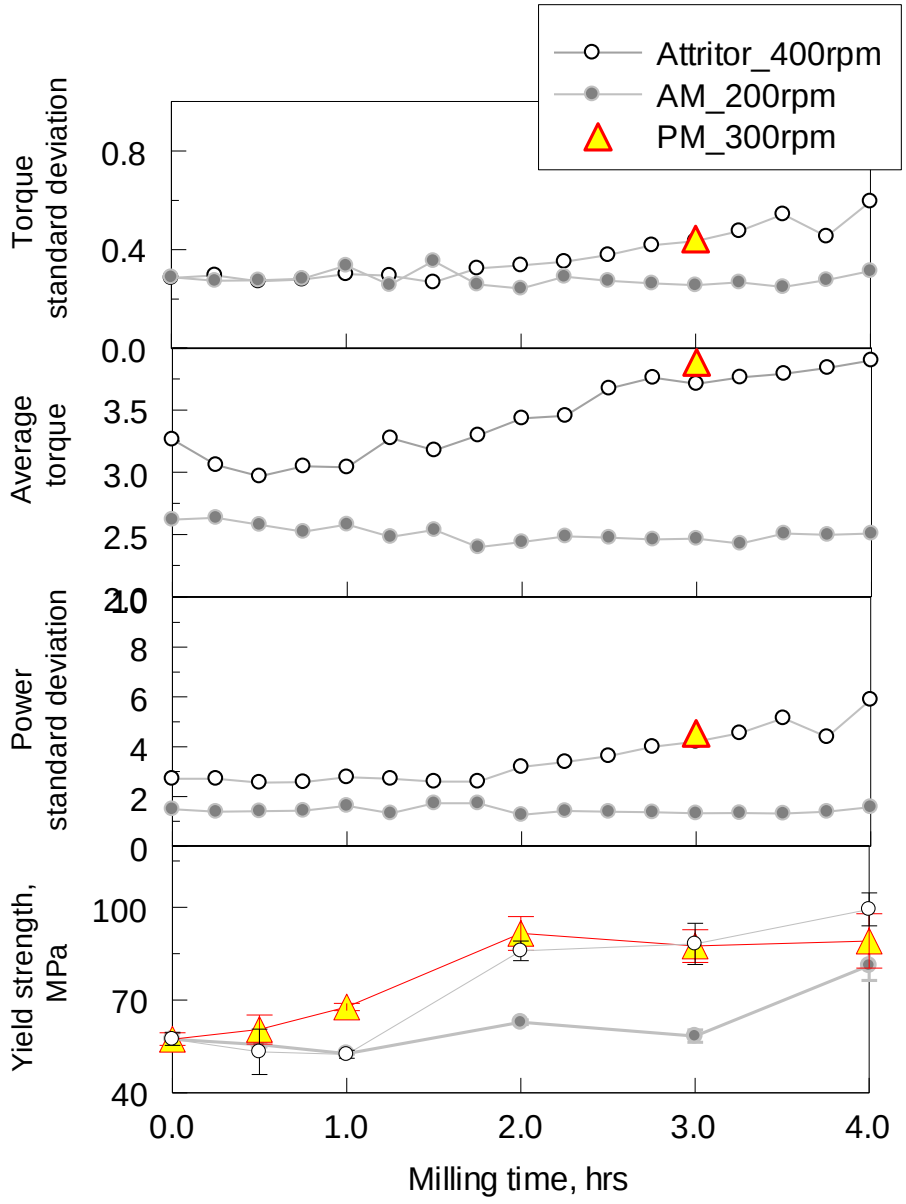

Figure H.1 Comparison of experimental and real-time milling progress indicators for transfer of sample from planetary to attritor mill. (powder mass is 50g).

After preparing the sample in planetary mill, the milled material was transferred to an attritor and the impeller rotation was initiated.

Here, the values of real time indicators for this powder (from planetary mill) were recorded. The usability of real-time indicators is further established here as we observe the planetary mill real time data is similar to where the experimental trends are.

APPENDIX I

RESULTS FOR LARGER ATTRITOR VIALS

Some experiments and EDEM calculations were performed with larger (1400cc) steel and ceramic vials. The corresponding results are presented in this appendix. The experimental results are limited for the larger vials and the reasons for the lack of data are different for steel and ceramic vials. A motor overload was observed in the ceramic vial, Perhaps this was caused due to the material of construction of the vial which could not "respond" or adjust to the jams the way steel vials do. In the case of larger steel vial, multiple deformations on the vial wall occurred during such jamming responses which resulted in the vial being stuck in the enclosure at the end of every experiment.

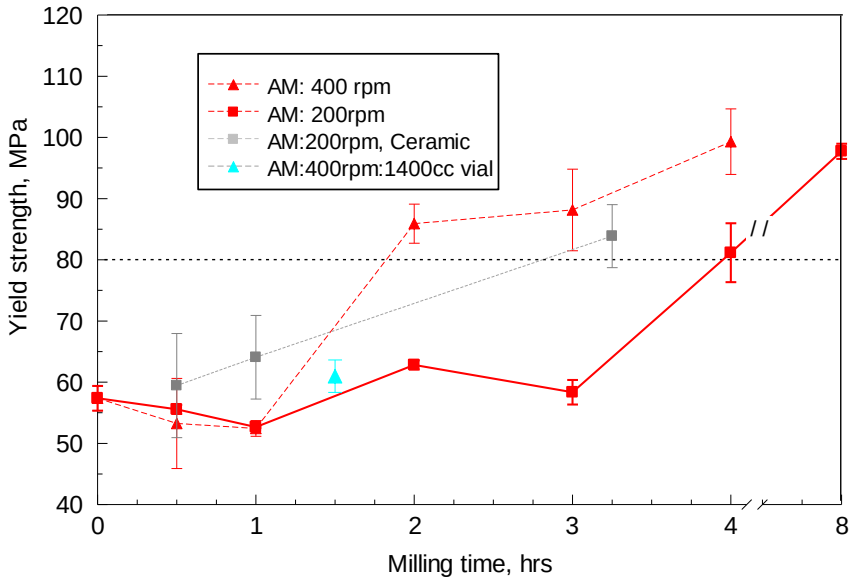

Figure I.1 Yield strength results for larger ceramic and steel vials relative to smaller attritor vials.

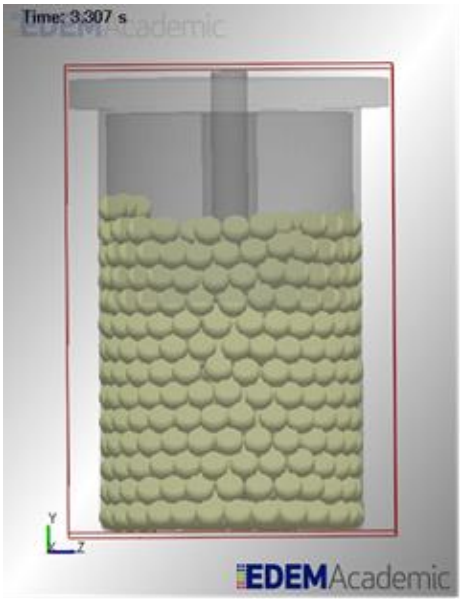

Figure I.2 DEM model of larger ceramic vial.

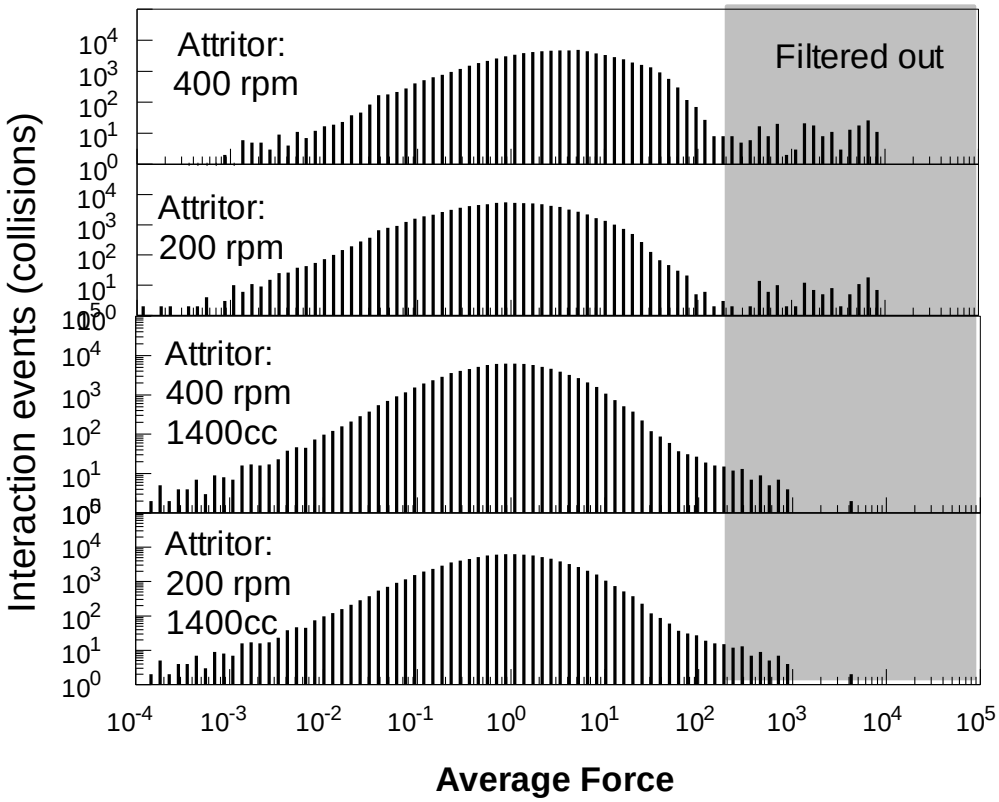

Figure I.3 Histograms of events sorted based on average force during the simulation for smaller and larger vials are depicted.

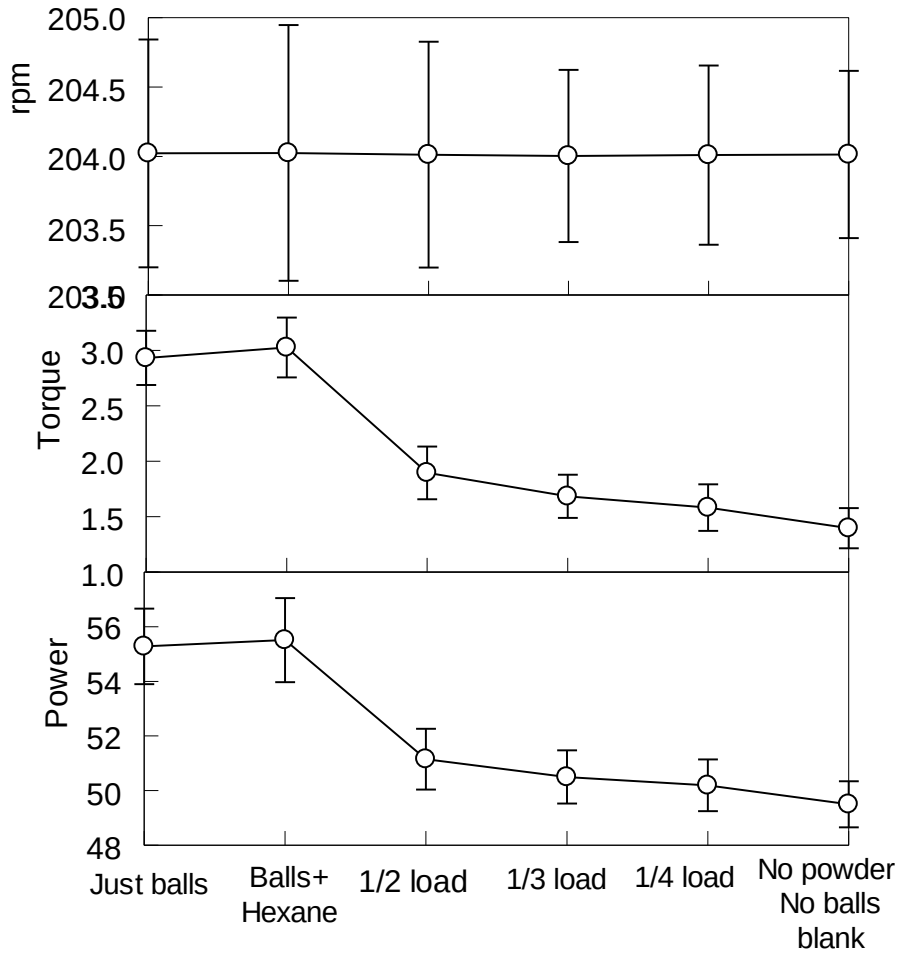

Figure I.4 Results of parametric investigation for ceramic 1400cc vial operated at 200rpm.

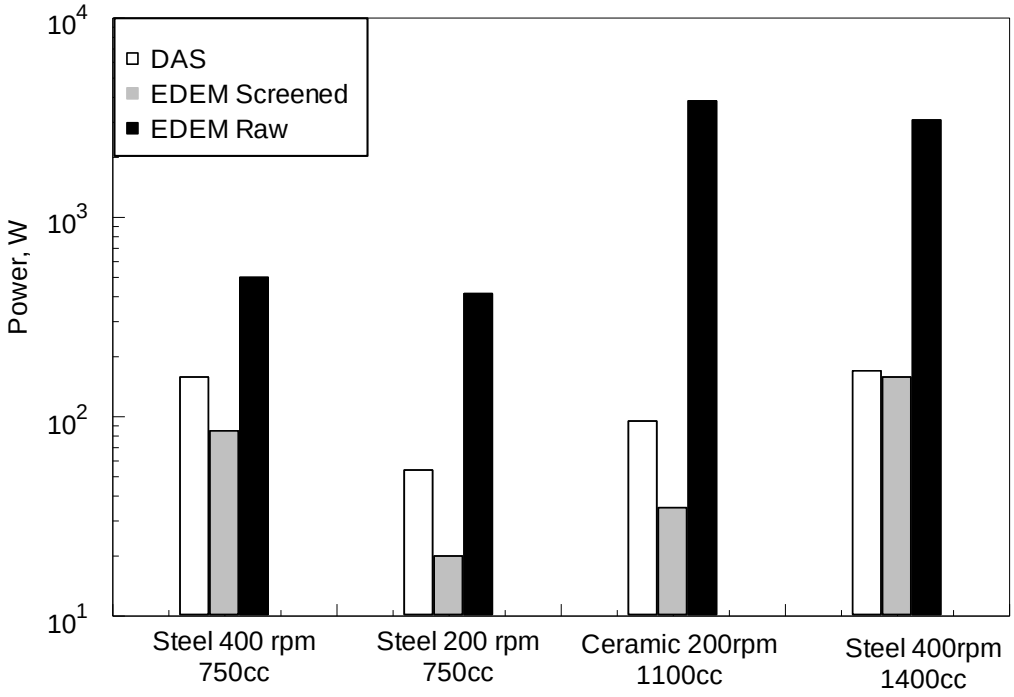

Figure I.5 Power data from EDEM and data acquisition for different cases.

REFERENCES

1. Han, B.Q., E.J. Lavernia, and F.A. Mohamed, *Mechanical properties of nanostructured materials.* Reviews on Advanced Materials Science, 2005. 9(1): p. 1-16.
2. Koch, C.C., *Top-down synthesis of nanostructured materials: Mechanical and thermal processing methods.* Reviews on Advanced Materials Science, 2003. 5(2): p. 91-99.
3. Schaffer, G.B. and P.G. McCormick, *Mechanical alloying.* Metals Forum, 1992. 16(2): p. 91-97.
4. Suryanarayana, C., *Mechanical alloying and milling.* Progress in Materials Science, 2001. 46(1-2): p. 1-184.
5. Suryanarayana, C., *Recent developments in mechanical alloying.* Reviews on Advanced Materials Science, 2008. 18(3): p. 203-211.
6. Baheti, V. and J. Militky, *Reinforcement of wet milled jute nano/micro particles in polyvinyl alcohol films.* Fibers and Polymers, 2013. 14(1): p. 133-137.
7. Ding, J., et al., *Optimised methodology for carboxymethylation of (1→3)-β-d-glucan from Yeast (Saccharomyces cerevisiae) and promotion of mechanical activation.* International Journal of Food Science and Technology, 2013. 48(2): p. 253-259.
8. Caron, V., et al., *Amorphous solid dispersions of sulfonamide/soluplus® and sulfonamide/PVP prepared by ball milling.* AAPS PharmSciTech, 2013. 14(1): p. 464-474.
9. Ho, R., et al., *Effect of milling on particle shape and surface energy heterogeneity of needle-Shaped crystals.* Pharmaceutical Research, 2012. 29(10): p. 2806-2816.
10. Le, V.N.P., E. Robins, and M.P. Flament, *Agglomerate behaviour of fluticasone propionate within dry powder inhaler formulations.* European Journal of Pharmaceutics and Biopharmaceutics, 2012. 80(3): p. 596-603.
11. Machida, N., et al., *Preparation of amorphous 75L2S·xP2S3·(25−x)P2S5 (mol%) solid electrolytes by a high-energy ball-milling process and their application for an all-solid-state lithium battery.* Solid State Ionics, 2005. 176(5–6): p. 473-479.
12. Liang, G., et al., *Catalytic effect of transition metals on hydrogen sorption in nanocrystalline ball milled MgH2–Tm (Tm=Ti, V, Mn, Fe and Ni) systems.* Journal of Alloys and Compounds, 1999. 292(1–2): p. 247-252.
13. Mohammad Sharifi, E., F. Karimzadeh, and M.H. Enayati, *Fabrication and evaluation of mechanical and tribological properties of boron carbide reinforced aluminum matrix nanocomposites.* Materials & Design, 2011. 32(6): p. 3263-3271.

14. Tahamtan, S., et al., *Fabrication of Al/A206–Al2O3 nano/micro composite by combining ball milling and stir casting technology.* Materials & Design, 2013. 49(0): p. 347-359.
15. Montinaro, S., et al., *Remediation of heavy metals contaminated soils by ball milling.* Chemosphere, 2007. 67(4): p. 631-639.
16. Mohammadi Zahrani, E. and M.H. Fathi, *The effect of high-energy ball milling parameters on the preparation and characterization of fluorapatite nanocrystalline powder.* Ceramics International, 2009. 35(6): p. 2311-2323.
17. Benjamin, J.S. and T.E. Volin, *Mechanism of mechanical alloying.* Metall Trans, 1974. 5(8): p. 1929-1934.
18. Khina, B.B. and F.H. Froes, *Modeling mechanical alloying: Advances and challenges.* Journal of Materials, 1996. 48(7): p. 36-38.
19. Li, M. and W.L. Johnson, *Instability of metastable solid solutions and the crystal to glass transition.* Physical Review Letters, 1993. 70(8): p. 1120-1123.
20. Rosato, V. and C. Massobrio, *The role of chemical disorder and volume expansion in crystal-to-amorphous transitions: simulation results for NiZr2 and Cu3Au.* Journal of Alloys and Compounds, 1993. 194(2): p. 439-445.
21. Miedema, A.R., P.F. de Châtel, and F.R. de Boer, *Cohesion in alloys - fundamentals of a semi-empirical model.* Physica B+C, 1980. 100(1): p. 1-28.
22. Maurice, D. and T.H. Courtney, *Modeling of mechanical alloying: Part I. deformation, coalescence, bdand fragmentation mechanisms.* Metallurgical and Materials Transactions A, 1994. 25(1): p. 147-158.
23. Maurice, D. and T.H. Courtney, *Modeling of mechanical alloying: Part II. Development of computational modeling programs.* Metallurgical and Materials Transactions A, 1995. 26(9): p. 2431-2435.
24. Maurice, D. and T.H. Courtney, *Modeling of mechanical alloying: Part III. Applications of computational programs.* Metallurgical and Materials Transactions A, 1995. 26(9): p. 2437-2444.
25. Courtney, T.H. and D. Maurice, *Process modeling of the mechanics of mechanical alloying.* Scripta Materialia, 1996. 34(1): p. 5-11.
26. Watanabe, R., H. Hashimoto, and G.G. Lee, *Computer simulation of milling ball motion in mechanical alloying (overview).* Materials Transactions, JIM, 1995. 36(2): p. 102-109.
27. Gaffet, E., M. Abdellaoui, and N. Malhouroux-Gaffet, *Formation of nanostructural materials induced by mechanical processings (overview).* Materials Transactions, JIM, 1995. 36(2): p. 198-209.
28. Magini, M. and A. Iasonna, *Energy transfer in mechanical alloying (overview).* Materials Transactions, JIM, 1995. 36(2): p. 123-133.

29. Koch, C.C., *Research on metastable structures using high energy ball milling at North Carolina State University (overview).* Materials Transactions, JIM, 1995. 36(2): p. 85-95.
30. Mulas, G., et al., *Process parameters and amorphization rate of Cu-Ti system under mechanical deformation*. Material Science Forum, 1998. p. 693-698.
31. Cocco, G., F. Delogu, and L. Schiffini, *Toward a quantitative understanding of the mechanical alloying process.* Journal of Materials Synthesis and Processing, 2000. 8(3-4): p. 167-180.
32. Delogu, F., L. Schiffini, and G. Cocco, *A quantitative description of the amorphisation behaviour by mechanical alloying*. Material Science Forum, 2001. p. 337-342.
33. Weeber, A.W. and H. Bakker, *Amorphization by ball milling. A review.* Physica B: Physics of Condensed Matter, 1988. 153(1-3): p. 93-135.
34. Huang, H., J. Pan, and P.G. McCormick, *On the dynamics of mechanical milling in a vibratory mill.* Materials Science and Engineering A, 1997. 232(1-2): p. 55-62.
35. Jiang, X., et al., *Mechanical alloying and reactive milling in a high energy planetary mill.* Journal of Alloys and Compounds, 2009. 478(1-2): p. 246-251.
36. Ward, T.S., et al., *A study of mechanical alloying processes using reactive milling and discrete element modeling.* Acta Materialia, 2005. 53(10): p. 2909-2918.
37. Hashimoto, H., Y.-H. Park, and R. Watanabe, *Model simulation of vibratory ball milling of metal powders.* Funtai Oyobi Fummatsu Yakin/Journal of the Japan Society of Powder and Powder Metallurgy, 1991. 38(1): p. 37-41.
38. Feng, Y.T., K. Han, and D.R.J. Owen, *Discrete element simulation of the dynamics of high energy planetary ball milling processes.* Materials Science and Engineering A, 2004. 375-377(1-2 SPEC. ISS.): p. 815-819.
39. Mishra, B.K., *A review of computer simulation of tumbling mills by the discrete element method: Part I-contact mechanics.* International Journal of Mineral Processing, 2003. 71(1-4): p. 73-93.
40. Mishra, B.K., *A review of computer simulation of tumbling mills by the discrete element method Part II-Practical applications.* International Journal of Mineral Processing, 2003. 71(1-4): p. 95-112.
41. Yang, R.Y., et al., *DEM simulation of the flow of grinding media in IsaMill.* Minerals Engineering, 2006. 19(10): p. 984-994.
42. Cleary, P.W., M.D. Sinnott, and R.D. Morrison, *DEM prediction of particle flows in grinding processes.* International Journal for Numerical Methods in Fluids, 2008. 58(3): p. 319-353.
43. Murty, B.S. and S. Ranganathan, *Novel materials synthesis by mechanical alloying/milling.* International Materials Reviews, 1998. 43(3): p. 101-141.

44. Charkhi, A., H. Kazemian, and M. Kazemeini, *Optimized experimental design for natural clinoptilolite zeolite ball milling to produce nano powders.* Powder Technology, 2010. 203(2): p. 389-396.
45. Dutkiewicz, J., et al., *Cu/Ti base multicomponent amorphous Cu 47Ti 33Zr 11Ni 8Si 1 and nanocrystalline silver composites.* Physica Status Solidi (A) Applications and Materials Science, 2010. 207(5): p. 1109-1113.
46. Wei, X., et al., *Fabrication of Al-based bulk metallic glass by mechanical alloying and vacuum hot consolidation.* Journal of Alloys and Compounds, 2010. 501(1): p. 164-167.
47. de Barros, R.A. and W.M. de Azevedo, *Polyaniline/silver nanocomposite preparation under extreme or non-classical conditions.* Synthetic Metals, 2008. 158(21-24): p. 922-926.
48. E.L. Dreizin and M. Scoenitz, *Nano-composite energetic powders prepared by arrested reactive milling.* Proceedingf of the Combustion Institute, 2009. 30(II): p. 2071-2078.
49. Umbrajkar, S.M., et al., *Aluminum-rich Al-MoO3 nanocomposite powders prepared by arrested reactive milling.* Journal of Propulsion and Power, 2008. 24(2): p. 192-198.
50. Jayasundara, C.T., et al., *Discrete particle simulation of particle flow in IsaMill-Effect of grinding medium properties.* Chemical Engineering Journal, 2008. 135(1-2): p. 103-112.
51. Huang, H., et al., *An investigation of the effect of powder on the impact characteristics between a ball and a plate using free falling experiments.* Materials Science and Engineering A, 1998. 241(1-2): p. 38-47.
52. Yamada, K. and C.C. Koch, *Influence of mill energy and temperature on the structure of the TiNi intermetallic after mechanical attrition.* Journal of Materials Research, 1993. 8(6): p. 1317-1326.
53. Korchagin, M.A., et al., *Thermal explosion of a mechanically activated 3Ni-Al mixture.* Combustion, Explosion and Shock Waves, 2010. 46(1): p. 41-46.
54. Maleki, A., et al., *Mechanism of zinc oxide-aluminum aluminothermic reaction.* Journal of Materials Science, 2010. 45(20): p. 5574-5580.
55. Denny, P.J., *Compaction equations: A comparison of the Heckel and Kawakita equations.* Powder Technology, 2002. 127(2): p. 162-172.
56. Forrest, M., *Virtual milling.* Materials World, 2007. 15(4): p. 30-32.
57. R.D., M., *Compliance of elastic bodies in contact, Journal of Applied Mechanics.* Journal of Applied Mechanics, 1949. 16: p. 259-268.
58. Cundall, P.A. and O.D.L. Strack, *Discrete numerical model for granular assemblies.* Geotechnique, 1979. 29(1): p. 47-65.

59. Rydin, R.W., D. Maurice, and T.H. Courtney, *Milling dynamics: Part I. Attritor dynamics: Results of a cinematographic study.* Metallurgical Transactions A, 1993. 24(1): p. 175-185.
60. Santhanam, P.R. and E.L. Dreizin, *Predicting conditions for scaled-up manufacturing of materials prepared by ball milling.* Powder Technology, 2012. 221: p. 403-411.
61. Goodson, R., F. Larson, and L. Sheehan, *Energy input monitoring during attritor milling.* International Journal of Refractory Metals and Hard Materials, 1985. 4(2): p. 70-76.
62. Kimura, H., M. Kimura, and F. Takada, *Development of an extremely high energy ball mill for solid state amorphizing transformations.* Journal of The Less-Common Metals, 1988. 140(C): p. 113-118.
63. Iasonna, A. and M. Magini, *Power measurements during mechanical milling. An experimental way to investigate the energy transfer phenomena.* Acta Materialia, 1996. 44(3): p. 1109-1117.
64. Magini, M., et al., *Power measurements during mechanical milling - II. The case of "single path cumulative" solid state reaction.* Acta Materialia, 1998. 46(8): p. 2841-2850.
65. Mulas, G., L. Schiffini, and G. Cocco, *Impact energy and reactive milling: A self propagating reaction*. Material Science Forum, 1997. 235(II): p. 15-22.
66. Shoshin, Y.L., R.S. Mudryy, and E.L. Dreizin, *Preparation and characterization of energetic Al-Mg mechanical alloy powders.* Combustion and Flame, 2002. 128(3): p. 259-269.
67. M. Schoenitz, T. Ward and E.L.Dreizin, *Preparation of Energetic Metastable Nano-Composite Materials by Arrested Reactive Milling*. Material Research Society Symposium, 2004. 800: p. 85-90.
68. Khakbiz, M. and F. Akhlaghi, *Synthesis and structural characterization of Al-B4C nano-composite powders by mechanical alloying.* Journal of Alloys and Compounds, 2009. 479(1-2): p. 334-341.
69. Mohammad Sharifi, E., F. Karimzadeh, and M.H. Enayati, *Fabrication and evaluation of mechanical and tribological properties of boron carbide reinforced aluminum matrix nanocomposites.* Materials and Design, 2011. 32(6): p. 3263-3271.
70. Zhang, D.L., *Processing of advanced materials using high-energy mechanical milling.* Progress in Materials Science, 2004. 49(3-4): p. 537-560.
71. Ren, H., Q. Jiao, and S. Chen, *Mixing Si and carbon nanotubes by a method of ball-milling and its application to pyrotechnic delay composition.* Journal of Physics and Chemistry of Solids, 2010. 71(2): p. 145-148.

72. van der Heijden, A.E.D.M. and A.B. Leeuwenburgh, *HNF/HTPB propellants: Influence of HNF particle size on ballistic properties.* Combustion and Flame, 2009. 156(7): p. 1359-1364.
73. Aguey-Zinsou, K.F., et al., *Effect of Nb2O5 on MgH2 properties during mechanical milling.* International Journal of Hydrogen Energy, 2007. 32(13): p. 2400-2407.
74. Hanada, N., T. Ichikawa, and H. Fujii, *Catalytic effect of nanoparticle 3d-transition metals on hydrogen storage properties in magnesium hydride MgH2 prepared by mechanical milling.* Journal of Physical Chemistry B, 2005. 109(15): p. 7188-7194.
75. Liang, G., et al., *Catalytic effect of transition metals on hydrogen sorption in nanocrystalline ball milled MgH2-Tm (Ti, V, Mn, Fe and Ni) systems.* Journal of Alloys and Compounds, 1999. 292(1-2): p. 247-252.
76. Lefort, R., et al., *Solid state NMR and DSC methods for quantifying the amorphous content in solid dosage forms: An application to ball-milling of trehalose.* International Journal of Pharmaceutics, 2004. 280(1-2): p. 209-219.
77. MacHida, N., et al., *Preparation of amorphous 75L 2S•xP 2S 3•(25-x)P 2S 5 (mol%) solid electrolytes by a high-energy ball-milling process and their application for an all-solid-state lithium battery.* Solid State Ionics, 2005. 176(5-6): p. 473-479.
78. Janot, R. and D. Guérard, *Ball-milling in liquid media: Applications to the preparation of anodic materials for lithium-ion batteries.* Progress in Materials Science, 2005. 50(1): p. 1-92.
79. Liu, T.Y., et al., *The effect of ball milling treatment on structure and porosity of maize starch granule.* Innovative Food Science and Emerging Technologies, 2011. 12(4): p. 586-593.
80. Montinaro, S., et al., *Remediation of heavy metals contaminated soils by ball milling.* Chemical Engineering Transactions, 2012. 28: p. 187-192.
81. Cleary, P.W., *Predicting charge motion, power draw, segregation and wear in ball mills using discrete element methods.* Minerals Engineering, 1998. 11(11): p. 1061-1080.
82. Kwan, C.C., et al., *Analysis of the milling rate of pharmaceutical powders using the Distinct Element Method (DEM).* Chemical Engineering Science, 2005. 60(5): p. 1441-1448.
83. Mori, H., et al., *Ball mill simulation in wet grinding using a tumbling mill and its correlation to grinding rate.* Powder Technology, 2004. 143-144: p. 230-239.
84. Zhu, H.P., et al., *Discrete particle simulation of particulate systems: A review of major applications and findings.* Chemical Engineering Science, 2008. 63(23): p. 5728-5770.

85. Bell, N., Y. Yu, and P.J. Mucha. *Particle-based simulation of granular materials*. Computer Animation: Cnference Proceedings, 2005. p. 77-86.
86. Coetzee, C.J., D.N.J. Els, and G.F. Dymond, *Discrete element parameter calibration and the modelling of dragline bucket filling.* Journal of Terramechanics, 2010. 47(1): p. 33-44.
87. Chung, Y.C., H.H. Liao, and S.S. Hsiau, *Convection behavior of non-spherical particles in a vibrating bed: Discrete element modeling and experimental validation.* Powder Technology, 2013. 237: p. 53-66.
88. Grima, A.P. and P.W. Wypych, *Investigation into calibration of discrete element model parameters for scale-up and validation of particle-structure interactions under impact conditions.* Powder Technology, 2011. 212(1): p. 198-209.
89. Tao, H., et al., *Discrete element method modeling of non-spherical granular flow in rectangular hopper*. Chemical Engineering and Processing: Process Intensification, 2010. 49(2): p. 151-158.
90. Zhao, D., et al., *Three-dimensional discrete element simulation for granular materials.* Engineering Computations (Swansea, Wales), 2006. 23(7): p. 749-770.
91. Goda, T.J. and F. Ebert, *Three-dimensional discrete element simulations in hoppers and silos.* Powder Technology, 2005. 158(1-3): p. 58-68.
92. Ketterhagen, W.R., et al. *Segregation during hopper discharge: A DEM and experimental study*. AIChE Annual Meeting, 2005. p. 3078.
93. Muguruma, Y., et al., *Discrete particle simulation of a rotary vessel mixer with baffles.* Powder Technology, 1997. 93(3): p. 261-266.
94. Sudah, O.S., et al., *Simulation and experiments of mixing and segregation in a tote blender.* AIChE Journal, 2005. 51(3): p. 836-844.
95. Inoue, T. and K. Okaya, *Grinding mechanism of centrifugal mills - A simulation study based on the discrete element method.* International Journal of Mineral Processing, 1996. 44-45(SPEC. ISS.): p. 425-435.
96. Mishra, B.K., R.K. Rajamani, and W.G. Pariseau. *Simulation of ball charge motion in ball mills*. Society of Mining Engineers of AIME, 1990.5: p. 137.
97. Goldschmidt, M.J.V., et al., *Discrete element modelling of fluidised bed spray granulation.* Powder Technology, 2003. 138(1): p. 39-45.
98. Kaneko, Y., T. Shiojima, and M. Horio, *DEM simulation of fluidized beds for gas-phase olefin polymerization.* Chemical Engineering Science, 1999. 54(24): p. 5809-5821.
99. Newell, K.J. and R.M. McMeeking. *Discrete element analysis for process modeling of titanium powder consolidation*. American Society of Mechanical Enginees, 1995. 216: p. 109-121.
100. Tamura, S., T. Aizawa, and J. Kihara. *Granular modeling simulator for powder compaction processes*. Advances in Powder Metallurgy, 1992. 2: p. 29-41.

101. Chou, C.S. and Y.W. Chen, *Study of Flow Patterns in an Inclined Moving Granular Bed.* Bulk Solids Handling, 2004. 24(1): p. 32-36+69.
102. Moysey, P.A. and M.R. Thompson, *Modelling the solids inflow and solids conveying of single-screw extruders using the discrete element method.* Powder Technology, 2005. 153(2): p. 95-107.
103. Labous, L., A.D. Rosato, and R.N. Dave, *Measurements of collisional properties of spheres using high-speed video analysis.* Physical Review E - Statistical Physics, Plasmas, Fluids, and Related Interdisciplinary Topics, 1997. 56(5 SUPPL. B): p. 5717-5725.
104. Lorenz, A., C. Tuozzolo, and M.Y. Louge, *Measurements of impact properties of small, nearly spherical particles.* Experimental Mechanics, 1997. 37(3): p. 292-298.
105. van Buijtenen, M.S., et al., *Discrete particle simulation study on the influence of the restitution coefficient on spout fluidized-bed dynamics.* Chemical Engineering and Technology, 2009. 32(3): p. 454-462.
106. Mishra, B.K. and C. Thornton, *An improved contact model for ball mill simulation by the discrete element method.* Advanced Powder Technology, 2002. 13(1): p. 25-41.
107. Bordbar, M.H. and T. Hyppänen, *Simulation of bubble formation and heaping in a vibrating granular bed.* Chemical Engineering Communications, 2011. 198(7): p. 905-919.
108. Aryaei, A., K. Hashemnia, and K. Jafarpur, *Experimental and numerical study of ball size effect on restitution coefficient in low velocity impacts.* International Journal of Impact Engineering, 2010. 37(10): p. 1037-1044.
109. Durda, D.D., et al., *Experimental determination of the coefficient of restitution for meter-scale granite spheres.* Icarus, 2011. 211(1): p. 849-855.
110. Qin, Z. and R.H. Pletcher, *Particle impact theory including surface asperity deformation and recovery.* Journal of Aerosol Science, 2011. 42(12): p. 852-858.
111. Antypov, D., J.A. Elliott, and B.C. Hancock, *Effect of particle size on energy dissipation in viscoelastic granular collisions.* Physical Review E - Statistical, Nonlinear, and Soft Matter Physics, 2011. 84(2).
112. Härtl, J. and J.Y. Ooi, *Experiments and simulations of direct shear tests: Porosity, contact friction and bulk friction.* Granular Matter, 2008. 10(4): p. 263-271.
113. Emami, S. and L.G. Tabil, *Friction and compression characteristics of chickpea flour and components (DOI:10.1016/j.powtec.2006.12.021).* Powder Technology, 2008. 182(1): p. 119-126.
114. Aissa, A.A., C. Duchesne, and D. Rodrigue, *Effect of friction coefficient and density on mixing particles in the rolling regime.* Powder Technology, 2011. 212(2): p. 340-347.

115. Azhdar, B., B. Stenberg, and L. Kari, *Determination of dynamic and sliding friction, and observation of stick-slip phenomenon on compacted polymer powders during high-velocity compaction.* Polymer Testing, 2006. 25(8): p. 1069-1080.
116. Larsson, S.H., *Kinematic wall friction properties of reed canary grass powder at high and low normal stresses.* Powder Technology, 2010. 198(1): p. 108-113.
117. Orlando, A.D., D.M. Hanes, and H.H. Shen. *Scaling effects in direct shear tests.* AIP Conference Proceedings, 2009. 1145: p. 405-408.
118. Zhu, H.P., A.B. Yu, and Y.H. Wu, *Numerical investigation of steady and unsteady state hopper flows.* Powder Technology, 2006. 170(3): p. 125-134.
119. Wu, S.M., et al., *Numerical investigation of crater phenomena in a particle stream impact onto a granular bed.* Granular Matter, 2007. 9(1-2): p. 7-17.
120. Nouchi, T., A.B. Yu, and K. Takeda, *Experimental and numerical investigation of the effect of buoyancy force on solid flow.* Powder Technology, 2003. 134(1-2): p. 98-107.
121. Bharadwaj, R., W.R. Ketterhagen, and B.C. Hancock, *Discrete element simulation study of a Freeman powder rheometer.* Chemical Engineering Science, 2010. 65(21): p. 5747-5756.
122. Ketterhagen, W.R., et al., *Predicting the flow mode from hoppers using the discrete element method.* Powder Technology, 2009. 195(1): p. 1-10.
123. Qiu, H. and W. Jia, *High-resolution optical particle sizing in an optimized orientation.* Optical Engineering, 1999. 38(12): p. 2104-2113.
124. Shackelford, J.F., W. Alexander, and J.S. Park, *CRC practical handbook of materials selection.* CRC Press, Boca Raton : FL, 1995.
125. Beloni, E., P.R. Santhanam, and E.L. Dreizin, *Electrical conductivity of a metal powder struck by a spark.* Journal of Electrostatics, 2012. 70(1): p. 157-165.
126. Zhang, D. and W.J. Whiten, *The calculation of contact forces between particles using spring and damping models.* Powder Technology, 1996. 88(1): p. 59-64.
127. Tsuji, Y., T. Tanaka, and T. Ishida, *Lagrangian numerical simulation of plug flow of cohesionless particles in a horizontal pipe.* Powder Technology, 1992. 71(3): p. 239-250.
128. Alizadeh, E., F. Bertrand, and J. Chaouki, *Development of a granular normal contact force model based on a non-Newtonian liquid filled dashpot.* Powder Technology, 2013. 237: p. 202-212.
129. Aly, Y., M. Schoenitz, and E.L. Dreizin, *Ignition and combustion of mechanically alloyed Al-Mg powders with customized particle sizes.* Combustion and Flame, 2013. 160(4): p. 835-842.